# A Laser System for Cavity-Enhanced State-Dependent Optical Lattices for Ultracold Strontium

**Ömer Faruk Erşahan**

München 2023

# Ein Lasersystem für Resonator-verstärkte zustandsabhängige optische Gitter für ultrakaltes Strontium

School of Natural Sciences
Technische Universität München

Fakultät für Physik
Ludwig-Maximilians-Universität München

Max-Planck-Institut für Quantenoptik

Masterarbeit

vorgelegt von

**Ömer Faruk Erşahan**

aus Ankara, Türkei

München, den 04. Oktober 2023

Tag der mündlichen Prüfung: 13. Nov 2023
Erstgutachter: Prof. Dr. Immanuel Bloch
Zweitgutachter: Prof. Dr. Monika Aidelsburger

## Abstract

In this thesis, we report on the construction and stabilization of a laser system for generating state-dependent optical lattices in an enhancement cavity for ultracold strontium atoms. For this purpose, two injection lock amplifiers are built and they are frequency-stabilized to the enhancement cavity. In addition, an intensity control loop is used to stabilize the intensity of the lasers. The amplified spontaneous emission produced by the lasers is also suppressed to prevent uncontrolled heating mechanisms that may take place in the lattice. Based on our experimental findings, we estimate the heating and the scattering rates of strontium atoms in the state-dependent lattice. The developed techniques open up new possibilities in simulating open quantum systems with ultracold strontium.

# Contents

# List of Tables

# List of Figures

# Chapter 1

# Introduction

Simulating the behavior of many-body systems that are composed of a large number of interacting particles is a task that researchers have been tackling since the advent of computer technology. Simulating such a system becomes particularly challenging if the laws of quantum mechanics govern its dynamics. This difficulty arises from the fact that the dimension of the Hilbert space scales exponentially with the number of particles in a given quantum system, which overloads a classical computer rapidly. To overcome this problem, Richard Feynman proposed the solution of using a quantum system that is experimentally well controlled to simulate another quantum system [1, 2]. To achieve this, a mapping between the Hamiltonians of the two systems has to be established. Then, the parameters of the simulation can be controlled through the accessible parameters of the experiment.

To this end, one of the promising approaches includes the use of ultracold neutral atoms [3–5]. In the field of ultracold neutral atoms, optical forces from laser light are used to cool and trap atoms. While cooling atoms requires a dissipative scattering force, trapping can be achieved with dipole forces. A specific configuration that traps atoms using dipole forces is known as an optical lattice. Optical lattices are essentially periodic potential well structures created by interfering laser beams [6]. Atoms that are cooled by laser cooling techniques can be trapped in these potential wells, also known as lattice sites. When an atom is trapped in a lattice site, it can interact with other atoms occupying the same site and it can "hop" into other sites due to quantum tunneling. Such a system can already simulate important models in condensed matter physics such as the Hubbard model [7]. The intensity of the lattice field determines the on-site interaction and the tunneling parameters, which provides a system with a high degree of tunability. Using this tunability, a cornerstone experiment demonstrated quantum phase transitions of bosonic particles in an optical lattice [8]. The successive demonstrations of similar quantum many-body phenomena motivated researchers to come up with various quantum computation [9–11] and quantum simulation schemes that use ultracold atoms in optical lattices. A particular class of the proposed quantum simulation schemes involve the use of state-dependent lattices. These lattices trap neutral atoms selectively, based on their internal quantum states. Such systems can be used to study the dynamics of open quantum systems, such as the spontaneous emission of quantum emitters [12–16].

One of the main requirements of performing quantum simulations with ultracold atoms

in optical lattices is the detection of atoms with single-site resolution. This detection can be achieved by imaging the fluorescence of atoms in the lattice using a microscope objective with a high numerical aperture [17–25]. This technique is known as quantum gas microscopy. Quantum gas microscopy can reveal valuable information about the many-body system since it allows us to image individual atoms.

The choice of atomic species also plays an important role in the proposed quantum simulation experiments. Although alkali atoms were initially used in such experiments, alkaline-earth atoms are gaining more attention due to several advantages [26]. One of the promising features of alkaline-earth atoms is their rich electronic structure, arising from the two valence electrons forming spin-singlet and triplet states. In particular, the strontium atom has an exceptionally narrow ($\sim 1$ mHz) transition in its electronic structure. This is the $5s^2\ {}^1\mathrm{S}_0 - 5s5p\ {}^3\mathrm{P}_0$ transition (see Fig. 1.1). Due to this narrow transition, the electronic excited state ${}^3\mathrm{P}_0$ acquires a long lifetime [27]. For this reason, the ${}^1\mathrm{S}_0 - {}^3\mathrm{P}_0$ transition of strontium is extensively studied as a frequency standard in optical lattice clocks [28–35]. This situation serves as an advantage, since it makes longer simulation times viable for simulations that involve the ${}^3\mathrm{P}_0$ state. Furthermore, efficient laser cooling can be achieved via the ${}^1\mathrm{S}_0 - 5s5p\ {}^1\mathrm{P}_1$ and the ${}^1\mathrm{S}_0 - 5s5p\ {}^3\mathrm{P}_1$ transitions, which have linewidths of $\gamma = 30.41(9)$ MHz and $\gamma = 7.423(7)$ kHz, respectively. The broad linewidth of the ${}^1\mathrm{S}_0 - {}^1\mathrm{P}_1$ transition can be used for fast initial cooling while the narrow linewidth of the ${}^1\mathrm{S}_0 - {}^3\mathrm{P}_1$ transition allows reaching low temperatures [36, 37].

Our research team is currently developing an experimental apparatus to perform quantum gas microscopy with ${}^{88}$Sr atoms in state-dependent lattices for the ultimate goal of simulating quantum emitters in structured reservoirs. So far, the advances made by our research team include: (1) the development of a magneto-optical trap for strontium atoms to reach ultracold temperatures [42], (2) the experimental measurement of the so called "tune-out" wavelength, which is crucial for the simulation of open quantum systems [43], (3) the development of a novel crossed-cavity design for enhancing the size of the lattice and for reducing the spatial inhomogeneities in the system [44], and (4) the development of an experimental scheme for addressing atoms locally using the ${}^1\mathrm{S}_0 - 5s5p\ {}^3\mathrm{P}_2$ transition of strontium [45]. As a next step, the team aims to integrate two-dimensional state-dependent lattices in the experiment and to demonstrate quantum simulations. For this reason, a laser system that can generate a state-dependent lattice needs to be constructed. While constructing such a system, there are several considerations to take into account. The first consideration is the tunneling of strontium atoms in the lattice. In particular, the ${}^3\mathrm{P}_2$ atoms are not supposed to tunnel to an adjacent site during the simulation to prevent inelastic collisions of excited state atoms. Therefore, we need to determine the optical power regime that we will work with and we need to build appropriate lasers to reach these powers. Then, we need to consider the intensity and frequency instabilities of the lasers that we use to generate the lattice. These instabilities may result in a heating mechanism known as parametric heating [46]. Heating is an unwanted effect since it leads to the loss of atoms from the lattice. Another mechanism

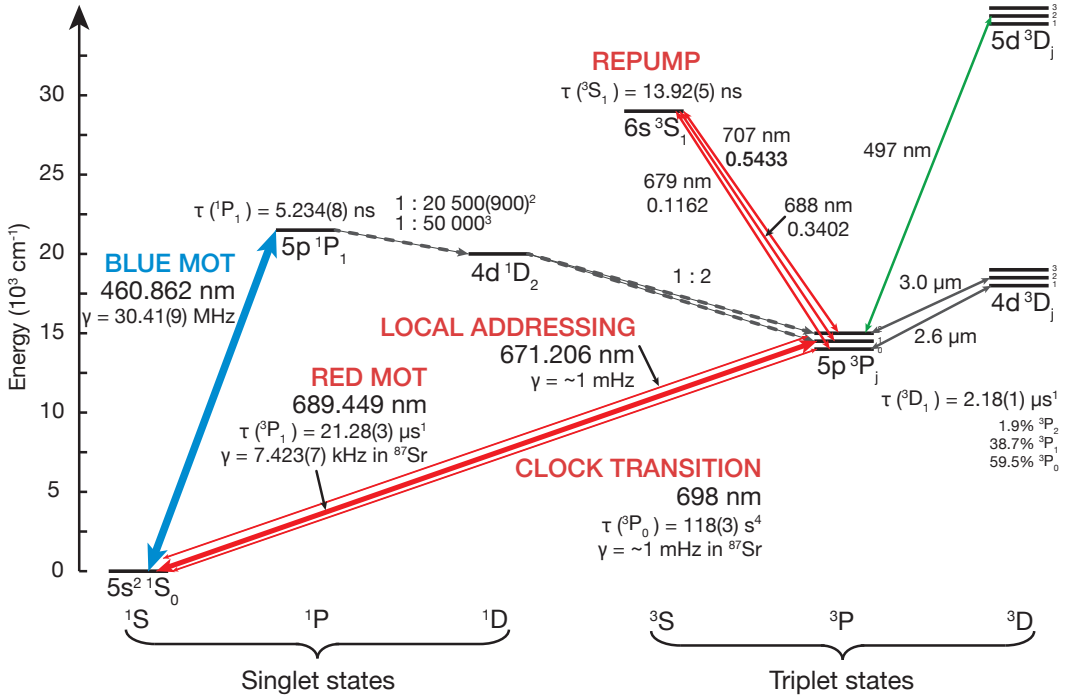


**Figure 1.1** The energy level diagram of $^{88}$Sr. The diagram contains information about the most relevant states and transitions. The figure is adapted from Ref. [38] and the data is obtained from Refs. $^1$[39] $^2$[40] $^3$[41] $^4$[27].

that may induce heating is the scattering of lattice photons by the atoms. This situation is particularly enhanced for optical lattices operated in the vicinity of an electronic transition and lasers that contain an incoherent background radiation as a result of amplified spontaneous emission. This thesis reports on the construction of this laser system and estimates the instabilities of the generated state-dependent lattice.

The outline of this thesis is as follows:

- In Chapter 2, we provide a theoretical background of state-dependent optical lattices, we discuss our motivations to use the $^1\mathrm{S}_0 - {}^3\mathrm{P}_2$ transition of strontium in detail, we present the crossed-cavity design of our team and we calculate the lattice depth that we can reach in this cavity.
- In Chapter 3, we introduce the lasers and the injection locking modules that we use for generating the state-dependent lattices.
- In Chapter 4, we describe the experimental setup that combines the Pound-Drever-Hall technique with a control loop for intensity stabilization and we measure the relative intensity noise of the lasers to estimate the parametric heating rate.

- In Chapter 5, we estimate the amount of amplified spontaneous emission produced by our lasers, we describe the method we use to suppress it and we calculate the resulting photon scattering rate.

# Chapter 2

# State-Dependent Optical Lattices for Strontium

In this Chapter, we provide the reader with a general overview of state-dependent optical lattices and discuss our motivations to make such optical lattices for strontium in a crossed-cavity configuration. For this reason, we begin by briefly discussing the basics of optical lattices. Then, we present the concept of state-dependent lattices and the matter-wave emission experiments that we plan to conduct with them. We proceed by explaining the relevance of the $^1\mathrm{S}_0$ and the $^3\mathrm{P}_2$ states of strontium for these experiments. Lastly, we introduce the in-vacuum buildup cavity system that our research team uses to enhance the size of our optical lattices. In this last part, we also determine the minimum lattice depth requirements of the state-dependent lattice that we want to generate inside the buildup cavity.

## 2.1 Optical lattices

In the most general sense, optical lattices are periodic arrangements of potential wells made of optical standing waves that trap neutral atoms. In this Section, we discuss how these lattices are generated and how they trap neutral atoms.

### 2.1.1 Polarizability

First, we introduce the concept of polarizability, which is a crucial concept in understanding off-resonant atom-light interactions. We follow the definitions and derivations of Ref. [47], while skipping some of the intermediate steps. We encourage the reader to refer to this excellent source for a more detailed mathematical description of polarizability.

We consider the oscillating electric field of a laser interacting with a two-level atom. This interaction occurs in an off-resonant manner so that the electric field does not cause an atomic transition. We express the electric field as

$$\mathbf{E}(\mathbf{r},t) = \frac{\mathbf{E}(\mathbf{r})\exp(-i\omega t)}{2} + \text{c.c.}, \tag{2.1}$$

where $\omega$ is the optical angular frequency, $t$ is time, and $\mathbf{r}$ is the position vector. Classically, we consider the atom as a dipole consisting of a positive and a negative charge. The dipole moment induced by the field is given by

$$\mathbf{d} = \alpha(\omega)\mathbf{E}(\mathbf{r}, t), \tag{2.2}$$

where $\alpha(\omega)$ is defined as the polarizability. With this expression, we can write the time-averaged potential energy of the induced dipole as

$$V_{\text{dipole}} = -\langle \frac{\mathbf{d} \cdot \mathbf{E}(\mathbf{r}, t)}{2} \rangle. \tag{2.3}$$

Here, we have a factor of $1/2$ due to the fact that the dipole is induced and not permanent. Using the expression for the intensity of light as

$$I(\mathbf{r}) = \frac{\sqrt{\epsilon_0/\mu_0}}{2}|\mathbf{E}(\mathbf{r})|^2, \tag{2.4}$$

with vacuum permittivity $\epsilon_0$ and vacuum permeability $\mu_0$, we rewrite Eqn. (2.3) as

$$V_{\text{dipole}} = -\frac{1}{2}\sqrt{\frac{\mu_0}{\epsilon_0}}\text{Re}[\alpha(\omega)]I(\mathbf{r}). \tag{2.5}$$

Therefore, the dipole sees a potential proportional to $I(\mathbf{r})$. The force exerted on the induced dipole can be expressed as

$$F_{\text{dipole}} = -\nabla V_{\text{dipole}} \propto \nabla I(\mathbf{r}). \tag{2.6}$$

Thus, intensity gradients result in a net dipole force while the positions where $\nabla I(\mathbf{r})$ is zero correspond to attractive and repulsive dipole potentials. An attractive dipole potential is the basis of trapping neutral atoms using optical lattices. If $\text{Re}[\alpha(\omega)]$ is positive, the atoms are attracted to intensity maxima. For a negative polarizability, the atoms are attracted to intensity minima. To explain the conditions which may give rise to a positive or a negative polarizability, we introduce the classical Lorentz-oscillator model, which describes the polarizability of a two-level atom as [48]

$$\alpha(\omega) = 6\pi\epsilon_0 c^3 \frac{\Gamma}{\omega_0^2(\omega_0^2 - \omega^2 - i\Gamma\frac{\omega^3}{\omega_0^2})} \tag{2.7}$$

where $c$ is the speed of light in vacuum, $\Gamma$ is the natural decay rate of the excited state and $\omega_0$ is the transition frequency. From this expression, we observe that the real part of the polarizability is negative for $\omega > \omega_0$ (blue-detuned) and it is positive for $\omega < \omega_0$ (red-detuned). Therefore, the sign of the detuning determines the position of the attractive potential in a dipole trap.

### 2.1.2 Standing electromagnetic wave

Optical lattices are formed by interfering laser beams that create a standing electromagnetic wave. A standing electromagnetic wave is a specific type of wave pattern that is formed by the superposition of two electromagnetic waves that have the same frequency, amplitude and polarization, but travel in opposite directions. These electromagnetic

waves interfere with each other and they create regions of constructive and destructive interference. Here, we derive the potential arising from such a standing wave following the derivations in Ref. [43]. The electric field of a standing electromagnetic wave in 1D can be expressed as

$$E(x,t) = E_0 \exp(ikx - i\omega t) + E_0 \exp(-ikx - i\omega t), \tag{2.8}$$

where $E_0$ is the amplitude of each counter-propagating beam, $k = 2\pi/\lambda$ is the wave number, $\lambda$ is the wavelength, and $x$ is the coordinate. To obtain the intensity $I(x)$ of the standing wave, we take the modulus-squared of Eqn. (2.8) and multiply it by $\frac{1}{2}cn\epsilon_0$ to obtain

$$I(x) = \frac{1}{2}cn\epsilon_0 |E_0 \exp(ikx - i\omega t) + E_0 \exp(-ikx - i\omega t)|^2 = 4I_0 \cos^2(kx), \tag{2.9}$$

where $n$ is the refractive index of the medium in which the standing wave forms ($n = 1$ for vacuum) and $I_0 = \frac{1}{2}cn\epsilon_0|E_0|^2$. The resulting intensity pattern $I(x)$ does not depend on time, which means that it is a stationary pattern. Furthermore, this pattern has a $\cos^2$ shape with a periodicity of $\lambda/2$. Using Eqn. (2.5), we express the potential seen by the atom as

$$V(x) = -2\sqrt{\frac{\mu_0}{\epsilon_0}} I_0 \mathrm{Re}[\alpha(\omega)] \cos^2(kx). \tag{2.10}$$

We expand $\cos^2(kx)$ around $x = 0$ and find

$$\cos^2(kx) = (1 - \frac{1}{2!}(kx)^2 + \frac{1}{4!}(kx)^4 - \cdots)(1 - \frac{1}{2!}(kx)^2 + \frac{1}{4!}(kx)^4 - \cdots) = 1 - (kx)^2 + \mathcal{O}[(kx)^4]. \tag{2.11}$$

Hence, to a second order approximation, we can write the dipole potential as

$$V(x) \approx 2\sqrt{\frac{\mu_0}{\epsilon_0}} I_0 \mathrm{Re}[\alpha(\omega)](k^2x^2 - 1) = V_x(k^2x^2 - 1), \tag{2.12}$$

where we introduced the lattice depth (or trap depth) as $V_x = 2\sqrt{\frac{\mu_0}{\epsilon_0}} I_0 \mathrm{Re}[\alpha(\omega)]$. This expression has the form of a harmonic potential $\frac{m\omega_{\mathrm{tr}}^2}{2}x^2$, where $m$ is the mass of the atom and $\omega_{\mathrm{tr}}$ is defined as the angular trap frequency given by

$$\omega_{\mathrm{tr}} = 2\pi\nu_{\mathrm{tr}} = \sqrt{\frac{2k^2}{m}V_x} = \omega_{\mathrm{rec}}\sqrt{\frac{4V_x}{E_{\mathrm{rec}}}}. \tag{2.13}$$

Here, we introduced the recoil energy $E_{\mathrm{rec}} = \hbar\omega_{\mathrm{rec}} = \frac{\hbar^2k^2}{2m}$, which is the kinetic energy gained by the atom after absorbing or emitting a photon with momentum $\hbar k$.

Due to the harmonic form of the potential that the atom sees, we can approximate the

energy levels of the system with the quantum harmonic oscillator model. This approach results in quantum states that are separated by $\hbar\omega_{\mathrm{tr}}$ in energy. Furthermore, we can extend our discussion into three dimensions by expressing the 3D lattice potential as

$$V_{\mathrm{3D}}(\mathbf{r}) = V_x k^2 x^2 + V_y k^2 y^2 + V_z k^2 z^2. \tag{2.14}$$

Hence, we have a three-dimensional optical lattice that traps atoms in harmonic quantum wells with a spatial periodicity of $\lambda/2$.

### 2.1.3 Scalar, vector and tensor polarizabilities

So far, we treated the atom and the oscillating field classically to explain the concept of polarizability in a simplistic manner. A quantum mechanical treatment of a multi-level atom such as strontium yields three irreducible parts of the polarizability [49–51]. For this purpose, we consider an atom interacting with an electromagnetic field whose polarization vector is given by $\hat{\epsilon} = \epsilon_x\hat{\mathbf{x}} + \epsilon_y\hat{\mathbf{y}} + \epsilon_z\hat{\mathbf{z}}$. Here, $\hat{\mathbf{x}}$, $\hat{\mathbf{y}}$, and $\hat{\mathbf{z}}$ are the basis vectors of the Cartesian coordinate system. Then, a strong external magnetic field $B_0\hat{\mathbf{z}}$ is applied to the atom, which defines its quantization axis as the z-axis. Under these conditions, the total polarizability of the atomic state state $|i\rangle$ is

$$\alpha^i = \alpha^i_{\mathrm{S}}(\omega) + \alpha^i_{\mathrm{V}}(\omega)\frac{m_i}{J_i}\mathrm{Im}(\epsilon_x^*\epsilon_y) + \alpha^i_{\mathrm{T}}(\omega)\frac{3m_i^2 - J_i(J_i+1)}{2J_i(2J_i-1)}[3\cos^2(\theta_p) - 1], \tag{2.15}$$

where $\alpha_{\mathrm{S}}$ is the scalar polarizability, $\alpha_{\mathrm{V}}$ is the vector polarizability and $\alpha_{\mathrm{T}}$ is the tensor polarizability. Furthermore, we denote the angular momentum of the atomic state $|i\rangle$ as $J_i$ and the quantum number that describes the projection of $J_i$ along the z-axis as $m_i$. The angle between the polarization vector and the quantization axis is given by $\theta_p$. We realize that the components of the polarization vector $\epsilon_{x,y,z}$ are purely real when the electromagnetic field is linearly polarized, which we assume to be the case for our optical lattices. Therefore, the vector polarizability contribution in Eqn. (2.15) vanishes due to the term $\mathrm{Im}(\epsilon_x^*\epsilon_y)$. The remaining scalar and tensor parts depend on the parameters $\omega$ and $\theta_p$, which are usually experimentally accessible. Therefore, the total polarizability $\alpha^i$ can be tuned by tuning these parameters. In the following Sections, we discuss how this tunability results in special conditions for the state-dependent lattices such as the magic and the tune-out conditions.

## 2.2 State-dependent optical lattices

After presenting an overview of optical lattices, we proceed with discussing state-dependent optical lattices. State-dependent trapping is the ability of trapping atoms selectively, based on their internal quantum states. With this ability, state-dependent lattices can enable certain quantum simulation [15, 16] and quantum computation schemes [52]. In

this Section, we discuss three special types of state-dependent lattices. Then, we describe the quantum simulation scheme that is relevant for our work.

### 2.2.1 Types of state-dependent lattices

In Eqn. (2.15), we give the expression for the polarizability of an atomic state. For an atom with a ground and an excited state, the value of the polarizability is different for each state, leading to state-dependent traps. Certain types of state-dependent lattices can be created by tuning the atomic polarizability. As mentioned in Sec. 2.1.3, the polarizability can be tuned by changing the wavelength of light or the angle of polarization with respect to the quantization axis. In the following, we only consider the wavelength dependence of the polarizability and discuss the special cases of magic, anti-magic and tune-out wavelengths.

*Magic wavelength* When the polarizability of the ground state $\alpha^g(\omega)$ equals the polarizability of the excited state $\alpha^e(\omega)$ for a certain wavelength, the potential seen by the ground state atom is identical to the potential seen by the excited state atom. This wavelength is known as the magic wavelength.

*Anti-magic wavelength* When the polarizabilities have equal magnitude and opposite sign, i.e., $\alpha^g(\omega) = -\alpha^e(\omega)$, the lattice depths are equal but the attractive potential points have a spatial separation of $\lambda/4$. This wavelength is known as the anti-magic wavelength.

*Tune-out wavelength* Tune-out wavelength is the wavelength where one of the polarizabilities $\alpha^g(\omega)$ or $\alpha^e(\omega)$ equals zero. This leads to an optical lattice potential that traps one state, while leaving the other state untrapped. In such optical lattices, the untrapped state has a higher mobility compared to the other state due to the lack of confinement by the optical lattice. In this thesis, we refer to the tune-out wavelength that does not trap the state $|i\rangle$ as the $|i\rangle$ state tune-out wavelength.

### 2.2.2 Simulation of light-matter interfaces

Tune-out lattices can enable certain simulations of light-matter interfaces. To understand this, we consider an optical lattice in which the excited state atoms see a deep lattice potential while the ground state atoms see a shallow lattice potential. To achieve this condition, the lattice is set slightly detuned from the tune-out wavelength. This results in the ground state atoms being able to "hop" freely from one lattice site to the neighboring lattice site. This process is known as tunneling. The frequency of this process is given by the tunneling rate $J/\hbar$, where $J$ is the tunneling parameter. In this lattice, the tunneling of the excited state atoms is not allowed due to the deep trapping potential that these atoms see. Then, an on-resonant laser light is used to couple the two states. This coupling induces Rabi oscillations with a frequency of $\Omega$. When a de-excitation occurs from the excited state to the ground state, the atom becomes free to move in the shallow lattice,

which resembles the process of a matter-wave emission. This process can be used to simulate photon emission in certain nanophotonic structures, which is difficult to realize classically. Furthermore, we can extend the simulation to two dimensions by using a 2D lattice potential. We illustrate a visualization of this scheme in Fig. 2.1, which is adapted from Ref. [38].

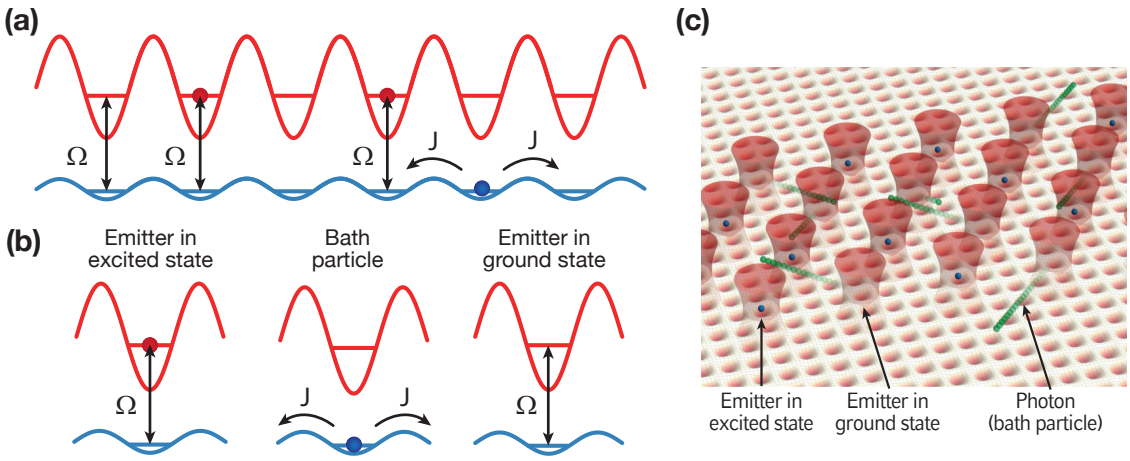


**Figure 2.1** Quantum simulation of light-matter interfaces (adapted from Ref. [38]). **(a)** Excited and ground state atoms in a state-dependent lattice. While the ground state atoms can tunnel through the lattice with the tunnelling parameter $J$, the excited state atoms are tightly confined. A resonant beam induces Rabi oscillations with a Rabi frequency of $\Omega$. **(b)** Different conditions that can occur in a lattice site, corresponding to a quantum emitter or a bath particle (photon). **(c)** An illustration of the presented simulation scheme in a 2D lattice.

## 2.3 $^1S_0$ and $^3P_2$ states of strontium

In a previous work of our research team, the trapping of $^3P_0$ atoms in a one-dimensional $^1S_0$ tune-out lattice is demonstrated as a proof-of-principle experiment, paving the way for the first quantum simulation experiments with strontium in state-dependent lattices [43]. The $^1S_0 - {}^3P_0$ transition offers long excited state lifetimes due to its narrow linewidth of $\sim 1$ mHz, which provides us a technical advantage. However, one main obstacle that limits us still remains, which are the intensity fluctuations of the lattice field that broaden the transition frequency. The $^3P_0$ atoms in the $^1S_0$ tune-out lattice are particularly prone to these intensity fluctuations, because the $^3P_0$ atoms are trapped in the intensity maxima of the lattice sites due to the positive polarizability of the $^3P_0$ state at the $^1S_0$ tune-out wavelength. Therefore, we shift our focus to the $^3P_2$ state, which has a negative polarizability at the $^1S_0$ tune-out wavelength. Due to this property, $^3P_2$ atoms are trapped in the intensity minima of the lattice sites, making the system less sensitive to intensity fluctuations. Furthermore, the $^1S_0 - {}^3P_2$ transition also has a narrow linewidth of $< 1$ mHz,

which provides us with the same technical advantages as $^3\mathrm{P}_0$.

Another advantage of using the $^3\mathrm{P}_2$ state is the ability of addressing a single 2D layer in a 3D lattice by using the magnetic sensitivity of this state. This can be achieved by using a magnetic field gradient that creates a spatially varying frequency shift in the $^1\mathrm{S}_0 - {}^3\mathrm{P}_2$ transition due to the Zeeman effect. To prepare a 2D lattice layer, we can use a magic lattice and excite the atoms to the $^3\mathrm{P}_2$ state in the desired lattice layer, while removing the atoms in the other layers using the $^1\mathrm{S}_0 - {}^1\mathrm{P}_1$ transition. A proof-of-principle single-layer isolation scheme is presented in Refs. [38] and [45]. Therefore, our current motivation is to construct a 2D $^1\mathrm{S}_0$ tune-out lattice to trap $^3\mathrm{P}_2$ atoms and to study matter-wave emission dynamics in 2D, which remains largely unexplored.

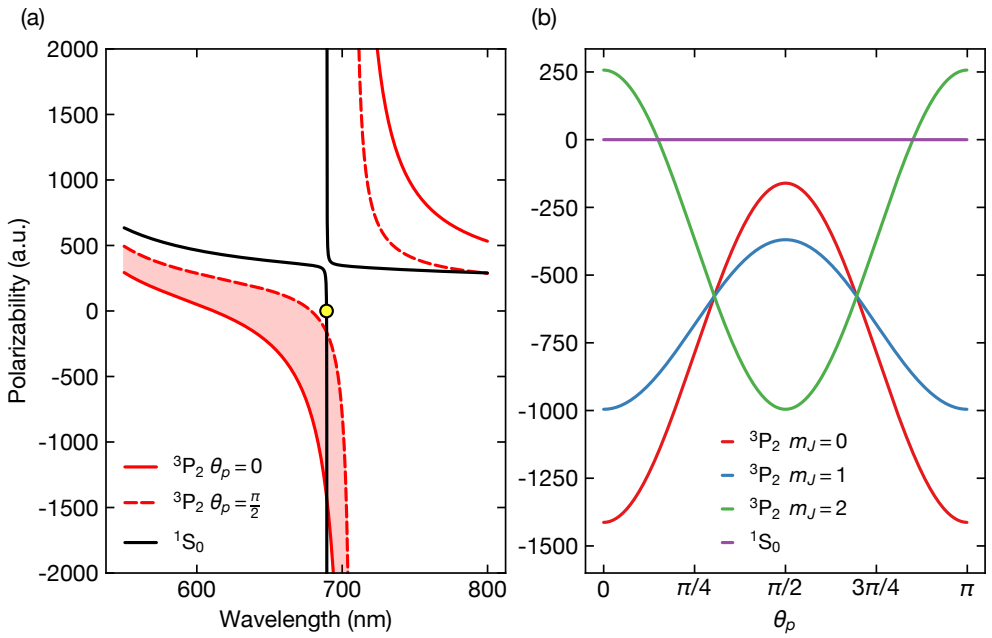


**Figure 2.2** **(a)** Calculated polarizabilities of the $^1\mathrm{S}_0$ and the $^3\mathrm{P}_2$ states as a function of wavelength. The polarizability of the $^3\mathrm{P}_2$ state ($m_J = 0$) is shown in the two extreme cases of $\theta_p = 0$ and $\theta_p = \pi/2$. The yellow marker corresponds to the tune-out wavelength where the polarizability of the $^1\mathrm{S}_0$ state vanishes. **(b)** The polarizabilities of the $^1\mathrm{S}_0$ and the $^3\mathrm{P}_2$ states at the tune-out wavelength as a function of the angle between the lattice polarization and the quantization axis. The $^1\mathrm{S}_0$ state is unaffected by this angle due to its vanishing angular momentum $J = 0$.

The $^1\mathrm{S}_0$ tune-out wavelength was measured experimentally as $689.22222(1)$ nm by our team and this measurement was confirmed by the atomic structure calculations provided by Marianna Safronova. Here, we present the polarizabilities of the $^1\mathrm{S}_0$ and the $^3\mathrm{P}_2$ states obtained from these atomic structure calculations. We plot the polarizabilities in atomic

units as a function of wavelength in Fig. 2.2 (a). In this Figure, we show the polarizability of the $^3\mathrm{P}_2$ state ($m_J = 0$) in the two extreme cases of $\theta_p = 0$ and $\theta_p = \pi/2$ using Eqn. (2.15). We have the ability to tune the polarizability of the $^3\mathrm{P}_2$ state by tuning the angle of the magnetic field (quantization axis) with respect to the lattice polarization. During this tuning process, the polarizability of the $^1\mathrm{S}_0$ state remains constant since it has a vanishing angular momentum $J = 0$, leading to a vanishing tensor polarizability.

In Fig. 2.2 (b), we present the polarizability of the $^3\mathrm{P}_2$ state as a function of $\theta_p$ at the tune-out wavelength where the polarizability is zero for $^1\mathrm{S}_0$. In our experiments, we can only work with angles between $\theta_p = \pi/4$ and $\theta_p = \pi/2$. This precondition is set by the fixed orientation of the magnetic field in our experiment due to other considerations, which are beyond the scope of this thesis. At an angle of $\theta_p = \pi/4$, we calculate the polarizability of the $^3\mathrm{P}_2$ state ($m_J = 0$) as $\alpha = -787$ a.u., where $1$ a.u. $= 4\pi\epsilon_0 a_0^3$ is the atomic unit of polarizability, and $a_0$ is the Bohr radius.

## 2.4 System size enhancement with a crossed cavity

Simulating light-matter interfaces requires large and homogeneous optical lattices. The limitation on the system size is set by the harmonic confinement of the lattice, which is a result of the spatial mode (usually Gaussian) of the laser that is used to create the lattice. This effect results in a varying trap depth throughout the lattice. One way to enhance the system size is to make the laser beam larger. However, this results in shallower lattices due to the reduced intensity of the laser beam. This situation poses a problem for our experiments since it requires us to work with high-power lasers, which are challenging to obtain commercially at the wavelengths that we work with. To overcome this issue, our research team uses a novel experimental apparatus, which is an in-vacuum optical buildup cavity that enhances the intensity of light that is circulating in it. With this technique, we can generate large and deep optical lattices in the buildup cavity.

In this Section, we first introduce the features and the parameters of our optical cavity in which we want to generate the tune-out lattice. Then, we determine the minimum lattice depth requirement that we need to satisfy with the tune-out lattice to minimize the tunneling of the $^3\mathrm{P}_2$ atoms.

### 2.4.1 Crossed cavity

To make large and homogeneous 2D lattices, we use a crossed-cavity configuration, which is made of two orthogonal buildup cavities with their centers intersecting each other. We refer to these cavities as the “minus arm” and the “plus arm” of the crossed cavity. We present a picture of the crossed cavity in Fig. 2.3, which we adapt from Ref. [43]. In Tab. 2.1, we present the most relevant parameters of the crossed cavity. For a more detailed description and the manufacturing procedure of the crossed cavity, we refer the reader

| | |
|---|---|
| Free spectral range | $\nu_{\mathrm{FSR}} = 3$ GHz |
| Cavity linewidth | $\Gamma_{689} = 5.6(2)$ MHz |
| Finesse | $\mathcal{F}_{689} = 533(19)$ |
| Cavity mode waist at 689.2 nm | $w_{689} = 396\ \mu\mathrm{m}$ |
| Enhancement factor | $\Lambda_{689} = 147(5)$ |

**Table 2.1** Important parameters of the crossed cavity relevant for this thesis (data taken from Ref. [43]). The measured quantities are shown with an error.

to Ref. [43].

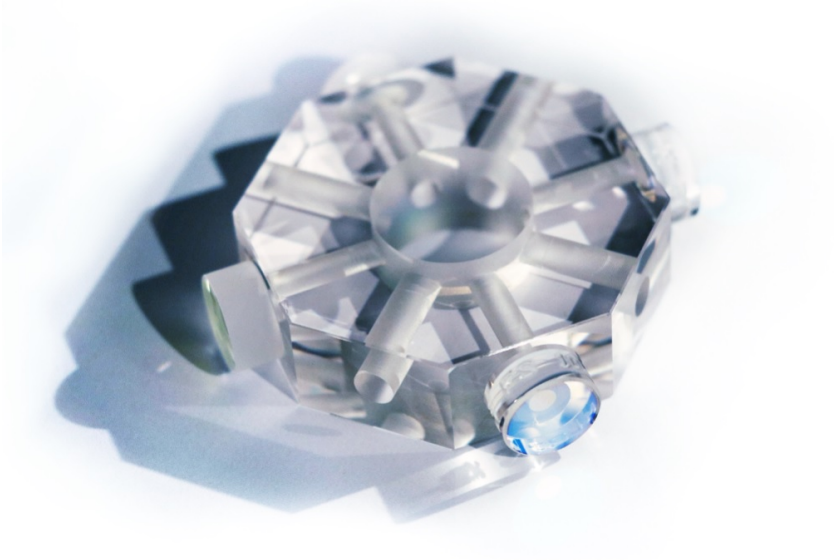

**Figure 2.3** A picture of the crossed cavity (adapted from [43]).

Due to the finite size of the cavity waist (396 $\mu$m), the harmonic confinement effect in the tune-out lattice causes a spatial variation in the $^1\mathrm{S}_0 - {}^3\mathrm{P}_2$ transition frequency. This is due to the fact that a spatial variation in the lattice depth leads to a corresponding shift in the harmonic energy levels of the lattice sites. In Fig. 2.4 (a), we present the calculated variation in the lattice depth as a function of distance from the center of the lattice. In Fig. 2.4 (b), we also present the spatial shift of the transition frequency relative to the ground state of the harmonic trap (at an energy of $\hbar\omega_{\mathrm{tr}}/2$). Due to this limitation, we aim to work near the center of the lattice in our experiments.

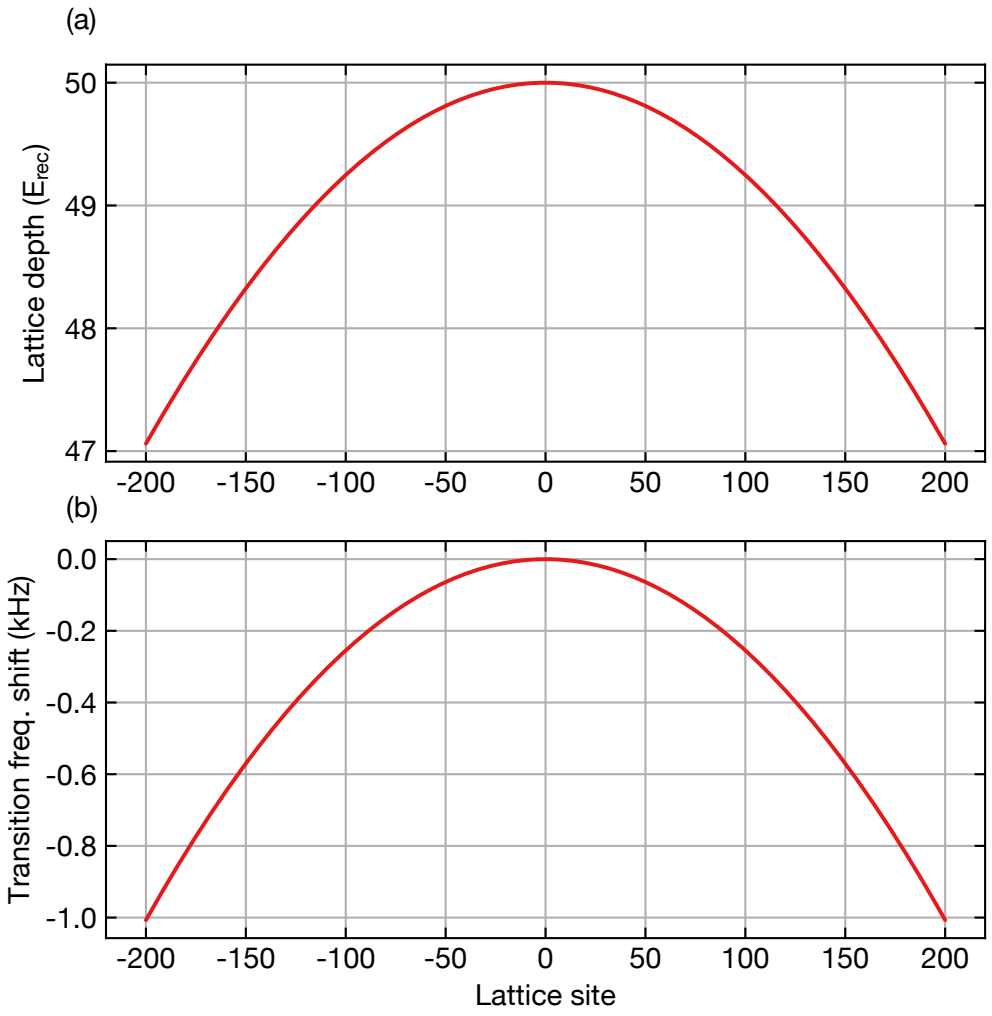


**Figure 2.4** The consequences of the harmonic confinement in the tune-out lattice. **(a)** Lattice depth as a function of the distance from the center of the lattice, expressed in terms of lattice sites. The lattice depth at the center of the gaussian envelope is assumed to be $50\mathrm{E}_{\mathrm{rec}}$. This lattice depth corresponds to a trap frequency of $\sim 68$ kHz. **(b)** The corresponding spatial dependence of the shift in the $^1\mathrm{S}_0 - {}^3\mathrm{P}_2$ transition frequency.

### 2.4.2 Lattice depth requirements

To simulate light-matter interfaces accurately, we need to ensure that the atoms in the excited state $^3\mathrm{P}_2$ do not tunnel to the adjacent lattice sites during the simulation time $\tau_{\mathrm{sim}}$. For this reason, we have certain limitations regarding the lattice depth $V_{\mathrm{e}}$ that the $^3\mathrm{P}_2$ state sees in the tune-out lattice. The lattice depth determines the ratio between the

on-site interaction energy $U$ of the atoms and the tunnelling parameter $J$. By increasing the lattice depth, we can minimize $J$ and suppress tunnelling. In a previous work of our team, a lattice depth of $50\mathrm{E}_{\mathrm{rec}}$ is proposed for a tunnelling rate of $J/\hbar = 1.2\ \mathrm{s}^{-1}$ in the tune-out lattice [43]. We calculate the required input power before each arm of the cavity to achieve this lattice depth using

$$V_{\mathrm{tr}} = \frac{4\Lambda_{689} P_{\mathrm{i}}}{\pi c \epsilon_0 w^2} \alpha_e, \tag{2.16}$$

where $P_{\mathrm{i}}$ is the input power before each arm of the cavity, $\alpha_e$ is the magnitude of the $^3\mathrm{P}_2$ polarizability and $w$ is the cavity mode waist. Using the parameters of the crossed cavity that we present in Sec. 2.4.1 and the calculated $^3\mathrm{P}_2$ polarizability of $\alpha_e = -787$ a.u., we plot the lattice depth as a function of input power $P_{\mathrm{i}}$ in Fig. 2.5. For a lattice depth of $50\mathrm{E}_{\mathrm{rec}}$, we calculate an input power of $P_{\mathrm{i}} \approx 26\ \mathrm{mW}$. We need this input power before each arm of the cavity so that the tunnelling in each direction in the 2D lattice is limited by $J/\hbar = 1.2\ \mathrm{s}^{-1}$. Note that at angles $\theta_p$ higher than $\pi/4$, the magnitude of the polarizability decreases. Therefore, we need higher input powers at these angles.

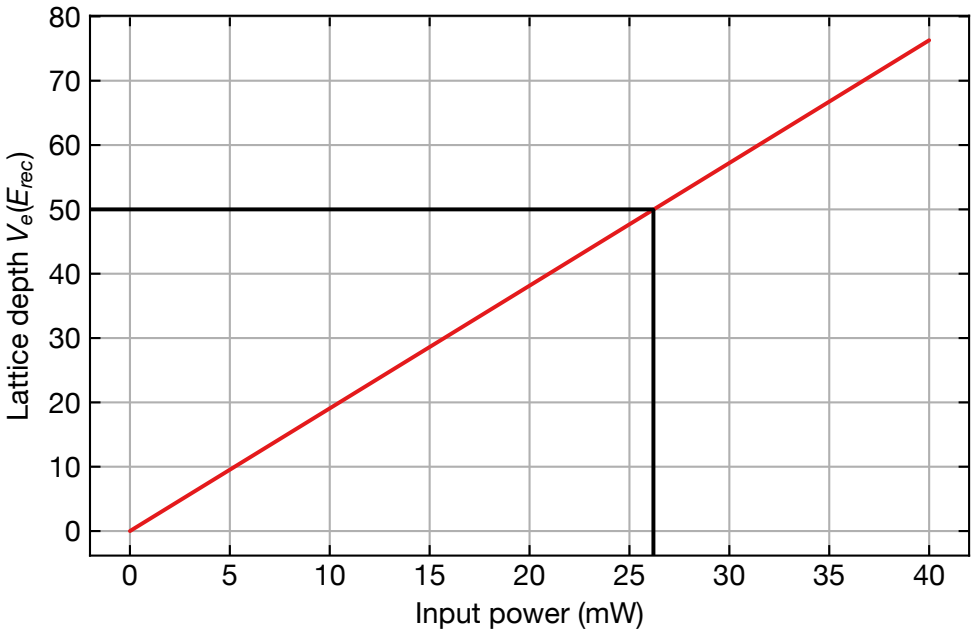


**Figure 2.5** The lattice depth that the $^3\mathrm{P}_2$ state sees as a function of input power before the cavity. A lattice depth of $50\mathrm{E}_{\mathrm{rec}}$ corresponds to an input power of $\sim 26\ \mathrm{mW}$.

As a last remark, we calculate the lattice depth that the $^1\mathrm{S}_0$ atoms see as a function of detuning from the tune-out wavelength. Around the tune-out wavelength, a linear fit to the polarizability of the $^1\mathrm{S}_0$ state yields a slope of $\frac{d\alpha_g}{d\nu} = 2.44$ a.u./GHz. Hence, we can

write

$$V_{\mathrm{g}} = \frac{4\Lambda_{689} P_{\mathrm{i}}}{\pi c \epsilon_0 w^2} \frac{d\alpha_g}{d\nu} \Delta\nu, \tag{2.17}$$

where $\Delta\nu$ is the detuning from the tune-out wavelength. We present the ground state lattice depth as a function of detuning in Fig. 2.6.

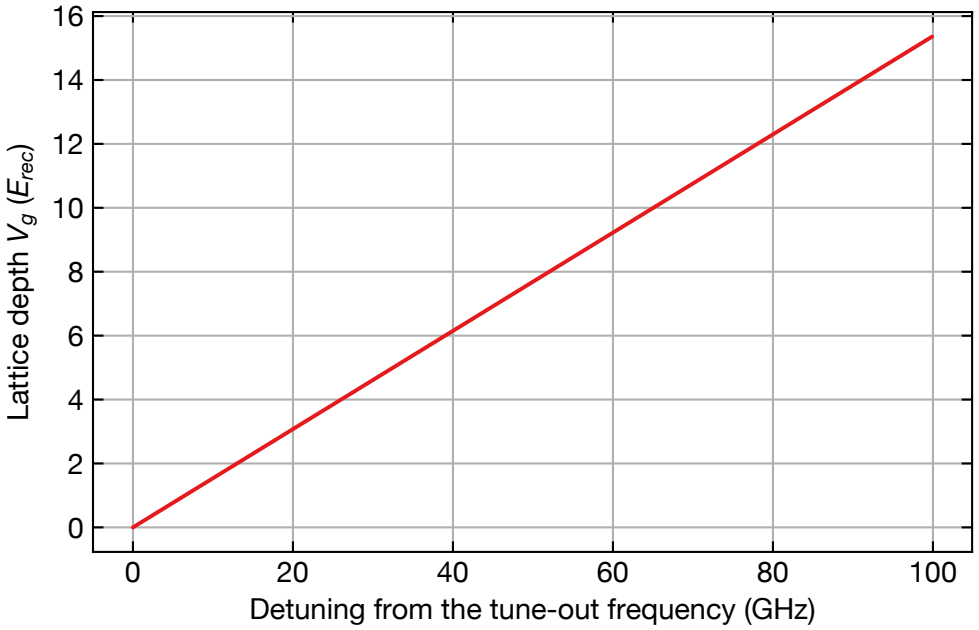


**Figure 2.6** The lattice depth that the $^1\mathrm{S}_0$ state sees as a function of detuning from the tune-out wavelength. An input power of $P_{\mathrm{i}} = 26\ \mathrm{mW}$ is used in this calculation.

## Conclusion

Here, we have discussed the basics of atom-light interactions in the context of optical lattices. Furthermore, we introduced the concept of state-dependent lattices and their role in simulating light-matter interfaces. We also motivated the use of the $^3\mathrm{P}_2$ atoms in these simulations. We presented the crossed-cavity design that our research team uses and we estimated the spatial variation of the $^1\mathrm{S}_0 - {}^3\mathrm{P}_2$ transition frequency resulting from the harmonic confinement of the lattice. Lastly, we estimated a required power of $26\ \mathrm{mW}$ to make tune-out lattices with a lattice depth of $50\mathrm{E}_{\mathrm{rec}}$ for the excited state. To make these lattices, we need a laser source that can provide us the required optical power.

# Chapter 3

# Tune-out Lattice Lasers

Trapping ultracold strontium atoms in a tune-out lattice requires a coherent laser source. For this purpose, this Chapter is dedicated to the description of the lasers that we use to generate light for the tune-out lattice. We refer to these lasers as the lattice lasers. We begin our discussion by introducing one of the lasers, which is an external-cavity diode laser. Then, we proceed by describing the components that are involved in the injection locking of a slave laser diode to this external-cavity diode laser. Lastly, we present the beam-shaping methods that we use to obtain a Gaussian laser beam.

## 3.1 DL Pro

Due to their commercial availability and practicality, we use diode lasers to generate light for the tune-out lattice. Typically, a laser diode with an internal cavity that is made of its rear and front facet emits light with a linewidth of up to 100 MHz without an external cavity configuration to provide optical feedback. However, we have higher requirements for the linewidth of our laser, because a broad linewidth leads to heating of the atoms due to the frequency-to-amplitude noise conversion in the crossed cavity [43]. Furthermore, since the modes of the crossed cavity have a linewidth of 5.6 MHz, a laser with a 100 MHz linewidth would only be partially amplified, leading to the loss of optical power and shallower lattices. Therefore, we cannot use laser diodes alone to generate our tune-out lattices. Instead, we use a grating-stabilized external-cavity diode laser (ECDL) that combines an anti-reflection coated laser diode with a reflection grating as a wavelength-selective component to achieve a narrower linewidth. In this Section, we describe the features of our grating-stabilized ECDL (Toptica, DL Pro) and the laser controller that we use to operate the laser.

The laser diode that this ECDL uses has a rear and a front facet. The front facet has an anti-reflection coating whereas the rear facet is reflective. The light exiting the front facet of the laser diode is collimated with a lens. Then, a diffraction grating diffracts the collimated light into multiple beams with different angles and these angles depend on the wavelength of each diffracted beam. Our ECDL uses a Littrow configuration [53] for this grating, which means that the first order of the diffracted beam is reflected back along the direction of the incident light. This way, a selected wavelength is sent back to the rear facet of the laser diode. Hence, a wavelength-selective external cavity is formed between the grating and the rear facet of the diode. Since the finesse of the external cavity is

higher than the finesse of the internal cavity due to the high-reflectivity and wavelength selectivity of the grating, the external cavity reduces the linewidth of the emitted light down to 100 kHz according to the data sheet of our ECDL. Furthermore, the wavelength can be coarsely tuned over a large range simply by rotating the diffraction grating using a screw integrated outside the laser housing design for convenience. The grating is also attached to a piezo element which lets us change the cavity length by applying a voltage on the piezo element. This capability provides us with fine-tuning of the emission frequency. Lastly, our ECDL uses thermoelectric elements to adjust the temperature of the laser diode. This adjustment changes the length of the internal cavity and thereby the emission wavelength.

We use a commercial laser controller (Toptica, DLC Pro) to control the parameters of the laser, i.e., the operating current of the laser, temperature of the laser diode and the piezo voltage we apply on the piezo element. The laser controller has a digital user interface which lets us adjust all these parameters using a touch panel. Furthermore, we can apply an external voltage to the laser controller using two ports labeled on its front panel as “fast in” and “fine in” to modulate and control any of these parameters in an automatic manner.

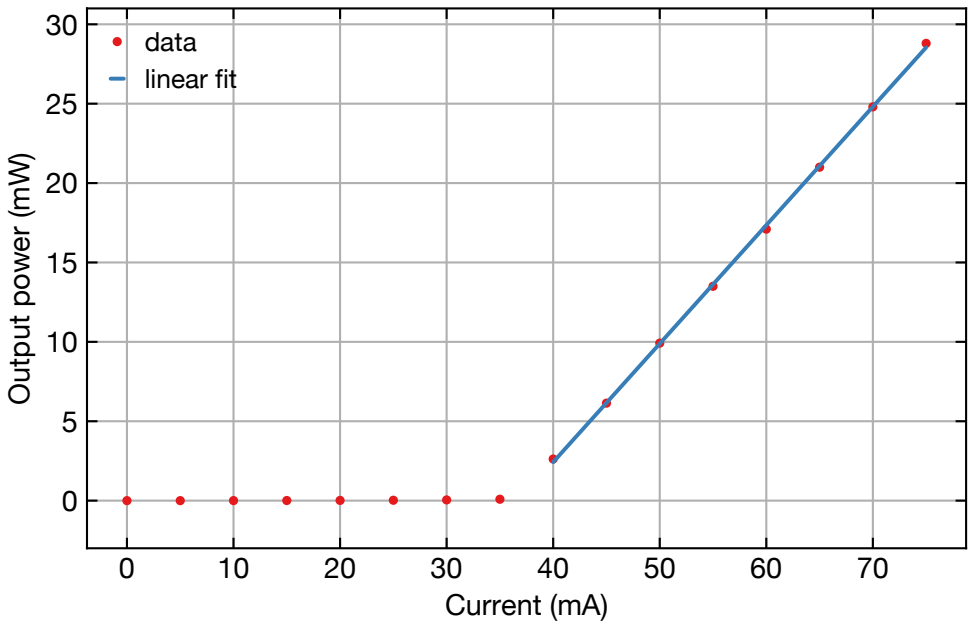


**Figure 3.1** Characterization of the output power of our master laser. The laser has a threshold current of 40 mA. We find a maximum optical output power of 28.8 mW at an operating current of 75 mA.

We measure the output power of the ECDL with a power meter at different operating currents, which we adjust with the laser controller interface. The laser starts lasing only after exceeding an operating current of 40 mA. This current is referred to as the threshold current. We fit a linear function to the output powers we measured above the threshold current, which we show in Fig. 3.1 and find a slope of 0.75 W/A. The laser has a maximum operating current of 75 mA which provides us with 28.8 mW output power.

As a last remark, we introduce the concepts of mode hopping and mode-hop free tuning range. A mode hop occurs when our laser is operating in the desired mode of the external cavity, but it suddenly switches to another mode of the external cavity. This situation may happen when the length of the internal cavity changes slightly different than the length of the external cavity, which results in a different combination of internal and external cavity modes operating at the same time. Therefore, we see a sudden change in the frequency of the laser. To maximize the frequency range over which no mode hopping occurs, we set a proportionality constant (feed forward) between the piezo voltage and the operating current of the laser diode. Since a change in the current on the laser diode will change the effective length of the internal cavity, we can make sure that the mode overlap between the internal and the external cavity is maximized by choosing the correct feed-forward constant. The maximum laser frequency range over which mode hopping can be eliminated is called the mode-hop free tuning range.

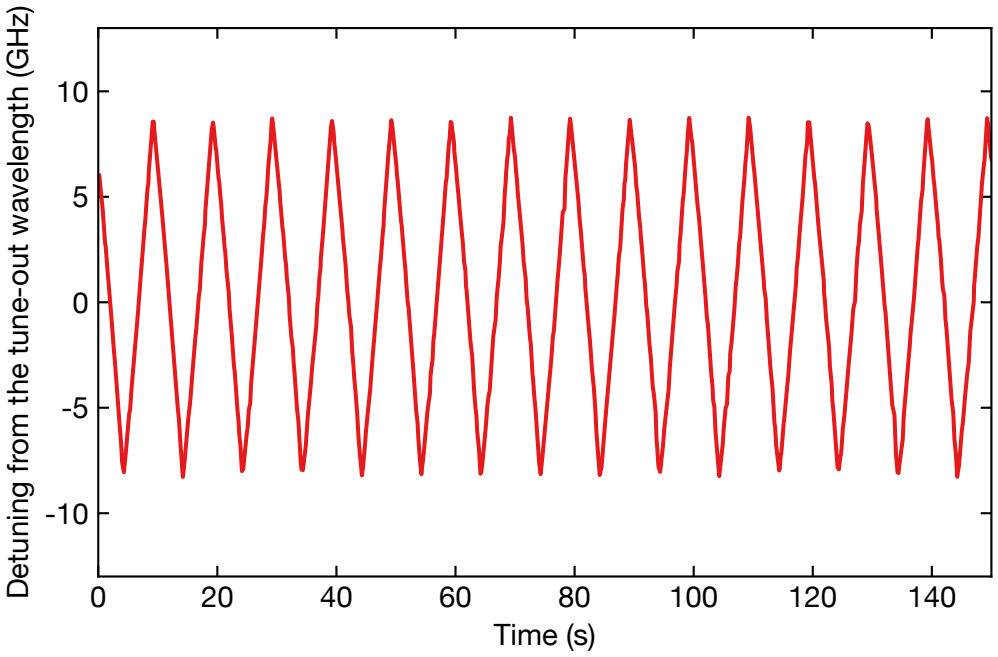


**Figure 3.2** Mode hop-free tuning range of the ECDL around the tune-out wavelength.

To optimize the feed forward, we tune our laser to the tune-out wavelength first with the piezo voltage. Then, we scan the piezo voltage while monitoring the laser frequency on a wavelength meter (HighFinesse, WS7). We gradually increase the scan amplitude until we see a sudden change in the frequency of the laser, i.e., a mode hop. We tune the feed-forward constant until the mode hop disappears. We repeat this procedure until tuning the feed-forward constant cannot improve the continuous scan of the laser frequency anymore. We measure a mode-hop free tuning range of about 16 GHz with a scan frequency of 0.1 Hz, a piezo voltage offset of 51.8 V, a piezo voltage scan amplitude of 50 V, a feed-forward parameter of -0.082 mA/V and at an operating current of 70 mA and a temperature of 21.5°C (see Fig. 3.2).

## 3.2 Injection locking

The maximum optical power that our ECDL can provide is 28.8 mW, which cannot provide the minimal required power of 26 mW per cavity arm. Therefore we use the method of injection locking to amplify the optical power of the ECDL. In this way we have more power available at the desired wavelength and can make deeper tune-out lattices. In a conventional injection locking setup, there is a powerful slave laser diode with an internal cavity which gets optically seeded by a master laser. When the slave diode is free running, i.e., without being seeded, it operates with lower spectral mode quality compared to the master laser. When we seed this free-running diode with our master laser (DL Pro), the free-running slave laser emits light with the same spectral properties of the master laser. This process can take place when the seed beam is mode-matched to the cavity of the injection-lock laser diode and if the spectra of the two lasers are overlapping. The former can be ensured by fine alignment and the latter requires the tuning of diode temperature and the operating current. Furthermore, the injected light must be much stronger than the spontaneously emitted photons of the free-running laser diode. We refer the reader to Ref. [54] for a mathematical model of the injection locking process.

### 3.2.1 Design and components

As we show in Fig. 3.3, the injection lock module consists of a mount for the slave diode, an optical isolator (Thorlabs, IO-5-670-HP) to make sure that reflections from optical components in the setup do not reach the diode, half wave plates (CeNing, WPZ1220-L/2-689nm) for polarization alignment, a fiber coupler (Thorlabs, PAF2-7B) for monitoring the injection locking status and another fiber coupler for collimating the seed light out of a fiber. Furthermore, we use a polarizing beam splitter (PBS) to split a portion of the laser light and send it to the fiber that we use for monitoring the injection locking process. The laser light that is transmitted through this PBS exits the injection lock module to be used in the experiment.

Here, we describe the most important parts of our injection lock setup. A more detailed description of an older but similar version of our setup can be found in Ref. [55]. We use

two of these modules for our experiment. One of these injection lock modules is for the minus arm and the other one is for the plus arm of the enhancement cavity.

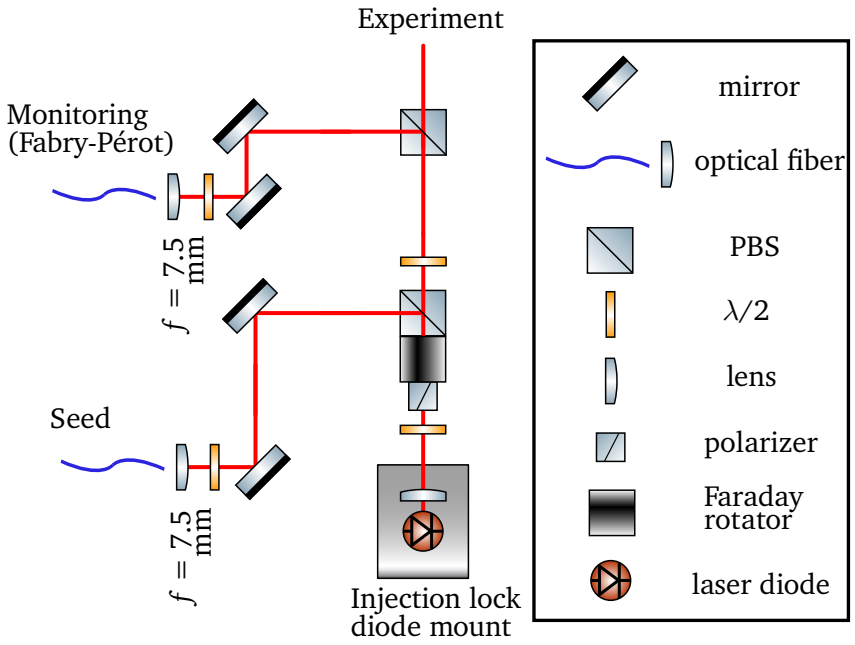


**Figure 3.3** An illustration of the injection lock module. The module consists of a mount for the slave laser diode, an optical isolator for the suppression of back reflections from the setup, half wave plates for polarization alignment, an optical fiber for monitoring the injection locking status and another optical fiber for providing the slave laser diode with the seed light from the master laser.

### Laser diode

We use two commercially available diodes (Ushio, HL69001DG) as slave laser diodes. According to the data sheet, these laser diodes have an optical output power of 210 mW. We characterize these lasers by measuring their output power after a collimation lens for different operating currents (see Fig. 3.4). The laser diodes start lasing only when the operating current exceeds approximately 40 mA. We fit a linear function to the output powers we measured above the threshold current and find a slope of 1.02 W/A for the minus arm laser and 0.98 W/A for the plus arm laser. The maximum operating current value for these laser diodes is 270 mA. However, we run them at 250 mA at most since running them at maximum power may reduce their lifetime. At 250 mA, we get 199 mW for the slave laser diode of the minus arm and 190 mW for the plus arm.

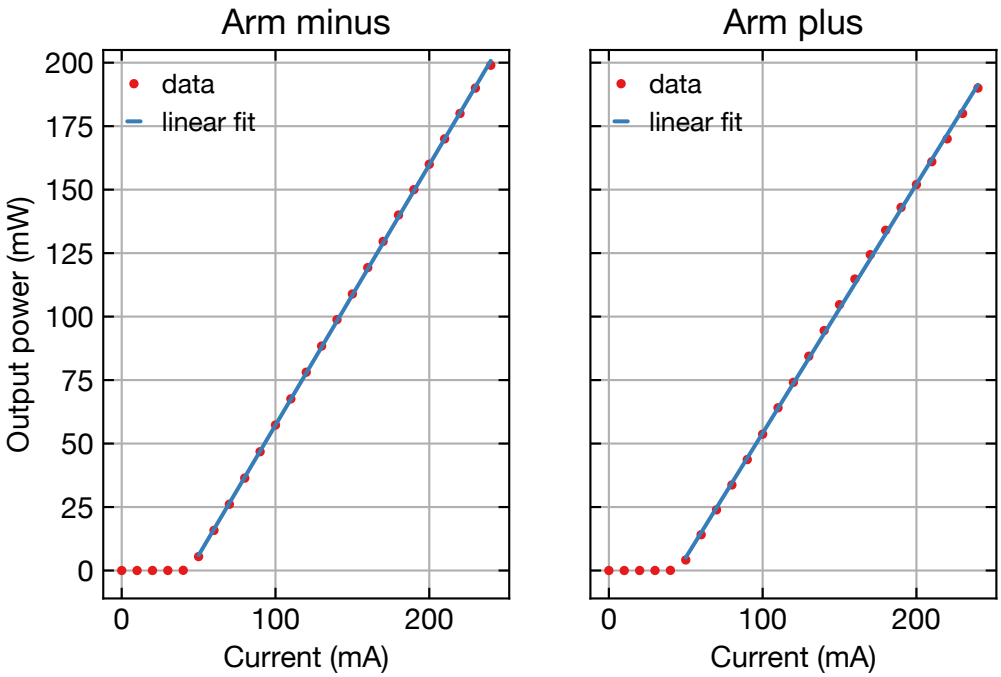


**Figure 3.4** Characterization of the output power of our slave laser diodes. The laser diodes have a threshold current of approximately 40 mA. We find a maximum optical output power of 199 mW for the slave laser diode of the minus arm and 190 mW for the plus arm at an operating current of 250 mA.

### Diode mount

We use a custom-designed laser diode mount in the injection lock modules. We show an illustration of this diode mount in Fig. 3.5. The diode mount is made of a laser head, a suspender under the laser head (heat sink) and a mount that attaches these parts to the optical breadboard. We place the laser diode and the collimating lens (Thorlabs, C230TMD-B) inside the laser head. Then, we collimate the beam by moving the lens inside the laser head using a spanner wrench. However, this lens can only partially collimate the beam since the beam that exits the slave laser diode has an elliptical spatial mode and the two axes of the ellipse diverge at different rates. The elliptical spatial mode is a result of divergence angles of the emission not being equal in the two orthogonal axes of the beam profile. We collimate the fast-diverging axis of the laser beam to prevent the beam from becoming too large quickly. We address the collimation of the slow-diverging axis of the beam later in this Chapter.

To ensure that the laser beam leaves the laser straight, the diode mount is designed in such a way that it can be tilted in the up-down and left-right direction. This degree of freedom is achieved by the non-matching screw and screw hole sizes at the attachment

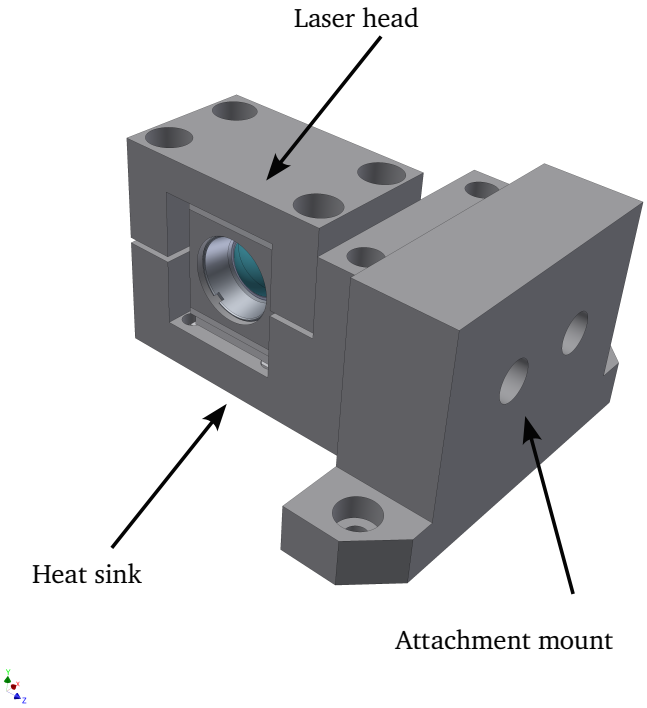


**Figure 3.5** A schematic of the diode mount.

point of the laser head and the sink. We loosen these screws, tilt the laser head and make the beam leave the laser as straight as possible. Then, we fix the screws again. After placing all the optical components of the injection lock setup, we use a beam profiler (Cinogy, CMOS-1201) to ensure that the beam is not being blocked by these components.

During operation, heat is generated in the laser by the electric current flowing through the laser diode. We detect the temperature with a thermistor (RS components, $3\,\mathrm{k}\Omega$) and stabilize it using a Peltier element (RS components) driven by a temperature controller (Thorlabs, ITC 4001). We glue the thermistor inside a small hole on the laser head right next to the diode. We use a thermally conductive and electrically insulating glue to ensure the best possible contact between the laser and thermistor without creating a short circuit. We place the Peltier element between the laser head and the suspender. This way, the Peltier element mediates the heat transfer between the laser head and the optical breadboard. Then, we tune the temperature with a commercial temperature controller (Thorlabs, ITC 4001) and monitor the spectrum of the emitted light on an optical spectrum analyser (Ando, AQ6315E) to overlap the spectral modes of the free-running diode laser with the tune-out wavelength. We see this overlap at a temperature of 26°C.

### Optical isolator

A parasitic reflection from an optical component in the beam path of our injection lock lasers can make the laser unstable because such a reflection is an additional feedback to the injection locking process. This feedback might amplify other spectral modes because the phase relation between the injected field and the internal field will be different due to the introduction of the back-reflected field. Furthermore, a high-intensity reflection can permanently damage the laser diode. With optical isolators, we can suppress the back reflection so that the lasers do not become unstable.

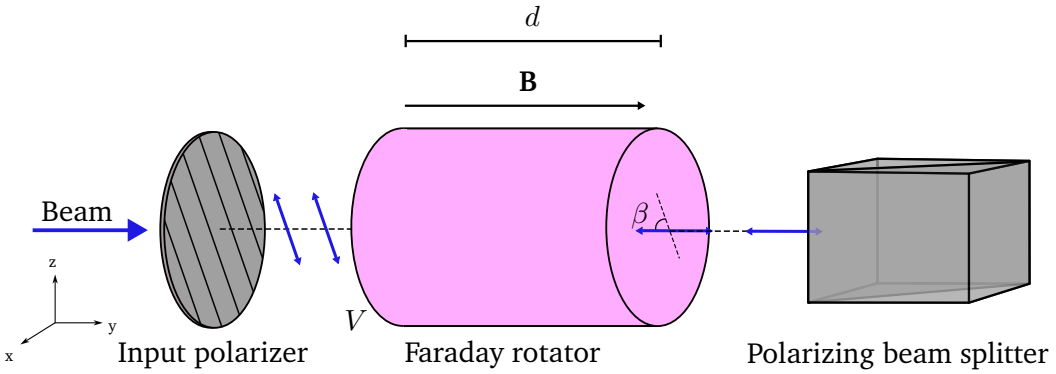


**Figure 3.6** An illustration of the parts of our optical isolator. We define $d$ and $V$ as the length and the Verdet constant of the Faraday rotator and $B$ as the magnitude of the magnetic field. The beam from the slave laser diode enters the isolator from the input polarizer that polarizes the beam with an angle of $\beta$ with respect to the x-axis. The Faraday rotator rotates the polarization of light in the anticlockwise direction by $\beta$. The beam exits the Faraday rotator with a polarization parallel to the x-axis. Ideally, this beam is transmitted through the PBS. Any back-reflected light from the setup is blocked by the input polarizer when $\beta = 45^\circ$ in this configuration.

We use tunable Faraday isolators (Thorlabs, IO-5-670-HP) to suppress this back reflection. Faraday isolators normally consist of three parts: a Faraday rotator, an input and an output polarizer. However, we cannot use the isolator with an output polarizer since we want to inject our seed beam to the slave laser diode by overlapping the beams on a polarizing beam splitter (PBS) cube. We use a PBS cube because it provides us with two orthogonal beam paths. Therefore, we remove the output polarizer from our optical isolator and replace it with a PBS (CeNing, 675-710 nm) as we show in Fig. 3.6. The extinction ratio of our PBS is specified as 500:1, which means that the optical power of the light polarized in the unwanted axis amounts to $1/500$ times the power of the light polarized in the wanted axis of our PBS.

In this part, we first discuss how our optical isolator works. Then, we explain how we align it in our beam path. The Faraday rotator of our optical isolator consists of a material which rotates the polarization plane of linearly polarized light when a magnetic

field parallel to the direction of light propagation is present. The rotation angle is given by

$$\beta = dBV, \tag{3.1}$$

where $d$ is the length of the material, $V$ is the Verdet constant of the material and $B$ is the magnitude of the magnetic field. When a beam propagates in the direction of the magnetic field, this rotation is anticlockwise, assuming we are looking toward magnetic field direction. When the beam propagation is anti parallel to the magnetic field, the rotation is also anticlockwise from the same perspective. Therefore, the polarization of a beam that passes through the Faraday rotator and comes back rotates by $2\beta$ in total in the anticlockwise direction. When $\beta = 45°$, the back-reflected light's polarization becomes orthogonal to its initial polarization. Then, we can align the input polarizer to transmit the input beam, while blocking the reflected beam, thereby isolating it. Furthermore, the PBS blocks the back-reflected components that are linearly polarized at the wrong angle or that are not linearly polarized at all. Such situations can arise due to polarization deviations introduced by various optical components in our setup.

We align the isolator by rotating the Faraday rotator and the input polarizer together and making sure that the seed power is maximized. Since the light reflected back from the setup goes through the other PBS port, it has a polarization orthogonal to the seed light. Therefore, we also maximize the suppression of the back-reflected light with our alignment method. Furthermore, the Faraday rotator we use is wavelength dependent, meaning that the magnitude of the rotation angle $\beta$ depends on the wavelength of light. The wavelength dependency of the Faraday rotator affects the Verdet constant, which in turn makes $\beta$ slightly deviate from $45°$. This deviation means that we have to rotate the Faraday rotator together with the input polarizer slightly more (or less) than $45°$ with respect to the back-reflected light for better suppression. This extra rotation misaligns the polarizing beam splitter with the light that is coming out of the Faraday rotator. A small fraction of this light reflects from the polarizing beam splitter, instead of being transmitted, and goes to the master laser setup where it is suppressed by the optical isolator of the master laser.

### Scanning Fabry-Pérot interferometer

To ensure that injection locking takes place between our master and slave laser diodes, we need to monitor the spectrum of the slave laser diodes. In principle, we can do this with an optical spectrum analyser. However, optical spectrum analysers are expensive instruments that are usually used for more complicated tasks. Furthermore, the spectrum analyser we possess in our laboratory (Ando, AQ6315E) has a single optical fiber input port, which makes it inconvenient for us since we want to monitor both of our slave lasers at the same time. Therefore, we assemble a scanning Fabry-Pérot cavity setup and measure its transmission spectrum to monitor the status of the injection locking for both slave lasers. Here, we present our setup and discuss how we couple light into this cavity.

We also present an illustration of this setup in Fig. 3.7.

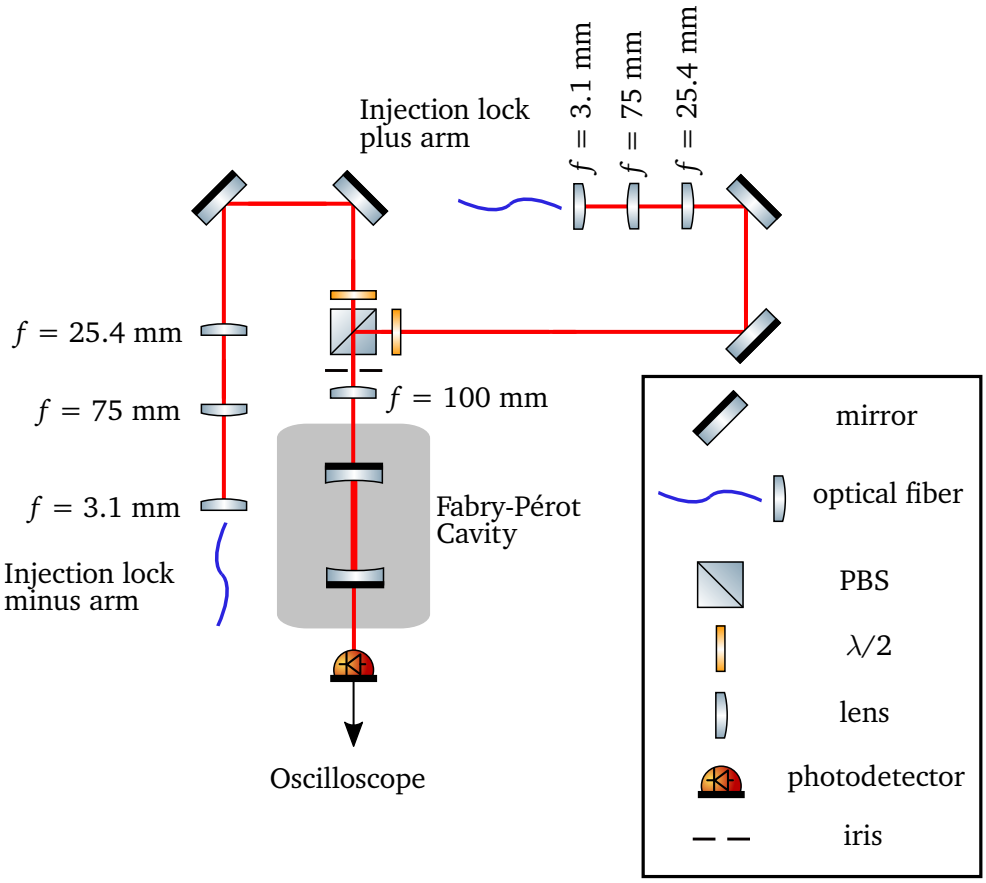


**Figure 3.7** An illustration of the Fabry-Pérot setup. We match the spatial modes of both beams from the injection lock lasers with the spatial mode of the Fabry-Pérot cavity using a telescope and a lens. We overlap the beams on a PBS. We detect the transmission signal through the cavity using a photodetector and monitor the injection locking status with this signal.

First, we use polarization-maintaining fibers to guide a portion of the laser light from the injection lock modules to the Fabry-Pérot cavity setup. We refer to these fibers as the monitoring fibers. We collimate the beams using aspherical lenses (Thorlabs, A220TM-B). Then, each beam goes through a telescope made of two plano-convex lenses in back-to-back configuration right after the aspherical lenses to adjust the beam diameter. After overlapping the beams on a PBS, we use another plano-convex lens with a focal length of $f = 100\,\mathrm{mm}$ in front of the cavity to match the spatial mode of the beam with the

$TEM_{00}$ mode of the cavity. Since our cavity is confocal, we place this mode-matching lens roughly 100 mm away from the cavity center to match the modes optimally.

We want to get the correct beam diameter right before this mode-matching lens using the telescope. We calculate the required beam waist in front of the mode-matching lens from Ref. [56] with

$$w_0^{\mathrm{inc}} = \frac{\lambda f}{\pi w_0^{\mathrm{cav}}}, \tag{3.2}$$

where $w_0^{\mathrm{cav}}$ is the waist of the cavity, $\lambda$ is the wavelength of light and $f$ is the focal length of the mode-matching lens. With $w_0^{\mathrm{cav}} = 74\ \mu\mathrm{m}$, we calculate a required beam diameter of $2w_0^{\mathrm{inc}} = 592\ \mu\mathrm{m}$. Since both beams that are collimated out of the fibers have a diameter of 1.8 mm, we use telescopes with 3:1 focal length ratios to reduce the beam size from 1.8 mm to 0.6 mm. Note that the lens with the larger focal length should come first for diameter reduction. The lenses in the telescopes have focal lengths of $f_1 = 75$ mm and $f_2 = 25.4$ mm. We collimate the beam by placing these lenses $f_1 + f_2$ apart.

| Operating current, minus arm (mA) | Operating current, plus arm (mA) |
|---|---|
| 60.8 | 61.8 |
| 77.4 | 73.2 |
| 92.6 | 87.9 |
| 106.8 | 102.2 |
| 120.2 | 115.9 |
| 132.9 | 128.9 |
| 144.8 | 141.3 |
| 156.3 | 152.9 |
| 167.7 | 164.4 |
| 178.3 | 175.6 |
| 188.9 | 186.1 |
| 198.9 | 196.3 |
| 208.7 | 206.3 |
| 218.1 | 216.2 |
| 227.2 | 225.4 |
| 235.9 | 234.9 |
| 245.0 | 244.0 |

**Table 3.1** Table of currents which lock the slave laser diodes to the master laser at an operating temperature of 26°C. The seed power is 5 mW on the minus arm and 6 mW on the plus arm.

We can change the length of the cavity in a periodic manner by applying a voltage ramp on a piezo element that is attached to one of the cavity mirrors. We use a ramp generator (Thorlabs, SA201) to apply this ramp. We see transmission only when the resonance

condition of the cavity is met,

$$L = n\lambda/2, \tag{3.3}$$

where $L$ is the length of the cavity and $n$ is a positive integer. We monitor this transmission with a photodetector after the Fabry-Pérot cavity. After a rough alignment of the beam to the cavity, several cavity modes are visible in the transmission spectrum of the cavity. To maximize the power in the $TEM_{00}$ mode and minimize the higher-order modes, we proceed according to the following steps. We align one of the beams first by beam walking with two mirrors and mode matching with the 100 mm lens before the cavity. We use an iris to make sure that we are hitting the center of the mode-matching lens. Then, we align the other beam by beam walking with two mirrors only. After this procedure, we only see the lowest-order modes of the cavity in the transmission data. We assume that these modes are 1.5 GHz away from each other since the free spectral range of the cavity is specified as 1.5 GHz. Then, we convert the time axis of the transmission data to a frequency axis using this information and display it in Fig. 3.8.

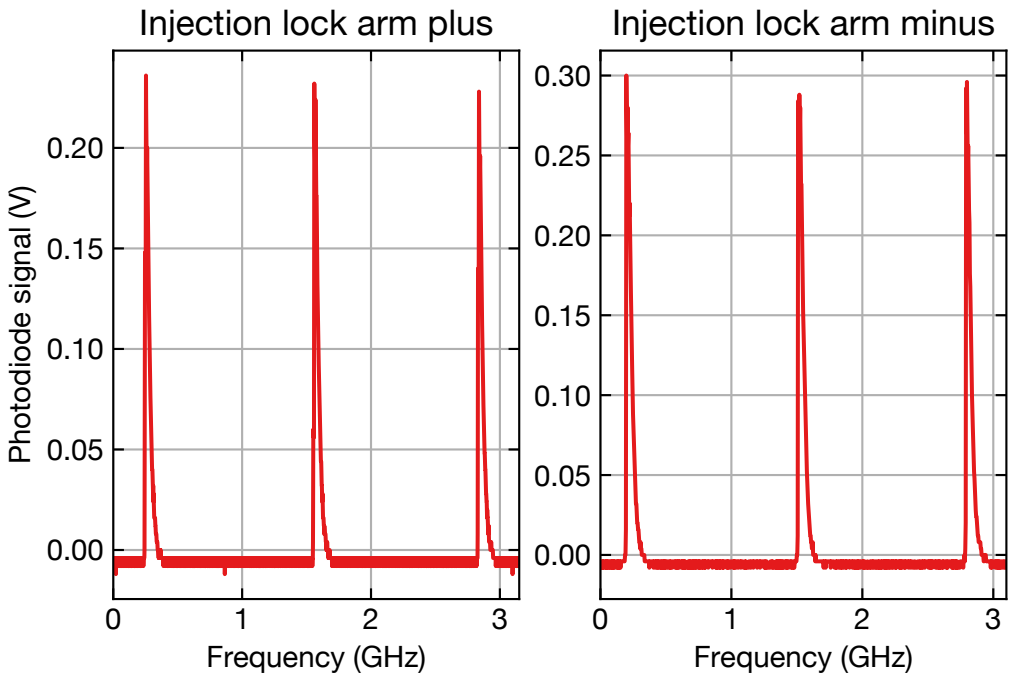


**Figure 3.8** Transmission spectrum from our scanning Fabry-Pérot cavity when the slave laser diodes are locked to the master laser.

After going through these steps, we can now monitor the injection locking status. We observe that injection locking occurs at certain currents flowing through the slave laser diode. These currents are given in Tab. 3.1 with the corresponding seeding powers and

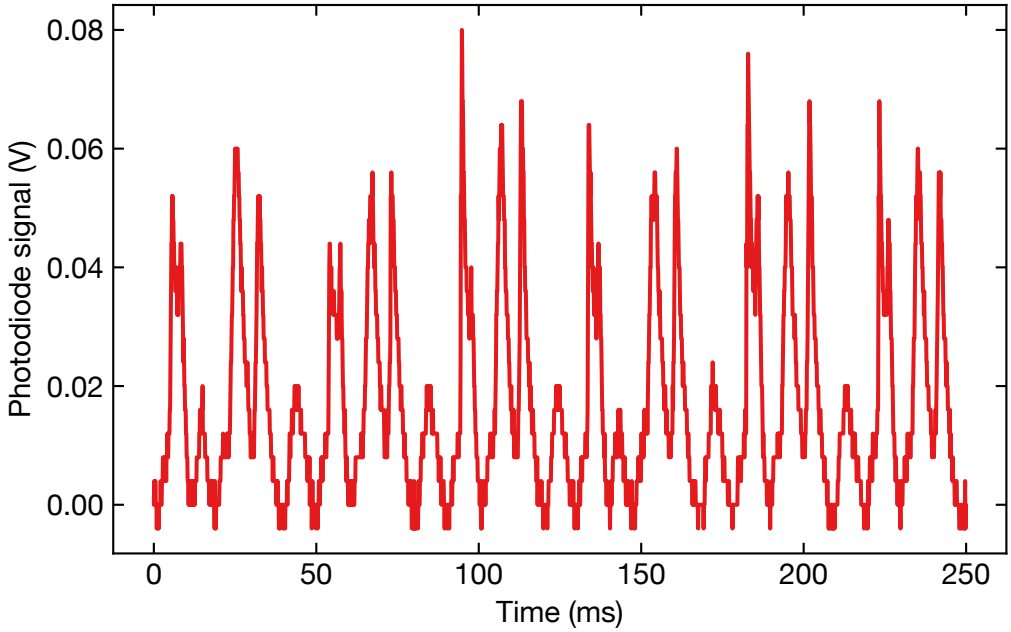


**Figure 3.9** Transmission signal from our scanning Fabry-Pérot cavity when the slave laser diodes are not locked to the master laser.

temperature. If the slave diode is not locked to the seed light, its broadband emission spectrum is visible as a collection of peaks in the transmission spectrum like in Fig. 3.9. Therefore, we can lock the injection lock lasers by making sure that we see equally spaced peaks in the transmission spectrum just like in Fig. 3.8.

## 3.3 Beam shaping with cylindrical telescopes

In our experimental setup, we need a collimated laser beam that has a Gaussian spatial mode throughout its propagation distance since we want to maximize the coupling efficiencies into the optical fibers we will use to guide the laser beam to other places. Therefore, we need to ensure that the beam that exits the injection lock module has a Gaussian mode and is collimated. However, as mentioned before, we collimate only the fast-diverging axis of the laser beam with the collimation lens that we insert inside the laser head of the diode mount. Here, we describe how we collimate the slow-diverging axis of the beam while making sure that the spatial mode of the beam is Gaussian.

We achieve the collimation by using a cylindrical telescope that consists of two cylindrical lenses. These cylindrical lenses have one flat surface and one curved surface. The curved surface acts only on one axis of the beam inbound to the surface, while leaving the

other axis unchanged. Therefore, cylindrical lenses make beam shaping and collimation along a single axis possible. We show an illustration of this method in Fig. 3.10.

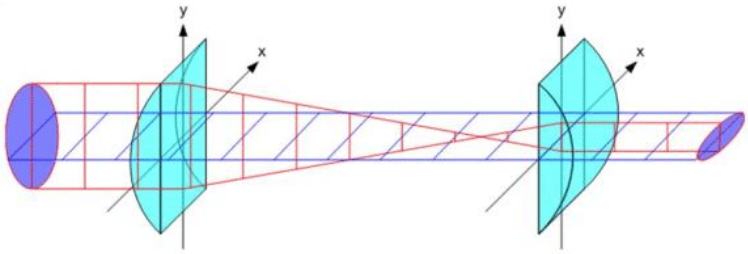


**Figure 3.10** Beam shaping with a cylindrical telescope made of two cylindrical lenses. The beam that is incident from the right has an elliptical profile. This profile is corrected and the beam exits the telescope from the left with a uniform Gaussian shape. This figure is adapted from Ref. [57].

To calculate the focal lengths of the cylindrical lenses we should use in our setup, we measure the diameter of the beams that exit the injection lock modules with a beam profiler (Cinogy, CMOS-1201). We measure a beam diameter of 1.8 mm in the horizontal axis and 1.4 mm in the vertical axis of the injection lock laser of the minus arm. Here, the vertical axis is the uncollimated axis (slow-diverging axis). Therefore, we use two cylindrical lenses with focal lengths of 30 mm and 40 mm to match the lengths of the axes. We place the lenses roughly 70 mm away, making sure that the flat surfaces are facing each other. Then, we let the beam propagate for several meters and monitor the cross section of the beam with a beam profiler at this distance. We adjust the vertical beam diameter to be as small as possible at this distance by moving one of the cylindrical lenses with respect to the other. Then, we fix the positions of the lenses. By going through this process, we make sure that the beam has a Gaussian mode and it is collimated in both axes. We go through the same process for the injection lock laser we use for the plus arm. We measure a beam diameter of 1.5 mm in the horizontal direction (collimated) and 1 mm in the vertical direction (uncollimated). We use cylindrical lenses with focal lengths of 12.7 mm and 20 mm. Then, we collimate the beam with the same procedure as above.

## Conclusion

In this Chapter, we introduced the lasers that we use to make tune-out lattices. We described the properties of our master laser and explained the role of each essential component in our injection lock modules. With the laser diodes that we use for these modules, we were able to reach an output power of $\sim 190\,\mathrm{mW}$. We presented how we can monitor the injection locking status by monitoring the spectrum of the slave lasers using a Fabry-Pérot cavity setup. Then, we discussed the cylindrical telescopes that we use in our setup to obtain collimated Gaussian beams from these lasers.

# Chapter 4

# Lattice Laser Stabilization Scheme

One of the main goals in our experiment is to ensure the stable operation of our lattice lasers, since the instability of these lasers would result in the instability of the tune-out lattice that we generate with them. More specifically, we are interested in stabilizing the intensity and the frequency of these lasers.

We start this Chapter by briefly discussing the parametric heating mechanism, which may heat the strontium atoms in the tune-out lattice due to intensity noise. Then, we give an overview of the Pound-Drever-Hall (PDH) technique, which can help us minimize the parametric heating in the lattice. We discuss the construction procedure of two electro-optic modulators that take part in the PDH technique. This discussion is followed by the measurement of the crossed-cavity modes near the tune-out wavelength. We need to know the resonant frequencies of these cavity modes to implement the PDH technique in the crossed cavity. Then, we present the main experimental setup and describe the components that are involved. Additionally, we prevent the long-term frequency drifts of the master laser by locking its frequency to a frequency comb. After implementing these stabilization schemes, we characterize the stability of the laser system by measuring the relative intensity noise. Lastly, we calculate the heating rate of atoms in the lattice.

## 4.1 Noise-induced parametric heating

One of the limitations we encounter with our optical lattices is laser-induced heating arising from the intensity fluctuations of the optical lattice. This process is called parametric heating. Parametric heating of atoms may reduce the trapping lifetime since it leads to the excitation of atoms into higher motional states. In this Section, we discuss how this heating mechanism takes place and how it affects the atoms in the lattice by following the derivations of Ref. [46].

For an atom confined in a harmonic optical trap, the intensity noise of the light field creates a proportional noise in the spring constant of the harmonic trap. We write the Hamiltonian of the noisy trap as

$$\hat{H} = \frac{\hat{p}^2}{2M} + \frac{1}{2} m\omega_{\mathrm{tr}}^2 [1 + \epsilon(t)]\hat{x}^2, \tag{4.1}$$

where $\hat{p}$ is the momentum operator acting on the coordinate $\hat{x}$. Furthermore, $\epsilon(t)$ is the time-dependent fractional intensity noise defined as

$$\epsilon(t) = \frac{I(t) - \langle I(t) \rangle}{\langle I(t) \rangle}, \tag{4.2}$$

where $I(t)$ is the intensity of light field in the optical trap and $\langle I(t) \rangle$ stands for the time average of the intensity. From Eqn. (4.1), the rate of heating can be obtained using time-dependent perturbation theory. We refer the reader to Ref. [46] for this derivation. The heating rate is the time-derivative of the average energy of the atom

$$\langle \dot{E} \rangle = \Gamma_\epsilon \langle E \rangle, \tag{4.3}$$

where $\langle E \rangle$ is the average energy and $\Gamma_\epsilon$ is the heating rate constant defined as

$$\Gamma_\epsilon = \pi^2 \nu_{\mathrm{tr}}^2 S_\epsilon(2\nu_{\mathrm{tr}}). \tag{4.4}$$

Here, $S_\epsilon(2\nu_{\mathrm{tr}})$ is the one-sided spectral density of the fractional intensity noise. The one-sided spectral density is expressed as

$$S_\epsilon(\omega) = \frac{2}{\pi} \int_0^{+\infty} \mathrm{d}\tau \langle \epsilon(t)\epsilon(t+\tau) \rangle \cos \omega\tau. \tag{4.5}$$

From Eqn. (4.4), we see that the spectral density of the intensity noise contributes to the parametric heating process at twice the trapping frequency. Therefore, we want to minimize the optical lattice intensity noise at this frequency.

For our tune-out lattices, there are two contributions to the intensity noise. The first contribution is simply the intensity noise of our lasers. The second contribution arises from a combination of laser frequency noise and the cavities that we use to create the optical lattices. When we tune the laser frequency to the cavity resonance frequency, frequency noise of the laser gets converted to intensity noise due to the frequency dependence of the light intensity circulating in the cavity. In Ref. [43], the fractional intensity noise arising from this conversion is given by

$$\epsilon(t) = 4 \frac{\delta_L^2(t)}{\Delta\nu_C^2}, \tag{4.6}$$

where $\delta_L$ is the frequency deviation of the laser from the cavity resonance and $\Delta\nu_C$ is the linewidth of the cavity mode.

Both of the contributions we mentioned enhance the parametric heating in the tune-out lattice. In a previous work, a cavity-lattice stabilization scheme has been proposed to reduce these effects [43]. In the following Sections, we discuss a similar stabilization scheme that we employ.

## 4.2 Pound-Drever-Hall technique

The Pound-Drever-Hall (PDH) technique is a frequency stabilization scheme which involves locking the frequency of a laser to the resonance frequency of a reference cavity. In our case, we want to stabilize our laser's frequency to the resonance frequency of the crossed cavity. This process requires the generation of sidebands around the carrier frequency of light by modulating the optical phase using an electro-optic modulator (EOM). In this Section, we first give a theoretical overview of how EOMs generate sidebands and how these sidebands are used to generate an error signal for the PDH method. Then, we describe the procedure that we go through to construct two EOMs for our setup.

### 4.2.1 Sideband generation with electro-optic modulators

Sidebands can be generated by modulating the phase of the light field using EOMs. Here, we discuss how EOMs operate in general and how they modulate the phase of a light field, resulting in a carrier wave and two or more sidebands. We follow the derivations in Ref. [58] and in Ref. [59].

EOMs use the Pockels electro-optic effect. This effect describes the linear response of the refractive index of an optical medium to an applied electric field. Such an optical medium is called a Pockels medium. The Pockels effect is usually directional, i.e., the refractive index variation only occurs for a beam linearly polarized in parallel to a certain axis of the Pockels medium, called the crystal axis. The applied electric field also needs to be parallel to this axis. We illustrate the Pockels effect in Fig. 4.1 where we consider a Pockels medium with a cuboid shape. We apply a voltage across the crystal axis of the cuboid to generate the electric field. The modulated refractive index is

$$n_{\parallel}(|\mathbf{E}|) = n_0 - \frac{1}{2} r n_0^3 |\mathbf{E}|, \tag{4.7}$$

where $n_0$ is the unmodulated refractive index of the medium, $r$ is the electro-optic coefficient of the medium and $|\mathbf{E}|$ is the magnitude of the electric field. Such a modulation of the refractive index of the material results in the modulation of the phase of the light field. The relation between the phase and the refractive index change $\Delta n_{\parallel} = n_{\parallel}(|\mathbf{E}|) - n_0$ is given by

$$\Delta\phi = 2\pi \Delta n_{\parallel} \frac{L}{\lambda}, \tag{4.8}$$

where $L$ is the length of the medium and $\lambda$ is the wavelength of light. Combining this equation with Eqn. (4.7) we obtain

$$\Delta\phi = \pi \frac{V}{V_\pi}. \tag{4.9}$$

Here, $V$ is the voltage applied across the the two faces of the medium (see Fig. 4.1) given by $V = |\mathbf{E}|d$ where $d$ is the distance between the two faces. Furthermore, $V_\pi$ is the

half-wave voltage which shifts the phase of the light field by $\pi$, given as

$$V_\pi = \frac{d}{L}\frac{\lambda}{r n_0^3}. \tag{4.10}$$

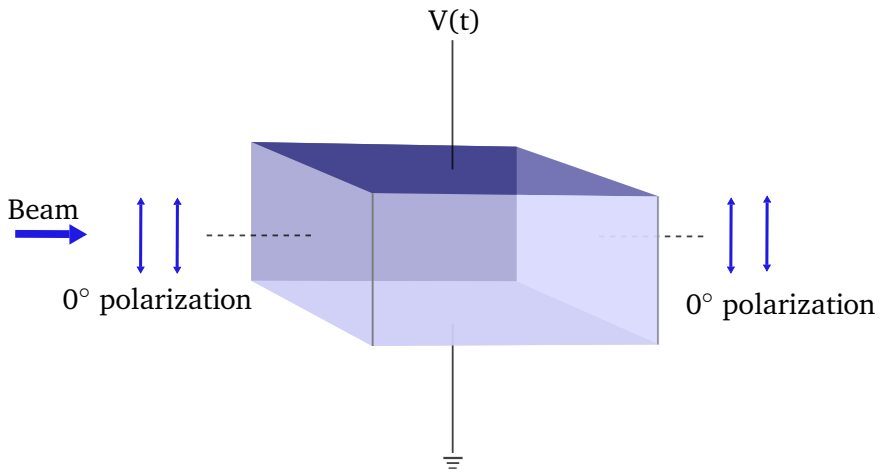


**Figure 4.1** An illustration of the Pockels effect. An oscillating voltage $V(t)$ is applied along the crystal axis of a Pockels medium with a cuboid shape to generate an electric field in this axis. We send a light field that is linearly polarized along the crystal axis of the Pockels medium trough the Pockels cell. The phase of the beam is modulated due to the varying refractive index of the medium induced by the varying electric field. Sidebands around the carrier frequency of light can be generated using this effect.

If we apply an oscillating voltage to the Pockels medium with a frequency of $\Omega$ and a modulation depth of $\beta$, i.e., $V(t) = \frac{V_\pi}{\pi}\beta \sin \Omega t$, the phase-modulated light field can be expressed as

$$E_{\mathrm{mod}}(t) = E_0 \exp(i\omega t) \exp(i\beta \sin \Omega t), \tag{4.11}$$

where $\omega$ and $E_0$ are the frequency and the electric field amplitude of the unmodulated light field, respectively. We can expand this expression in terms of Bessel functions of the first kind $J_k(\beta)$ as

$$E_{\mathrm{mod}}(t) = E_0[J_0(\beta)\exp(i\omega t) + \sum_{k=1}^{\infty} J_k(\beta)\exp(it(\omega + k\Omega)) + \sum_{k=1}^{\infty}(-1)^k J_k(\beta)\exp(it(\omega - k\Omega))]. \tag{4.12}$$

The terms that are oscillating with $\omega + k\Omega$ and $\omega - k\Omega$ in this expression correspond to $k^{\mathrm{th}}$ order sidebands and $E_0 J_k(\beta)$ corresponds to their amplitude. By choosing the modulation depth $\beta$ such that $J_0(\beta)$ and $J_1(\beta)$ are much stronger than the higher order Bessel functions, we can ensure that only the carrier and first sideband frequencies that are $\Omega$ away from the carrier are dominant in the spectrum of the beam. In Fig. 4.2 we take the square of these Bessel functions and plot them as functions of modulation depth.

These curves correspond to the power in the sidebands normalized to the total power. We display this quantity as percentage. According to Ref. [59], the optimal sideband-to-carrier power ratio for the PDH technique is 42 %, which is satisfied at a modulation depth of $\beta = 1.08$ where $|J_2(\beta)|^2 = 1.7$ %. Therefore, we can neglect the effect of the higher-order sidebands. Then, Eqn. (4.12) reduces to

$$E_{\mathrm{mod}}(t) = E_0[J_0(\beta)\exp(i\omega t) + J_1(\beta)\exp(i(\omega+\Omega)t) - J_1(\beta)\exp(i(\omega-\Omega)t)]. \quad (4.13)$$

Hence, two sidebands are obtained. Note that the sidebands differ in phase by $\pi$ due to the minus sign in front of the last term in Eqn. (4.13).

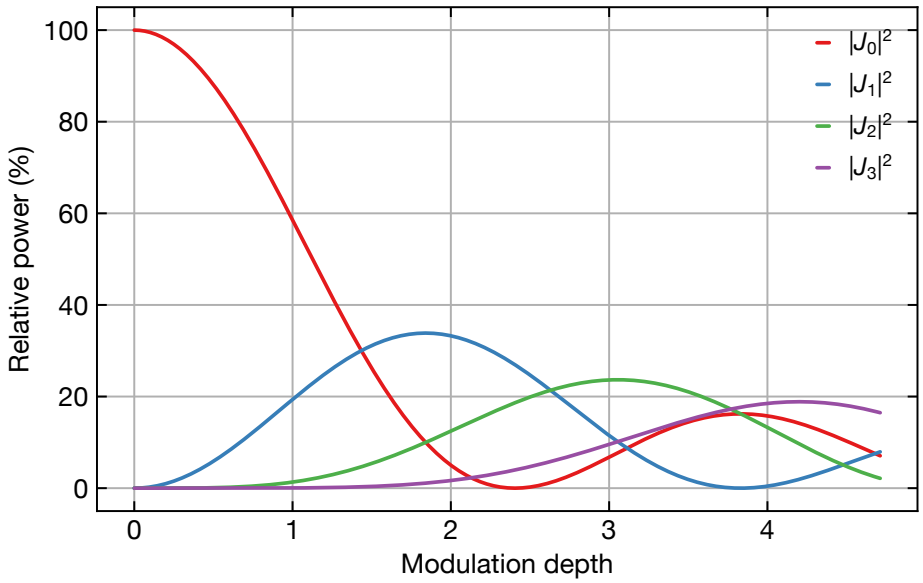


**Figure 4.2** The relative power of the carrier and the sidebands as a function of the modulation depth, which is a unitless quantity. The relative power is given by the square of the Bessel functions of the first kind $J_n$. Here, we only display the orders $n = 0, 1, 2, 3$.

### 4.2.2 Derivation of the error signal

The main goal of the PDH technique is to generate an error signal using the sidebands and to stabilize this signal by feeding it to a proportional-integral-derivative (PID) circuit. Here, we mathematically obtain the error signal following the derivations of Ref. [59]. First, we consider the back-reflection of a beam from a reference cavity. Therefore, we first introduce the reflection coefficient of a cavity as

$$F(\omega) = \frac{E_{\text{ref}}}{E_{\text{in}}} = \frac{r(e^{i(\omega-\omega_{\text{cav}})/\nu_{\text{FSR}}} - 1)}{1 - r^2 e^{i(\omega-\omega_{\text{cav}})/\nu_{\text{FSR}}}}, \tag{4.14}$$

where $E_{\text{ref}}$ is the reflected light field amplitude, $E_{\text{in}}$ is the light field amplitude incident to the cavity, $r$ is the amplitude reflection coefficient of the cavity mirrors, $\nu_{\text{FSR}}$ is the free spectral range of the cavity and $\omega_{\text{cav}}$ is the resonance frequency of the cavity. Then, the reflection of the light field in Eqn. (4.13) from the reference cavity is

$$E_{\text{ref}} = E_0 \exp(i\omega t)[F(\omega)J_0(\beta) + F(\omega+\Omega)J_1(\beta)\exp(i\Omega t) - F(\omega-\Omega)J_1(\beta)\exp(-i\Omega t)]. \tag{4.15}$$

We are interested in the power of the reflected beam since that is what we can experimentally measure with a photodetector. Therefore, we take the absolute square of Eqn. (4.15) to obtain the power $P_{\text{ref}}$ which gives

$$\begin{aligned} P_{\text{ref}} = P_{\text{DC}} + 2|E_0|^2 J_0(\beta)J_1(\beta)\{&\text{Re}[F(\omega)F^*(\omega+\Omega) - F^*(\omega)F(\omega-\Omega)]\cos(\omega t) \\ &+\text{Im}[F(\omega)F^*(\omega+\Omega) - F^*(\omega)F(\omega-\Omega)]\sin(\Omega t)\} + \mathcal{O}(2\Omega), \end{aligned} \tag{4.16}$$

where $P_{\text{DC}}$ stands for non-oscillating terms. At low modulation frequencies ($\Omega \ll \nu_{\text{FSR}}$), we can perform the approximation

$$F(\omega)F^*(\omega+\Omega) - F^*(\omega)F(\omega-\Omega) \approx -2i\text{Im}[F(\omega)]. \tag{4.17}$$

Therefore, the cosine term in Eqn. (4.16) vanishes. Furthermore, we neglect the $2\Omega$ terms and simplify Eqn. (4.16) as

$$P_{\text{ref}} \approx P_{\text{DC}} - 4|E_0|^2 J_0(\beta)J_1(\beta)\text{Im}[F(\omega)]\sin(\Omega t). \tag{4.18}$$

Then, we define the error signal as

$$\epsilon(\omega) \equiv -4|E_0|^2 J_0(\beta)J_1(\beta)\text{Im}[F(\omega)]. \tag{4.19}$$

The power of the light reflected from the cavity becomes

$$P_{\text{ref}} \approx P_{\text{DC}} + \epsilon(\omega)\sin(\Omega t). \tag{4.20}$$

We can measure the power using a photodetector. Then, we can use a mixer to demodulate the signal of the photodetector with another AC signal $\sin(\Omega t+\phi)$ that has a frequency $\Omega$ and a phase $\phi$ with respect to the signal applied to the Pockels medium. The output signal of the mixer is the product of the two inputs

$$P_{\text{mixed}} = [P_{\text{DC}} + \epsilon(\omega)\sin(\Omega t)]\sin(\Omega t + \phi). \tag{4.21}$$

We use the trigonometric identity

$$\sin(A)\sin(B) = \frac{1}{2}[\cos(A-B) - \cos(A+B)], \tag{4.22}$$

to simplify Eqn. (4.21) which becomes

$$P_{\text{mixed}} = \frac{1}{2}\epsilon(\omega)\cos(\phi) + P_{\text{DC}}\sin(\Omega t + \phi) - \frac{1}{2}\epsilon(\omega)\cos(2\Omega t + \phi). \tag{4.23}$$

Then, we use a low-pass filter with a cut-off frequency lower than $\Omega$ to filter the last two terms of Eqn. (4.23). We adjust the remaining term $\frac{1}{2}\epsilon(\omega)\cos(\phi)$ by changing the cable length through which we send the AC signal $\sin(\Omega t + \phi)$, thereby tuning $\phi$. When $\phi$ becomes $\pi$, the DC term becomes $\frac{1}{2}\epsilon(\omega)$. Hence, we can obtain the error signal directly after the low-pass filter. When the frequency of the laser $\omega$ is equal to the frequency of the cavity resonance $\omega_{\text{cav}}$, the error signal $\epsilon(\omega)$ vanishes. Furthermore, the error signal changes sign around $\omega = \omega_{\text{cav}}$. Therefore, the sign of the measured error signal tells us whether the frequency of the laser is higher or lower than the frequency of the cavity resonance. We input the error signal to a PID controller whose output modulates the frequency of our laser. The laser frequency modulation is carried out by acousto-optic modulators (AOM) which we will explain in detail later in this Chapter.

### 4.2.3 Home-built electro-optic modulators

We build two electro-optic modulators to generate sidebands for the PDH technique. We provide a picture of our home-built EOM design including the housing for the crystal in Fig. 4.3. We use lithium niobate ($LiNbO_3$) crystals as the Pockels medium of EOMs. These crystals are manufactured with two electrodes for applying a voltage along their crystal axis. The crystals are also equipped with anti-reflection coatings between the wavelengths 630 nm - 920 nm to reduce reflections from their surfaces. When we apply an oscillating voltage to the crystal, we want to ensure that the electrical power is optimally transferred to the crystal (the load) for a modulation as deep as possible. To achieve this, we perform impedance matching with a resonant LC circuit that contains an inductor (L) and a capacitor (C), illustrated in Fig. 4.4. Impedance matching occurs when the impedance of the power source $Z_S$ equals to the complex conjugate of the impedance of the load $Z_L^*$. By building a resonant LC circuit between the modulation source and the crystal, we can adjust $Z_S$ and make it equal to $Z_L^*$. Then, we want to confirm that the impedance matching is successful. To achieve this, we measure the fraction of the total power that reflects back to the source from the load. The ratio of the reflected power $P_{\text{ref}}$ to the incident power $P_{\text{in}}$ in decibels is called the return loss, defined as

$$\text{Return Loss} = 10\log_{10}\frac{P_{\text{ref}}}{P_{\text{in}}}. \tag{4.24}$$

When the power is transferred maximally to the EOM crystal at the resonance frequency of the LC circuit, we expect minimal return loss.

We build the LC circuit given in Fig. 4.4 and measure its return loss as a function of

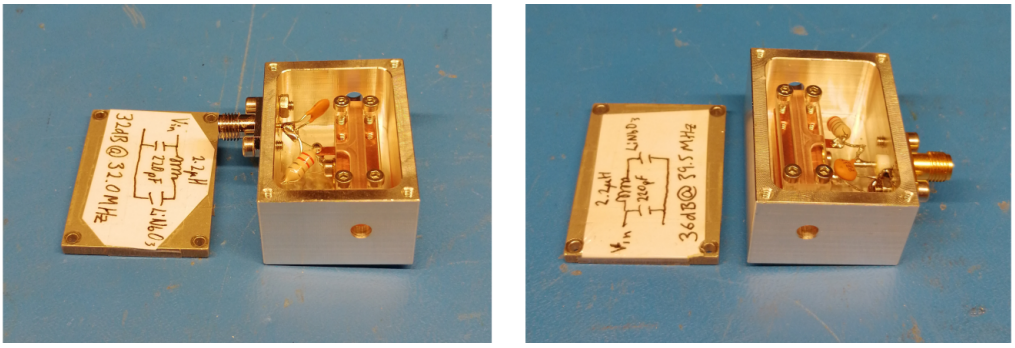

**Figure 4.3** Pictures of the home-built EOMs. These EOMs include the impedance-matching circuit, $LiNbO_3$ crystal and a housing to mount the EOM on an optical setup.

modulation frequency with an impedance analyzer (Times Technology, MFJ-226). We try different capacitors while keeping the inductor in place. We find that the combination of L = 2.2 $\mu$H and C = 220 pF for both EOMs gives us a minimum return loss of -32 dB at a modulation frequency of 32 MHz for one EOM and -36 dB at a modulation frequency of 39.5 MHz for the other EOM. We use the 32 MHz EOM for the plus arm and 39.5 MHz EOM for the minus arm of our crossed cavity.

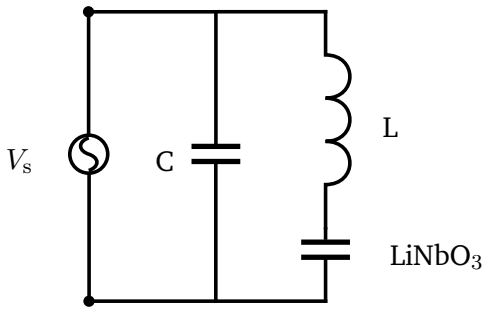


**Figure 4.4** The resonant LC circuit we build to perform impedance matching between the voltage source $V_s$ and the $LiNbO_3$ crystal.

We use programmable voltage-controlled crystal oscillators (SiT3808, SiTime) to produce modulation signals for our EOMs at these frequencies. We program the voltage-controlled crystal oscillators (VCXOs) by using the relevant software (Time Machine) in a computer environment. We integrate the VCXOs into a printed circuit board (PCB) for splitting the signal into two. For more details about the programming procedure and the PCB design, we refer the reader to Refs. [60] and [61]. One signal is sent to the local oscillator port of the mixer to demodulate the error signal and the other one is sent to an amplifier (RF Bay, MPA-10-40) which amplifies the signal and sends it to the LC circuit that contains the EOM crystal. We refer to the former as the mixer port of the PCB and the latter as the amplifier port of the PCB. The PCB that we use also has an LC low-pass filter to suppress the harmonic frequencies of the VCXO, which are at multiples

of the fundamental frequency. In Fig. 4.5, we show the spectrum of the signals with the suppressed harmonics measured with a spectrum analyzer (Anritsu, MS2721B). We observe that higher harmonic frequencies are suppressed by more than 20 dB with the LC low-pass filter.

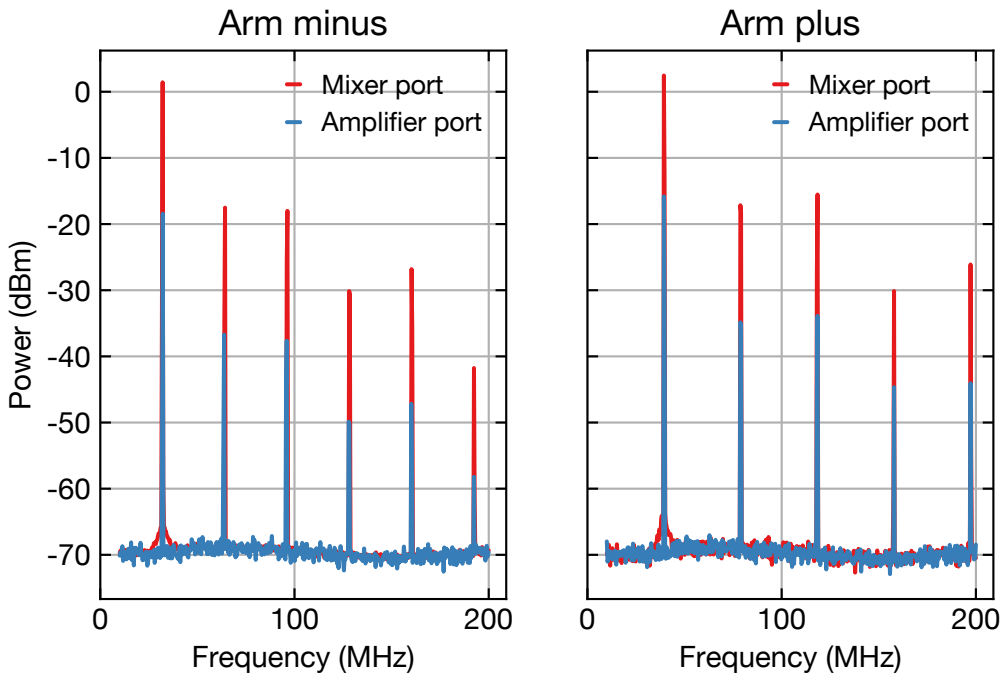


**Figure 4.5** The spectra of the harmonics of the amplifier and the mixer ports. Higher harmonic frequencies are suppressed (>20 dB) with an LC low-pass filter on the PCB.

Lastly, we want to confirm that the modulation signals that our VCXOs produce have a stable frequency and narrow linewidth. Deviations in the modulation frequency may change the return loss of the EOM. This change may also affect the modulation depth. This is a situation we want to avoid since we need the power on the sidebands to stay constant for a stable error signal. We measure the spectrum of the fundamental frequencies (32 MHz & 39.5 MHz) of the amplitude and mixer ports of both VCXOs with a spectrum analyzer (Anritsu, MS2721B) to extract their linewidth. We fit a Gaussian function to the measured data and we find a Gaussian standard deviation of around 0.5 Hz for both EOM drivers. These spectra are shown in Fig. 4.6. These linewidth values cannot be fully resolved with the resolution bandwidth of 1 Hz of our spectrum analyzer. However, this measurement still gives us an upper limit for the linewidth. These upper limit values that we find do not cause a change in the return loss. Furthermore, the VCXOs are specified with a frequency stability of $\pm$ 25 ppm. This corresponds to $\pm$ 800 Hz stability for the plus arm EOM driver and $\pm$ 987 Hz for the minus arm EOM driver. We confirm with our impedance analyzer that these deviations also do not cause a significant change in the

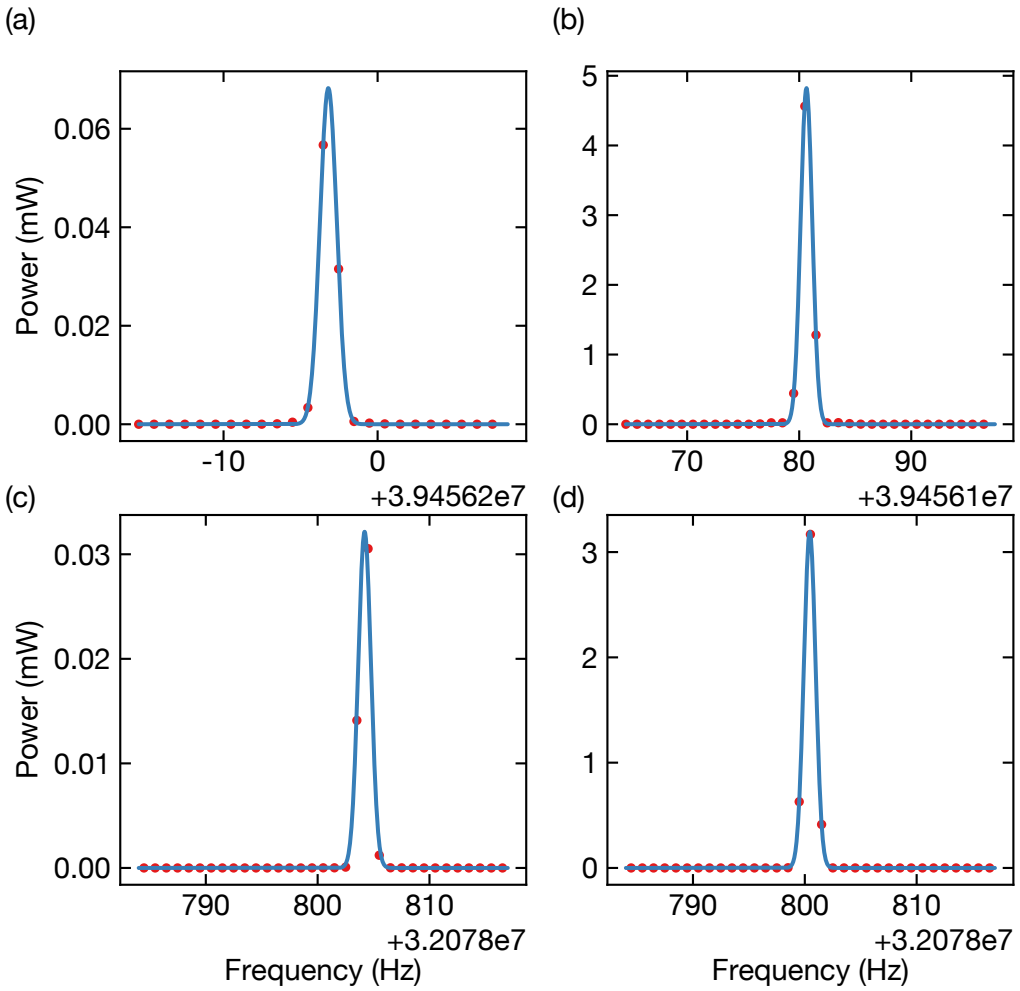


**Figure 4.6** Spectra of the signals produced by the VCXOs. **(a)** The amplifier port of the VCXO we use for the minus arm. We fit a Gaussian to this signal and find a standard deviation of 0.54 Hz. **(b)** The mixer port of the VCXO we use for the minus arm. We fit a Gaussian to this signal and find a standard deviation of 0.52 Hz. **(c)** The amplifier port of the VCXO we use for the plus arm. We fit a Gaussian to this signal and find a standard deviation of 0.57 Hz. **(d)** The mixer port of the VCXO we use for the plus arm. We fit a Gaussian to this signal and find a standard deviation of 0.52 Hz.

return loss. We conclude that the VCXOs that we use provide us with stable signals at the desired frequencies.

### 4.2.4 Laser-induced optical damage

The $LiNbO_3$ crystals that we use in our home-built electro-optic modulators are susceptible to optical damage introduced by a laser beam. The dominating optical damage mechanism in $LiNbO_3$ crystals is the photorefractive damage [62, 63]. As stated before, $LiNbO_3$ is an electro optically active material, i.e., we induce refractive index changes of the crystal when we apply an external electric field. However, the refractive index changes may also be induced by the oscillating electric field of the laser light. Another effect that may take place in our EOM crystals is known as photoconductivity. Photoconductivity is a phenomenon where the electrical conductivity of certain materials increase when they are exposed to light. When the photoconductivity effect is combined with the refractive index change in the crystal induced by the laser beam, photorefractive damage may occur in the crystal. The photorefractive damage may cause permanent spatial refractive index variances inside the crystal. This spatial variance results in a distorted wavefront of the beam travelling through the crystal. Here, we discuss the photorefractive damage we observe in our EOM crystals when they are exposed to the light of our injection lock lasers for a certain amount of time.

After beam shaping the injection lock laser beam of the minus arm with the cylindrical telescope, we use another telescope made of plano-convex lenses to reduce the diameter of the beam so that it can easily propagate through the EOM crystal. We reduce the beam diameter down to 0.8 mm using plano-convex lenses with focal lengths of 75 mm and 35 mm in this telescope. Then, we measure the power of the beam after this telescope as 140 mW with a power meter. We image the beam profile after the telescope using a beam profiler, which we show in Fig. 4.7 (a). We align our beam to go through the EOM crystal and image the beam profile after the EOM as well (see Fig. 4.7 (b)). Then, we place a beam dump after the EOM crystal that absorbs all the light that is transmitted through the crystal, to reduce reflections from any surface that may enhance the intensity of light going through the crystal. After 6 hours of exposure to the laser light with a power of 140 mW and a beam diameter of 0.8 mm, we measure the beam profile after the EOM again and observe that the beam is distorted compared to its initial beam profile (see Fig. 4.7 (c)). We suspect that this beam distortion is a result of the photorefractive damage in our $LiNbO_3$ crystal.

The distorted beam profile limits the maximum fiber coupling efficiency that we can achieve. Due to low fiber coupling efficiencies, a significant part of the optical power will be lost and the required minimum trap depth of $50\mathrm{E}_{\mathrm{rec}}$ may not be reached. To solve this issue, we consider using $LiNbO_3$ crystals that are doped with MgO. The doping process increases the damage threshold intensity, i.e., the minimum intensity that can cause damage, up to $8 \times 10^6$ W/cm$^2$ for continuous light [64]. This threshold intensity is much higher than the intensity of our beam, which is $56$ W/cm$^2$ (from 140 mW & 0.8 mm). Therefore, we aim to replace our $LiNbO_3$ crystals with ones that are doped with MgO in the future to improve our fiber-coupling efficiencies.

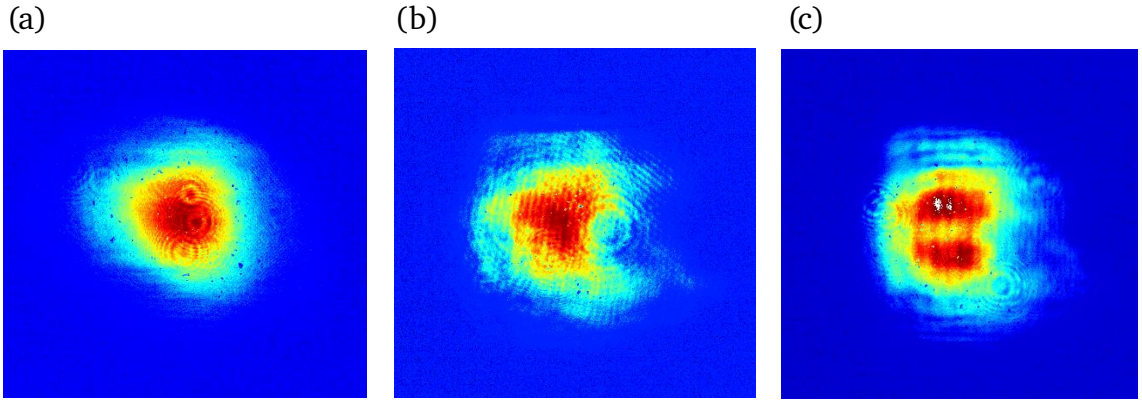


**Figure 4.7** The distortion of the beam profile caused by the photorefractive damage. **(a)** The beam profile of the injection lock laser (minus arm) after going through a cylindrical and a plano-convex telescope. **(b)** The beam profile after passing through the EOM crystal. The beam profile is already distorted due to the optical damage introduced to the crystal during the past measurements. **(c)** The beam profile after exposing the crystal to laser light for 6 hours.

## 4.3 Measurement of the crossed-cavity modes near the tune-out wavelength

In our setup, we can make optical lattices and implement the PDH technique only at the resonance frequencies of our crossed-cavity modes. These cavities have a free spectral range of about 3 GHz, as mentioned in Sec. 2.4.1. We cannot tune the resonance frequencies of the modes of the cavities. Hence, we cannot make a lattice arbitrarily close to the tune-out wavelength. Here, we characterize the resonance frequencies of the cavity modes that are close to the tune-out wavelength. Then, we calculate the non-vanishing ground state lattice depths associated with these frequencies.

| | Resonance frequency (THz) | Detuning (MHz) |
|---|---|---|
| Arm minus | 434.97326 | 1130 |
| | 434.97026 | -1870 |
| Arm plus | 434.97310 | 970 |
| | 434.97010 | -2030 |

**Table 4.1** The measured resonance frequencies of the crossed-cavity modes and their detunings from the tune-out wavelength.

We use the light from our master laser to determine the frequencies of the cavity modes. First, we split our master laser beam using a PBS. Then, we guide both beams into optical fibers. We send one of these beams to our wavelength meter. We tune our master laser's frequency to the tune-out frequency while monitoring it on the wavelength meter. Then,

we send the other beam to the crossed cavity. To align the beam to one of the arms of the crossed cavity, we go through a cavity-alignment procedure similar to the procedure we went through in Sec. 3.2 with the Fabry-Pérot cavity. The details of this procedure and the experimental setup will be discussed in detail in the next Section of this Chapter. After coupling light into the cavity, we monitor the transmission through the cavity with a photodetector. Then, we vary the frequency of our master laser manually by changing the piezo voltage. We observe the maximal voltage of the photodetector when the frequency of the laser matches the frequency of a cavity mode. Then, we read the frequency of our master laser on the wavelength meter, which tells us the frequency of the cavity mode. We go through this procedure for both arms of the cavity and find the cavity modes with frequencies closest to the tune-out wavelength. Note that the tune-out wavelength corresponds to 434.97213 THz in units of frequency in vacuum. We present the frequencies of the cavity modes in Tab. 4.1. In Fig. 4.8, we illustrate the cavity modes centered at these frequencies by plotting Lorentzian functions numerically. We also notice that the modes of the plus arm and the minus arm differ by 160 MHz in frequency. Therefore, we need to use acousto-optic modulators (AOM) to shift the frequency of our lasers accordingly. We discuss this method in detail in the next Section of this Chapter.

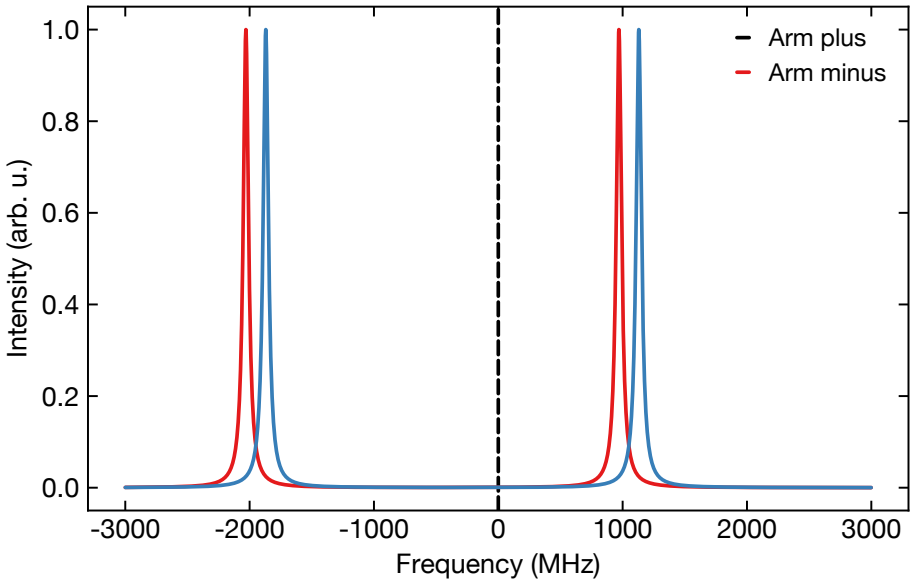


**Figure 4.8** The modes of the crossed cavity around the tune-out wavelength, numerically represented by Lorentzian curves. The dashed line represents the tune-out wavelength.

Due to the fact that the lattice inside the cavity is slightly detuned from the tune-out wavelength, the ground state potential does not vanish completely. In our experiments, we want the attractive potential of the non-vanishing ground state lattice to form at the

intensity minimum, similar to the excited state. Otherwise, the overlap between wavefunctions of the trapped and the untrapped states will be poor. Trapping at the intensity minimum only occurs for a negative $^1S_0$ polarizability, i.e., for wavelengths higher than the tune-out wavelength (see Fig. 2.2). Therefore, we prefer using the cavity modes that are red detuned (-1870 MHz and -2030 MHz). With the measured detuning values of the cavity modes from the tune-out wavelength, we use Eqn. (2.17) and calculate the minimum achievable lattice depths of $0.29E_{rec}$ and $0.31E_{rec}$ for the minus and the plus arm, respectively. In this calculation, we assume an input power of $26\ mW$ before each arm.

| | Resonance frequency (THz) | Detuning (MHz) |
|---|---|---|
| Arm minus | 434.83197 | 2850 |
| | 434.82897 | -150 |
| | 434.82597 | -3150 |
| Arm plus | 434.83167 | 2550 |
| | 434.82866 | -460 |
| | 434.82565 | -3470 |

**Table 4.2** The measured resonance frequencies of the crossed-cavity modes and their detunings from the $^1S_0 - {}^3P_1$ transition frequency.

As a last remark, we measure other consecutive modes of the cavity near a frequency of 434.82912 THz with our method and present them in Tab. 4.2. We are interested in this frequency because it is the frequency of the $^1S_0 - {}^3P_1$ transition of strontium. Since this transition frequency is close to the tune-out wavelength, the atoms in the tune-out lattice may suffer from photon scattering. We investigate this subject further in the next Chapter of this thesis.

## 4.4 PDH technique in a crossed cavity with intensity stabilization

Having obtained the resonant frequencies of the crossed cavity that we can work with, we implement the PDH technique to stabilize the laser frequency to these resonant frequencies. Additionally, we use another control loop to stabilize the intensity of the laser in front of the cavity. We illustrate the finalized setup in Fig. 4.9. Our setup consists of four parts: the master laser setup, two injection lock setups and the crossed-cavity setup. We start by describing the master laser setup. First, we split the beam from the master laser into two with a PBS cube. One beam path is further split into two for monitoring the wavelength of light on a wavelength meter and for pre-stabilization of the laser frequency with a frequency comb, which we explain in detail in Sec. 4.5. The other beam path is also split into two using a PBS cube to seed the slave lasers.

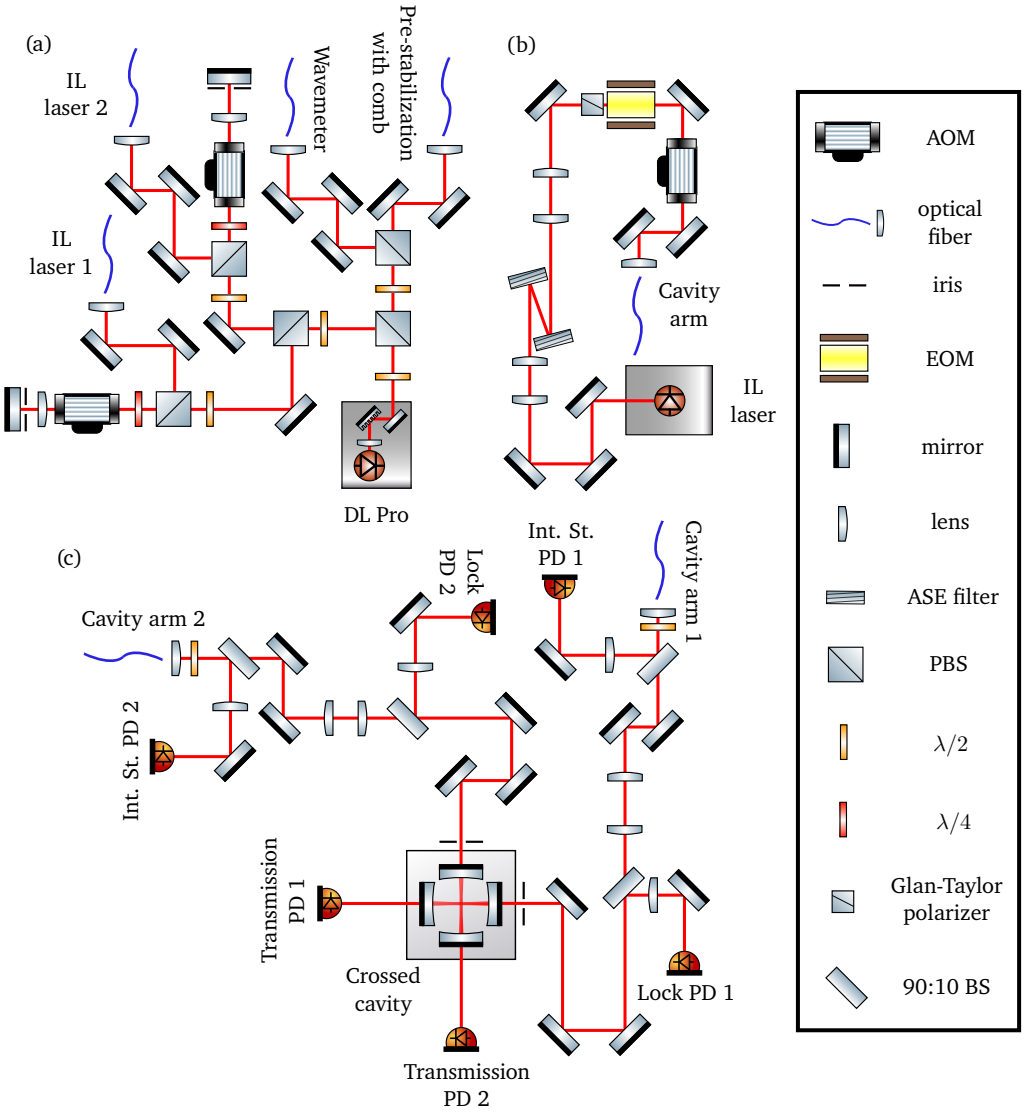


**Figure 4.9** The illustration of the master laser, injection lock, and crossed-cavity setups. **(a)** The master laser setup that consists of the master laser and two AOMs in double-pass configurations for the PDH technique **(b)** Injection lock setup. The light produced by the injection lock lasers are modulated with an EOM for sideband generation and an AOM for intensity stabilization. **(c)** The beam setup at the crossed cavity, where lattices are created.

We use two acousto-optic modulators with frequencies of 200 MHz & 270 MHz in double-pass configurations to shift the frequency of our laser beams since the cavity modes of the minus arm and the plus arm are 160 MHz apart from each other, as discussed in the previous Chapter. Each of these acousto-optic modulators (AOMs) is placed before the two fibers that go to the slave lasers for seeding. We use voltage-controlled

oscillators (VCOs) to operate these AOMs and to modulate their frequency for the PDH lock. We maximize the intensities in the -1. diffraction orders of these AOMs when they are operating at frequencies of 193 MHz and 275 MHz. This diffraction order gives us -193 MHz and -275 MHz shifts of the laser frequency in a single pass. Since we use a double-pass configuration, these frequency shifts are doubled. When we modulate these frequencies for the PDH lock, the intensity of this diffraction order will change. Furthermore, the angle of propagation of the diffraction order will also change. These two effects reduce the intensity of the seed light going to the injection lock modules and may result in the slave laser diodes unlocking from the master laser due to insufficient seed power. The former effect will directly reduce the light intensity, while the latter effect will reduce the fiber coupling efficiency. To understand how much this affects us, we perform a measurement. We scan the frequency of the VCOs by $\pm$25 MHz using a function generator (Keysight, 33220A). Then, we measure the intensity of the diffraction order we are interested in with a powermeter (Thorlabs, PM100D) before and after the fibers that we guide our seed light in. Then, we stop the frequency scan, lock the slave laser diodes to the master laser at VCO frequencies of 193 MHz and 275 MHz, and tune the frequency of the VCO manually. When the slave laser diodes get unlocked from the master laser due to insufficient intensity, we note the frequency of the VCO. We provide the scan measurements in Fig. 4.10. Here, the dashed lines represent the frequencies where slave lasers unlock from the master laser. From this figure, we observe that the lasers can stay locked over a bandwidth of 40 MHz (arm minus) and 30 MHz (arm plus).

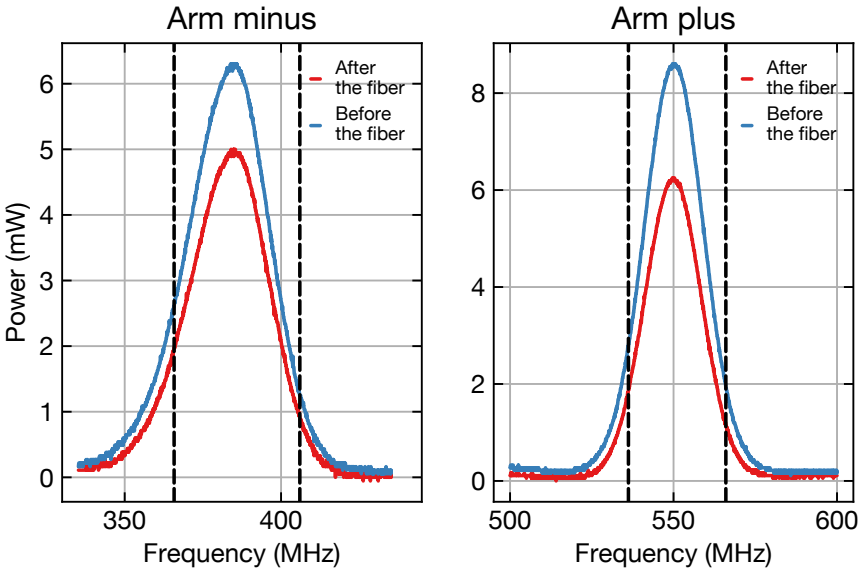


**Figure 4.10** The power of the -1. diffraction order of the double-pass AOMs as a function of VCO frequency before and after coupling into a fiber. Vertical dashed lines correspond to the VCO frequencies where the injection lock lasers fall out of lock from the master laser.

In each injection lock setup, we lock the slave laser diodes by tuning the current. Then, we use a cylindrical telescope to collimate the uncollimated axis of the beam, as we discussed in Sec. 3.3. Then, we use two optical components known as ASE filters. We explain the functionality of these filters in the next Chapter of this thesis. For now, we may simply regard them as reflective optical components in the beam path. After the filters, we use a plano-convex telescope to reduce the size of the Gaussian beam so that it can go through the EOM crystal. We do not supply the modulation signal to the EOMs yet. After the EOM, we have an AOM operating at a fixed frequency of 80 MHz. We use this AOM for the intensity stabilization of the laser beam passing through it. For this, we monitor the laser intensity with a photodetector on the crossed-cavity setup and stabilize the laser intensity by modulating the amplitude of the AOM radio-frequency (RF) signal using a PID circuit. After this AOM, the beam is coupled into a fiber which sends it to the crossed-cavity setup.

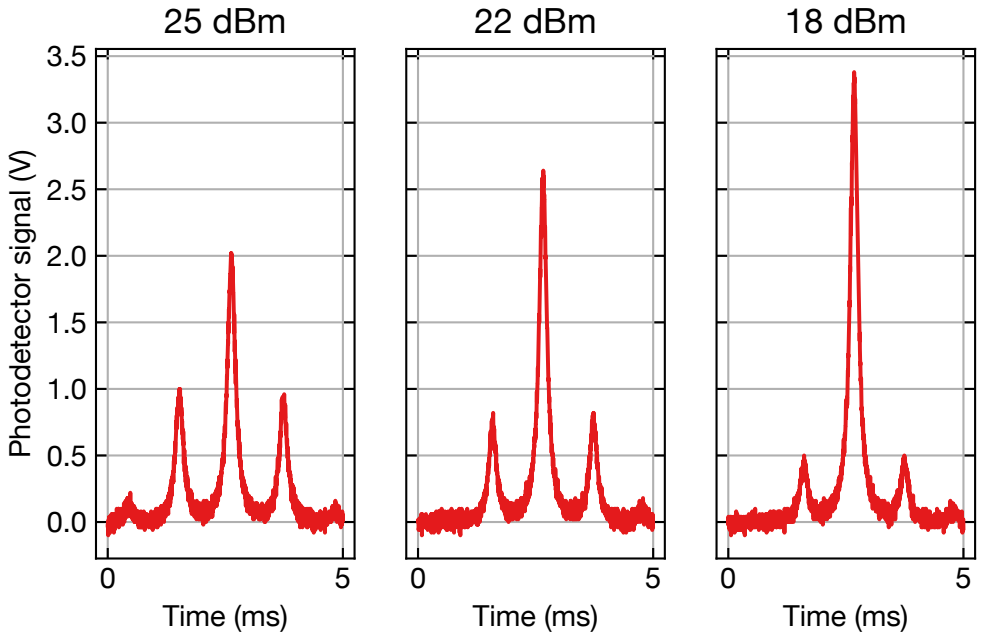


**Figure 4.11** Transmission signal of the crossed cavity for different driving powers of the EOM (plus arm). We use a driving power of 22 dBm to generate the error signal for both arms of the crossed cavity.

In the crossed-cavity setup, we collimate the beam from the fiber first. Then, we send a small fraction of this light to the photodetector which we use for intensity stabilization, as mentioned above. We use a telescope in front of the cavity to match the spatial mode of the beam to the mode of the cavity. First, we scan the frequency of the master laser periodically by scanning the piezo voltage. The frequency scan is slow enough (<50 Hz) to be followed by the injection lock modules. If the frequency scan is faster, the injection

lock lasers get unlocked. Then, we align the beam to the cavity roughly and monitor the transmission through the cavity with a photodiode. We minimize the higher order modes we see in the transmission spectrum by using two mirrors and mode matching with the lens in front of the cavity. Then, we connect the amplified VCXO signals to the home-built EOMs and monitor the sidebands on the transmission signal of the cavity. We try several different power attenuators to attenuate the output power of the VCXOs. In this manner, we can adjust the modulation depth and control how much power is in the sidebands. In Fig. 4.11, we show how different power levels of the amplified VCXO signal affect the sideband-to-carrier ratio. We use the attenuator that gives us a sideband-to-carrier ratio of 40 %, which means that 40 % of the optical power is in the sidebands.

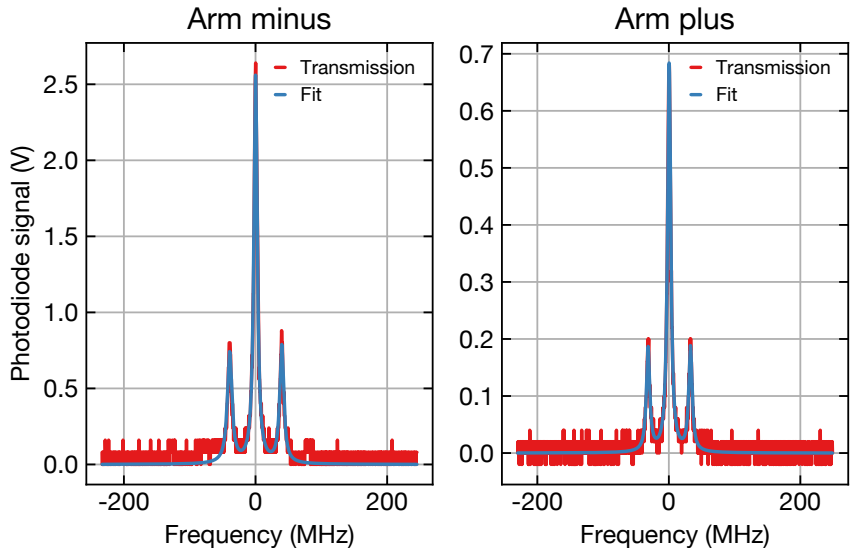


**Figure 4.12** Transmission spectrum of the crossed cavity with an EOM driving power of 22 dBm for both cavity arms. Three Lorentzian functions are fit to the transmission signal for obtaining the frequency axes in these plots.

We estimate the linewidths of the crossed cavity from the transmission spectrum in Fig. 4.12. To do this, we fit three Lorentzian functions to the transmission signal and calculate the carrier-sideband peak separation in terms of the time axis of the transmission signal. Since we know that this corresponds to our modulation frequency, we can convert the time axis to a frequency axis. Then, we extract the full width half at maximum (FWHM) of the cavity mode in terms of frequency from the Lorentzian fit. We find FWHMs of 5.42(8) MHz for the minus arm and 5.85(5) MHz for the plus arm. We see that these values mostly agree with the linewidth values we presented in Tab. 2.1 of Sec. 2.4.1.

We use a beam sampler with a sampling ratio of 90:10 in front of the cavity to send the back-reflected beam from the cavity to a photodetector for the PDH lock. Normally, a

quarter-wave plate is used for this purpose in a PDH lock. However, since we want to be able to control the linear polarization of the lattice, we use the beam sampler. Then, we go through the standard procedure of generating the error signal, as mentioned in Sec. 4.2.2. We optimize the error signals for both arms and show them in Fig. 4.13. Then, we feed the error signals to a PID circuit whose output modulates the VCO frequency of the AOMs in the master laser setup. This modulation locks the laser to the crossed-cavity resonances. Therefore, we have an active stabilization scheme for the state-dependent lattice.

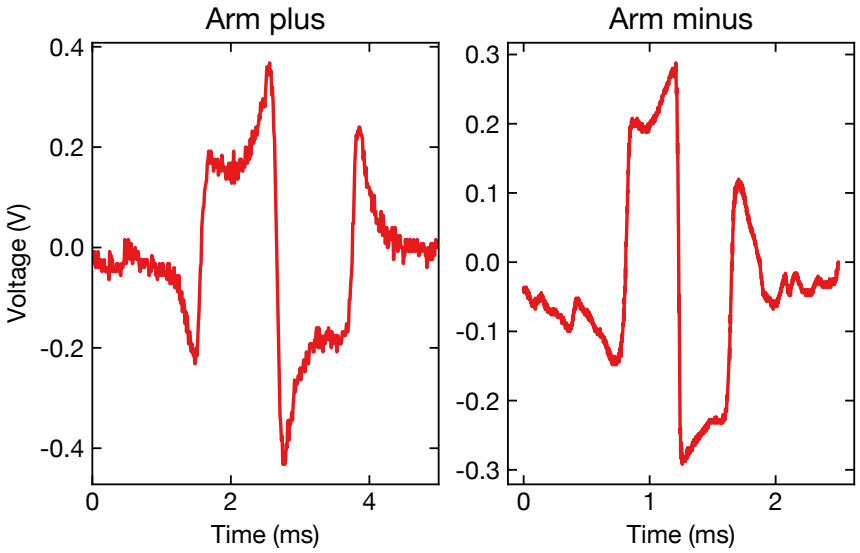


**Figure 4.13** The optimized error signals used for the PDH technique.

Since there are optical losses in our experimental setup, we need to confirm that we have enough power to make lattices at a trap depth of $50\mathrm{E_{rec}}$. We measure a power of $\sim 50\ \mathrm{mW}$ before the cavity arms. Note that this is slightly different for each arm due to differing optical losses in the injection lock setups. Since 40 % of the power is in the sidebands, we estimate that a power of $\sim 30\ \mathrm{mW}$ will enter each cavity, which satisfies the trap depth condition we have.

## 4.5 Pre-stabilization with frequency comb

Although the master laser emits light with a precise frequency and a narrow linewidth for our tune-out lattices, we observe long-term changes in its frequency. When the master laser drifts too far from the cavity resonance, the operating frequencies of the AOMs have to change to stay resonant with the cavity mode. This causes the diffraction efficiencies of the AOMs to decrease, leading to the slave lasers unlocking from the master laser (see Fig. 4.10). Therefore, in addition to the lattice laser stabilization scheme we introduced in

the previous Chapter, we devise another stabilization scheme to counter these long-term frequency drifts of the master laser. We lock our laser to a frequency comb to achieve this. A frequency comb is a laser source with a stable frequency spectrum that has a series of discrete, equally spaced frequency lines. Because of this feature, it may be used as an absolute optical frequency reference. We refer the reader to Ref. [65] for more details about the operating principle of frequency combs. Here, we discuss the method we use to lock the master laser to our commercially available frequency comb (Menlo Systems, FC1500-250-WG) which has a 250 MHz mode spacing.

First, we send a portion of our master laser beam from the master laser setup with a PBS (see Fig. 4.9) to our frequency comb setup using an optical fiber. Then, we overlap the master laser beam with the frequency comb beam using a non-polarizing beam splitter (NPBS). We send the overlapped beams to a reflection grating (Thorlabs, GR13-1205). Since the frequency comb beam has multiple frequency components in its spectrum, it gets dispersed by the grating. The frequency components that are near the master laser frequency stay spatially overlapped with the master laser beam since their diffraction angles are almost the same as the master laser. Then, we send the overlapped beam to a photodetector that measures the beat note between the frequency comb and the master laser. We send the beat note from the photodetector to a power splitter. We send one of the output signals of the power splitter to a frequency counter. For the other output port of the splitter, we use a low-pass filter (Mini-Circuits, SLP-100+) with a cut-off frequency of 98 MHz to isolate a single beat note between the master laser and the closest frequency comb mode. Then, we amplify the signal with an amplifier (RF Bay, MPA-10-40). To stabilize the master laser, it is sufficient to stabilize the frequency of the beat note. We use a phase-locked loop to achieve this. Therefore, we introduce the concept of a phase-locked loop (PLL) first.

A PLL is a servo loop with a phase detector which detects the relative phase between a reference signal and an input signal. The phase detector generates an error signal to lock the frequency of the input signal to the reference signal. In our case, the input signal is the amplified beat note and we use a function generator (Keysight, 33220A) to produce a reference signal. The amplified beat note is sent to the input port of a PLL circuit. The frequency of this signal is scaled down by 10 with a frequency divider inside the PLL circuit. We also provide this circuit with a reference signal at 6.4 MHz using the function generator. An error signal is generated by the PLL and passed through a low-pass filter with a cut-off frequency of 4 kHz. We send the error signal to a PI circuit. We connect the output of the PI circuit to the “fine in” input port of the master laser controller. Then, we define this input port as the piezo voltage input port using the digital interface of the laser controller. Hence, we stabilize the frequency of the master laser by modulating its piezo voltage.

## 4.6 Long term intensity stability

When we integrate our tune-out lattices in our experimental cycles, we expect the lattice to be stable in the long term, i.e., we expect stable injection locking of the slave laser diodes to the master laser, stable frequency locking of the master laser to the frequency comb, and stable PDH locking of the injection lock lasers to the crossed-cavity. To test this, we perform a measurement. We turn on the lasers, stabilize the master laser frequency with the frequency comb, stabilize the intensity in front of the cavities, and lock the laser frequencies to the resonant frequencies of the cavities. This way, we generate an optical lattice in the crossed cavity. We measure the power of the light transmitted through the cavity for ∼8 h. Furthermore, we also measure the frequency of the beat note between the frequency comb and the master laser with the frequency counter using a software that runs on the operating system of the frequency comb. We present the long-term measurement of the power of light transmitted through both arms of the cavity in Fig. 4.14 (a). We also present the beat note frequency over the course of this measurement in Fig. 4.14 (b).

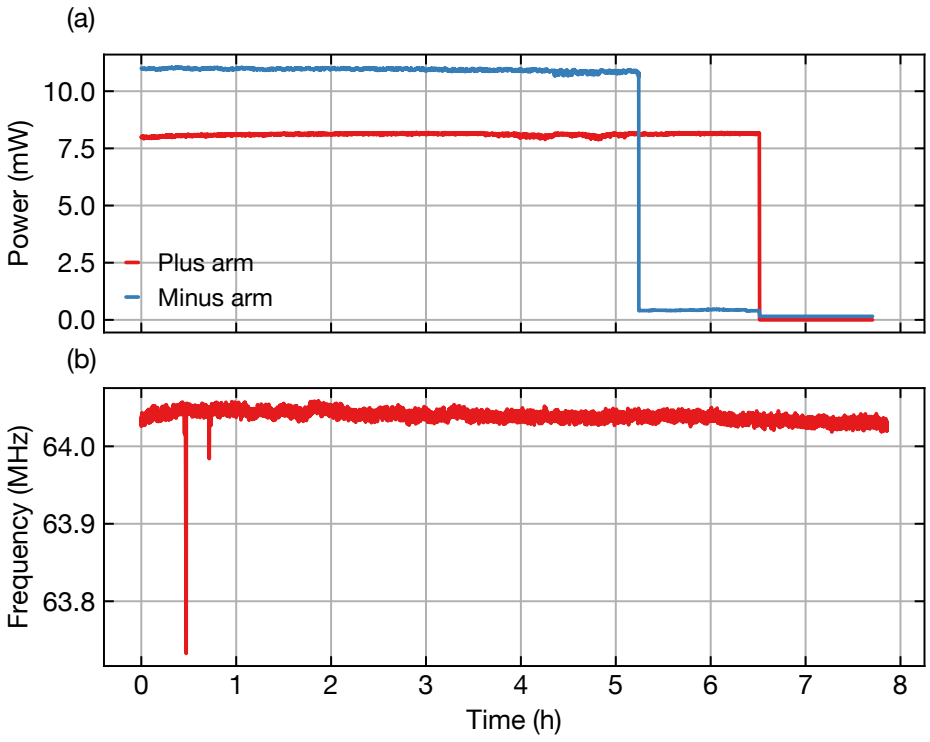


**Figure 4.14** **(a)** A long-term measurement of the transmitted powers through the crossed cavity. We observe an abrupt decrease in the transmitted powers a few hours after the beginning of the measurement. **(b)** The beat note frequency over the course of the measurement.

Although the beat note frequency changes abruptly by ∼300 kHz during the first hour of the measurement, this does not influence the PDH locking status since our AOMs can correct this frequency shift. Furthermore, the transmission powers stay stable for ∼5 h. After ∼5 h, we observe a sharp decrease in the transmission power of the minus arm, followed by the plus arm ∼1 h later. We realized that the injection locking between the slave lasers and the master laser was lost at these times. We were able to lock them again by changing the operating current of the slave laser diodes. We believe that this unlocking is a result of a slight optical misalignment of the seed beam due to pressure fluctuations in the laboratory. In the older versions of these modules in our experiment, a wedged window is glued to the opening of the module box where the beam exits. This window can make the box air tight and it can prevent the fluctuations in the room pressure influence the optical alignment inside the box. Therefore, we plan to use this component in our setup as well in the future. Another strategy is to implement an automatic relocking scheme that ramps the current to lock the injection lock lasers again. For now, a stability period of 5 h is sufficient for us to start conducting experiments with the tune-out lattice.

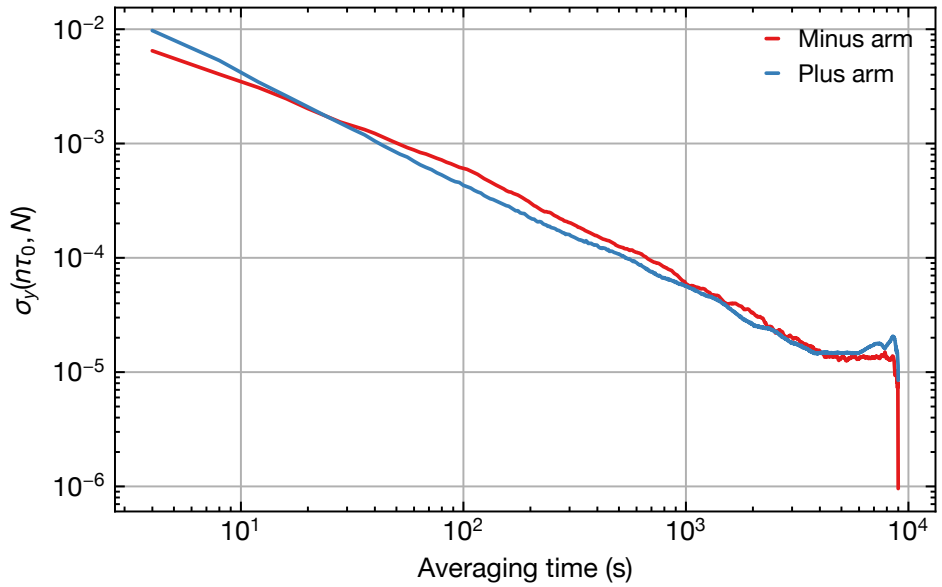


**Figure 4.15** The overlapping Allan deviation calculations of the powers transmitted through both arms of the cavity.

As a next step, we want to estimate the stability of the transmitted powers by calculating their Allan deviation. Allan deviation is a statistical analysis tool that lets us analyze the noise in a signal. By definition, the overlapping Allan deviation $\sigma_y$ is given by [66]

$$\sigma_y^2(n\tau_0, N) = \frac{1}{2n^2\tau_0^2(N-2n)} \sum_{i=0}^{N-2n-1} (x_{i+2n} - 2x_{i+n} + x_i)^2, \tag{4.25}$$

where $\tau_0$ is the sampling period, $n$ is an integer number that estimates the averaging time with $\tau = n\tau_0$, $N$ is the number of data points and $x_i$ is the $i^{\text{th}}$ element in the signal. In general, a low Allan deviation is an indication of good stability in a measured signal over the averaging time $\tau$. Our main motivation for calculating the Allan deviation is to compare the stability of the minus arm transmission power and the plus arm transmission power. We present our overlapping Allan deviation calculations for both arms in Fig. 4.15 as a function of averaging time. Note that we choose a sampling period of $\tau_0 = 4$ s. As we see from this figure, we have similar stabilities on both arms, confirming that there are no systematic differences between the two arms.

## 4.7 Relative intensity noise

So far, we discussed the stabilization techniques we use for the state-dependent lattice in this Chapter. In this Section, we proceed with characterizing the intensity noise of the lattice field when we employ these techniques and we calculate the resulting parametric heating rate.

Relative intensity noise (RIN) is a way of quantifying a laser's optical power level instability. It is defined as the ratio of power noise to the average power. Time-dependent power of the laser can be written as

$$P(t) = \bar{P} + \delta P(t), \tag{4.26}$$

where $\bar{P}$ is the average power and $\delta P(t)$ is the deviation in the power level. A convenient way to define RIN is the one-sided spectral density $S(\omega)$ given in Eqn. (4.5). Since the power of the laser is proportional to the intensity, we can use $\delta P(t)/\bar{P}$ instead of the fractional intensity noise $\epsilon(t)$ in this equation. This is a useful replacement since we can measure the power deviations of the laser with a photodetector.

Our goal is to measure RIN experimentally in our lattice setup. First, we generate an optical lattice in the crossed cavity as mentioned in the previous Section. We use a photodetector to measure the RIN at different points in the beam path. We connect the photodetector to an intensity noise analyzer (Thorlabs, PNA1) that measures the RIN. The intensity noise analyzer is essentially a spectrum analyzer that displays the power spectrum $S(\omega)$ when we provide it with the power $P(t)$. Furthermore, we measure the photodetector noise floor by blocking the beam to make sure that the measurement is not limited by the photodetector noise level. In this case, we do not normalize the noise with the average power $\bar{P}$ because the beam does not hit the photodetector and the average power is zero, which leads to dividing by zero. Instead, the intensity noise analyzer calculates the numerator of the one-sided spectral density. When we want to compare a RIN measurement with this photodetector noise, we normalize the photodetector noise with the average power of the signal we are comparing it with. Note that the normalization should be performed in linear units, instead of logarithmic ones.

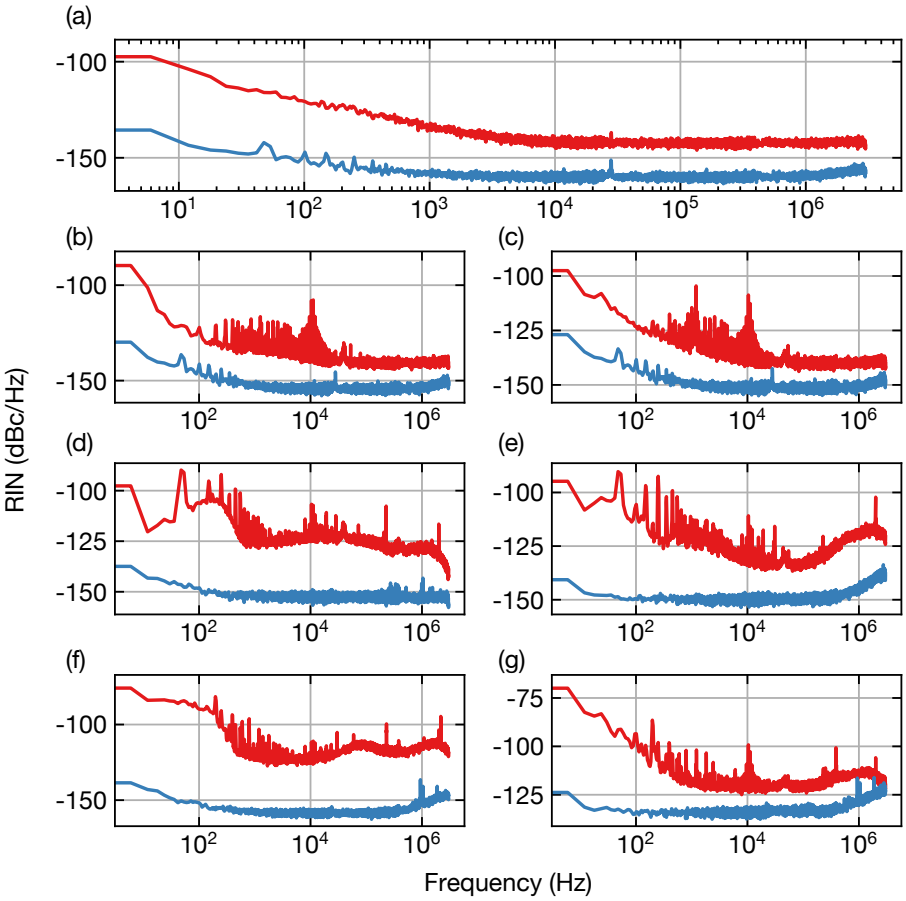


**Figure 4.16** The RIN measurements conducted at different points in the experimental setup. The red curves show the RIN measurements of the laser beam while the blue curves represent the floor noise of the photodetector that is used in the corresponding measurement. The unit of RIN we use here is dBc/Hz. The measurement points are **(a)** after the master laser, **(b)** & **(c)** after the minus and the plus arm injection lock lasers, **(d)** & **(e)** in front of the crossed-cavity with the intensity stabilization photodetectors of the minus and the plus arm, **(f)** & **(g)** after the crossed cavity with the transmission photodetectors of the minus and the plus arm.

We measure RIN for each cavity arm at four points: after the master laser, after the monitoring fiber of the injection lock module which sends light to the Fabry-Pérot cavity, in front of the crossed cavity with the intensity stabilization photodetector, and after the crossed cavity with the transmission photodetector. We display these measurements in Fig. 4.16.

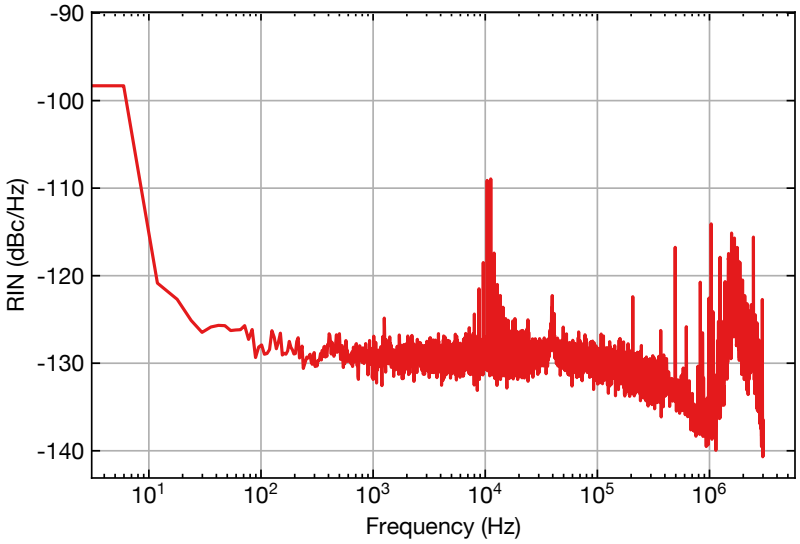


**Figure 4.17** The noise measurement of the current monitor port of the laser controller, which converts the operating current of the laser diode to a voltage. We performed this measurement with the intensity noise analyzer.

We observe that several peaks appear in the RIN after the injection lock lasers. We confirm that these peaks are coming from the injection lock laser controllers (Thorlabs, ITC4001) by attaching the intensity noise analyzer to the current-monitoring port of the laser controller. This port converts the operating current of the laser controller to a voltage for monitoring purposes. Therefore, we can treat this measurement as the noise spectrum of the operating current. We present this measurement in Fig. 4.17. We believe that these peaks are the Fourier components of certain electronic components inside the laser controller because we observe several peaks separated by 400 Hz. This situation might enhance the parametric heating rate. To suppress these peaks, we build the LC low-pass circuit in Fig. 4.18. Our aim is to pass the current supplied to the slave laser diode through this low-pass circuit.

We use an inductor with $L = 120\ \mu$H and a capacitor with $C = 220\ \mu$F to build the low-pass circuit. These values give us a cut-off frequency of 980 Hz. We choose an inductor that has minimal internal DC resistance to prevent the increase of the voltage applied on the slave laser diode by the laser controller, due to Ohm's law. We measure the internal resistance of our inductor as 0.9 $\Omega$ using a multimeter. Then, we connect our low-pass filter between the slave laser diode of the minus arm and the laser controller. We do not observe a significant rise in the voltage applied on the laser diode. We lock the slave laser to the master laser, measure the RIN of the injection lock module with its monitoring fiber and compare this measurement with the RIN that we measure without a filter. We present these measurements in Fig. 4.19. With this method, we are able to suppress the peaks

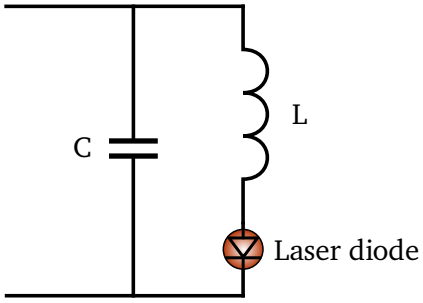


**Figure 4.18** The LC low-pass filter design that is used to suppress the noise of the operating current.

down to the floor-noise level of the slave laser. However, we realize that the use of the LC filter makes the RIN level of the laser unstable. We see up and down deviations in the RIN during the operation of slave lasers. We believe that this is due to external effects such as the temperature fluctuations of the low-pass filter, which affects the internal resistance of the inductor. Therefore, we do not implement the low-pass filters in the experiment at this stage. We aim to solve this issue in the future by using high-quality and low-resistance electronic components and by integrating them into a PCB.

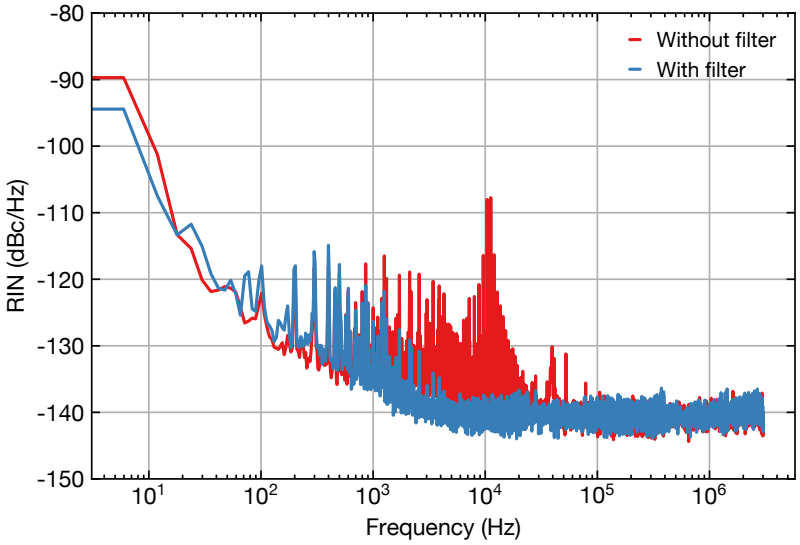


**Figure 4.19** The RIN measurement of the injection lock laser with and without the low-pass filter with a cut-off frequency of 1 kHz.

### 4.7.1 Heating rate

To calculate the parametric heating rate, we use the RIN of the transmission through the cavity, since this measurement already includes the frequency-to-amplitude noise conversion. At twice the trapping frequency, the RIN of the transmission gives us $S(2\nu_{\mathrm{tr}})$, which allows us to calculate $\Gamma_\epsilon$ from Eqn. (4.4). At the proposed lattice depth of $50\mathrm{E}_{\mathrm{rec}}$, we have a trapping frequency of $\nu_{\mathrm{tr}} \approx 68\ \mathrm{kHz}$. We look at the value of the transmission RIN at $2\nu_{\mathrm{tr}}$ and find $-115\ \mathrm{dBc/Hz}$ for the minus arm and $-120\ \mathrm{dBc/Hz}$ for the plus arm. With these values, we calculate heating rate constants of $\Gamma_\epsilon = 0.14\ \mathrm{s}^{-1}$ for the minus arm and $\Gamma_\epsilon = 0.04\ \mathrm{s}^{-1}$ for the plus arm. These values are sufficiently low and comparable to the value of $\Gamma_\epsilon = 0.1\ \mathrm{s}^{-1}$ that was proposed in an earlier work of our team [43].

## Conclusion

We presented a laser stabilization scheme that helps us make stable tune-out lattices in the crossed cavity. This scheme involves the PDH locking of the lasers to the resonances of the crossed cavity, a control loop to stabilize the laser intensity and the pre-stabilization of the master laser with a frequency comb. We measured the long-term stability of the system. We observed a stability period of $\sim$5 h, after which the slave lasers get unlocked from the master laser. We argued that we can improve this stability period by making the injection lock modules air tight using a wedged window at the laser beam output or by implementing an automatic relocking scheme. We measured the RIN at different points of the setup and we observed several peaks in our measurement. We demonstrated that these peaks can be suppressed by filtering the current supplied to the slave laser diode with a low-pass filter. Finally, we estimated the parametric heating rate constant $\Gamma_\epsilon$ using the measured RIN value of the transmission signal at a frequency of $2\nu_{\mathrm{tr}}$. From this estimation, we conclude that the presented stabilization scheme can help us suppress the parametric heating in the lattice sufficiently.

# Chapter 5

# Amplified spontaneous emission filtering

ALTHOUGH the rich electronic structure of strontium provides us with multiple benefits, some of its aspects make it more challenging to work with tune-out lattices. One of these challenges is caused by the proximity of the tune-out wavelength (689.222 nm) to the wavelength of the $^1\mathrm{S}_0 - {}^3\mathrm{P}_1$ transition (689.449 nm). This proximity results in an uncontrolled heating mechanism due to the scattering of lattice photons by the atoms [43, 67]. Furthermore, this scattering may get enhanced due to a phenomenon known as amplified spontaneous emission (ASE). In this Chapter, we discuss how ASE is generated in the gain medium of a laser and how it enhances the scattering. Then, we measure the ASE generated by our lasers and we discuss how we suppress it. Lastly, we characterize how good this suppression is by calculating the scattering rate in the lattice.

## 5.1 Amplified spontaneous emission

We begin by discussing the concept of spontaneous emission since it plays a role in the ASE phenomenon. We consider a two-level atom with energy levels $E_\mathrm{g}$ and $E_\mathrm{e}$ for the ground and the excited state, respectively. When the atom is in the excited state, it can spontaneously return to its ground state, emitting a photon in the process. This process is called spontaneous emission. The emitted photon has a frequency of

$$\nu = \frac{E_\mathrm{e} - E_\mathrm{g}}{h} \tag{5.1}$$

where $h$ is the Planck's constant. If an ensemble of atoms is present instead of a single atom, a collective spontaneous emission of these atoms can be observed. However, the process of spontaneous emission occurs with a random polarization, direction and optical phase. Therefore, the collective spontaneous emission of the ensemble of atoms is an incoherent emission. Spontaneous emission also takes part in the coherent amplification of light in a laser. We refer the reader to Ref. [68] for further details about this process.

While spontaneous emission can occur in any direction in the gain medium of a laser, it gets optically amplified in the propagation direction of the laser light due to a higher gain in this direction. This phenomenon is known as amplified spontaneous emission [69–71]. ASE results in the emission of an incoherent background radiation that has a much broader spectrum than the linewidth of the laser. Therefore, ASE is an unwanted effect in applications where coherent light sources are needed. Various laser sources

may contain ASE in their spectra, including laser diodes. Since we use laser diodes in our setup, we are interested in determining the potential influences of their ASE on the tune-out lattices.

### 5.1.1 Scattering

In this part, we discuss the main limitation we encounter due to ASE, which is the scattering of photons in the lattice by strontium atoms. The term scattering stands for a cluster of phenomena in physics. To understand the concept of scattering in the context of atom-light interactions, we consider a two-level atom interacting with an off-resonant light. In Ref. [72], the time evolution of this system is described by the optical Bloch equations,

$$\frac{d\rho_{\mathrm{gg}}}{dt} = +\Gamma\rho_{\mathrm{ee}} + \frac{i}{2}(\Omega^*\tilde{\rho}_{\mathrm{eg}} - \Omega\tilde{\rho}_{\mathrm{ge}}) \tag{5.2}$$

$$\frac{d\rho_{\mathrm{ee}}}{dt} = -\Gamma\rho_{\mathrm{ee}} + \frac{i}{2}(\Omega\tilde{\rho}_{\mathrm{ge}} - \Omega^*\tilde{\rho}_{\mathrm{eg}}) \tag{5.3}$$

$$\frac{d\tilde{\rho}_{\mathrm{ge}}}{dt} = -(\frac{\Gamma}{2} + i\Delta)\tilde{\rho}_{\mathrm{ge}} + \frac{i}{2}\Omega^*(\rho_{\mathrm{ee}} - \rho_{\mathrm{gg}}) \tag{5.4}$$

$$\frac{d\tilde{\rho}_{\mathrm{ge}}}{dt} = -(\frac{\Gamma}{2} - i\Delta)\tilde{\rho}_{\mathrm{eg}} + \frac{i}{2}\Omega(\rho_{\mathrm{gg}} - \rho_{\mathrm{ee}}) \tag{5.5}$$

where $\rho_{ij}$ are the matrix elements of the density matrix describing the two-level atom, $\Gamma = 2\pi\gamma$ is the linewidth of the atomic transition, $\Omega$ is the Rabi frequency and $\Delta$ is the detuning of light from the transition frequency. These equations have a steady-state solution, i.e., when the decay rate of the excited state population is equal to the rate of absorption. When the steady state is reached, the scattering rate is defined as

$$\Gamma_{\mathrm{sc}} \equiv \Gamma\rho_{\mathrm{ee}} = \frac{\Gamma}{2}\frac{s_0}{1 + s_0 + (\frac{2\Delta}{\Gamma})^2}. \tag{5.6}$$

Here, the on-resonance saturation parameter $s_0$ is given by

$$s_0 \equiv 2|\Omega|^2/\Gamma = I/I_{\mathrm{s}} \tag{5.7}$$

where $I$ is the intensity of light and

$$I_{\mathrm{s}} \equiv \pi hc/3\lambda^3\tau \tag{5.8}$$

where $c$ is the speed of light, $\lambda$ is the wavelength of light and $\tau$ is the lifetime of the excited state. An important detail in Eqn. (5.6) is that the value of $\Gamma_{\mathrm{sc}}$ saturates to $\Gamma/2$ for $s_0 \gg 1$. Furthermore, the absorption spectrum of the atomic transition broadens at high intensities due to the detuning dependence of Eqn. (5.6). This phenomenon is known as power broadening. The broadened linewidth of the absorption spectrum is given by

$$\Gamma' = \Gamma\sqrt{1+s_0} \tag{5.9}$$

In the case of our state-dependent lattices, ASE light that is produced by our lasers near a wavelength of 689.449 nm can induce the $^1\mathrm{S}_0 - {}^3\mathrm{P}_1$ transition of strontium. When the atoms interact with light near this wavelength, they scatter a photon by absorbing its energy. The scattering process introduces an energy of $2\mathrm{E}_{\mathrm{rec}}$ to the atom, which enhances the loss rate of atoms from the optical trap by heating the atom. Therefore, we are interested in the amount of ASE light present in our state-dependent lattices to determine the scattering rate.

## 5.2 Laser ASE level determination

From a previous experimental work, we know that ASE levels as low as ∼-50 dB at a wavelength of 689.449 nm with respect to the power level of the spectral peak of the laser may introduce heating effects [43, 67]. Therefore, it is important to determine how much ASE light is produced by our lasers at this wavelength. Further suppression of the ASE is necessary if the ASE level that we determine is not lower than -50 dB at a wavelength of 689.449 nm. In this Section, we discuss the methods that we use for determining the ASE level of our diode lasers.

The quantity we want to determine is the amount of power produced by the lasers at a wavelength of 689.449 nm when they are operating at the tune-out wavelength. In principle, we can determine this quantity by measuring the spectrum of the laser with an optical spectrum analyser (OSA). An OSA is an instrument that recieves an optical signal as input and provides information about the distribution of power in this input light as a function of wavelength. Inside our commercial OSA (Ando, AQ6315E), there is a diffraction grating that separates the incoming light into its wavelength components by creating a diffraction pattern. This separation is based on the principle that different wavelengths of light are diffracted with different angles from the grating. The light that is diffracted in a certain direction by the grating is sent to a focusing mirror which focuses the light on a narrow slit which the beam passes through. Therefore, the wavelength of the light that passes through this slit can be tuned by rotating the grating with a stepper motor. Then, the power of the light passing through the slit is measured with an optical sensor and digitally displayed to the user. Therefore, an OSA measures and displays the frequency distribution of power in a light source.

An important parameter in understanding the spectrum that an OSA measures is the resolution bandwidth (RBW). The RBW of an OSA stands for the minimum wavelength separation between two spectral components that the OSA can distinguish. For instance, if two peaks with a wavelength separation much smaller than the RBW are present in the spectrum of the input signal, the OSA displays a single peak that has a broader linewidth and a lower amplitude than the original two peaks. Furthermore, if a single peak that has

a much narrower linewidth than the RBW is present in the spectrum of the input signal, the OSA displays a broader peak with a lower amplitude than the original peak. Our OSA has a RBW of 0.05 nm which corresponds to 31.5 GHz at the tune-out wavelength. The RBW of our OSA may be sufficient to reveal the broad spectrum of the ASE. However, this RBW value is not sufficient to resolve the linewidth of our lasers since this linewidth is around 100 kHz for the master laser according to its datasheet. This situation implies that the OSA can measure how much optical power is present within a $\pm 0.025$ nm range around the central wavelength of the lasers, but it underestimates the actual power level of the peak of the laser spectrum and overestimates the laser linewidth. However, we need to resolve the spectral peak to determine the power of the ASE light produced at a certain wavelength with respect to this peak. For this reason, we additionally use a commercial linewidth analyser (HighFinesse, LWA-10k).

The LWA measures the frequency deviations of our laser to analyze its spectrum. It uses a frequency discriminator to achieve this task. Frequency discriminator is an optical component inside the LWA that converts frequency noise of our laser to intensity noise, which is measured with a photodetector. The linewidth and the spectral lineshape of the laser can be analyzed using these frequency deviations. We refer the reader to Ref. [73] for a detailed description of this analysis. Our LWA can measure the spectrum in a frequency window of $\pm 10$ MHz around the central frequency of the laser with a resolution of 50 Hz. Therefore, by using both the OSA and the LWA, we can reveal the power level of the ASE and the peak of the laser spectrum at the same time. Here, we describe the measurements we performed with the LWA and the OSA and how we combine the two measurements.

First, we lock our slave lasers to the master laser. We attach the monitoring fiber of the injection lock module to the fiber port of the OSA on its front panel. We measure the spectrum for both injection lock lasers. Then, we go through the same procedure of measurement with both lasers using the LWA. With the LWA measurement, we obtain the lineshapes of the lasers. We present these lineshapes in Fig. 5.1. To obtain the linewidth of our lasers, we fit a Voigt profile to the measured lineshape. A Voigt profile is a suitable choice for this fitting task since it provides a way to describe the observed lineshape of the lasers accurately by combining Lorentzian and Gaussian profiles. Mathematically, the Voigt profile is the convolution of a Gaussian function and a Lorentzian function, given by

$$V(\omega;\sigma,\gamma) = \frac{1}{\sigma\pi\sqrt{2\pi}} \int_{-\infty}^{\infty} \frac{\gamma \exp(-(\omega - x)^2/2\sigma^2)}{x^2 + \gamma^2} dx \tag{5.10}$$

where $\omega$ is the frequency offset from the center of the spectral line shape, $\sigma$ is the standard deviation of the Gaussian profile and $\gamma$ is the half width at half maximum (HWHM) of the Lorentzian profile. From the Voigt functions we fit, we find $\sigma = 145.7(2)$ kHz and $\gamma = 7.9(2)$ kHz for the minus arm injection lock laser, $\sigma = 183.0(2)$ kHz and $\gamma = 25.7(3)$ kHz for the plus arm injection lock laser. We present these fits in Fig. 5.1.

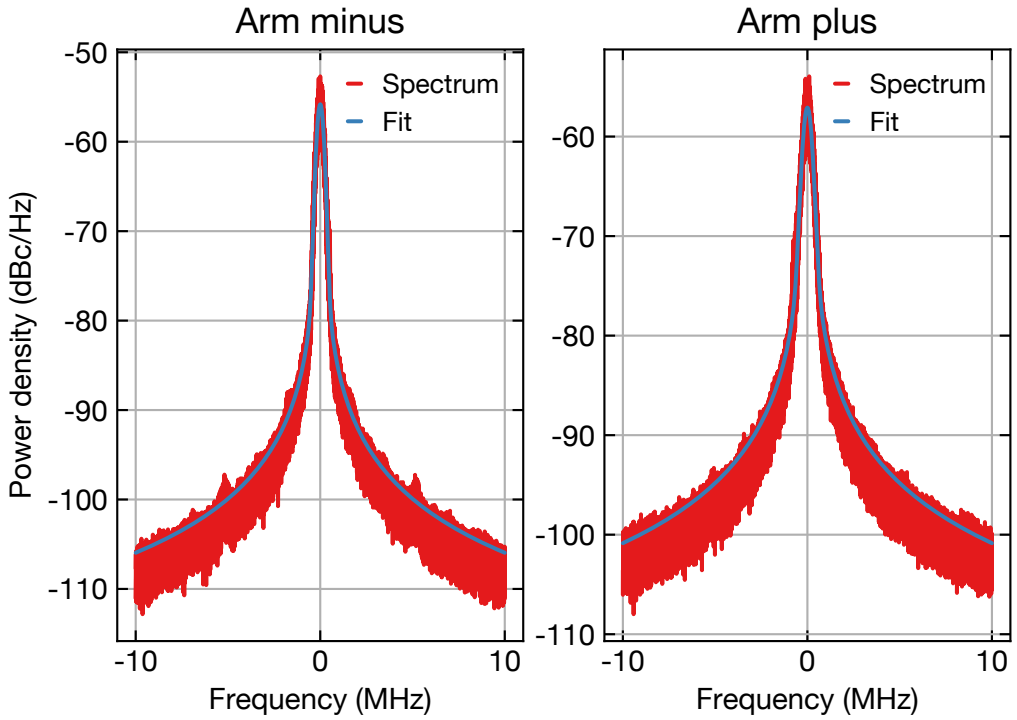


**Figure 5.1** Spectra of the injection lock lasers measured with the LWA in a frequency window of $\pm 10$ MHz. We fit Voigt functions to the measured spectra and find $\sigma = 145.7(2)$ kHz and $\gamma = 7.9(2)$ kHz for the minus arm injection lock laser, $\sigma = 183.0(2)$ kHz and $\gamma = 25.7(3)$ kHz for the plus arm injection lock laser.

To combine our measurements which we carried out with the OSA and LWA, we need to have the same units for both spectra. Therefore, we explain the following units that are relevant for our calculations.

***dBc*** The unit of dBc is a logarithmic unit that stands for dB relative to the carrier. Here, carrier is usually defined as the average power of the measured signal. Therefore, it is common to use this unit when measuring the power spectrum of the noise in a signal. In our case, we can think of the power of the ASE light as noise and the average power of the laser, which we can measure with a powermeter, as the carrier.

***dBc/Hz*** The unit of dBc/Hz stands for decibels relative to the carrier in a 1-Hz bandwidth. We can consider this unit as a unit of power density. We simply divide the measured spectrum, which is in units of dBc, by its resolution bandwidth to obtain this unit. Note that the logarithmic unit dBc should be made linear first before dividing it by the resolution bandwidth.

***dBm*** Decibels relative to milliwatt (dBm) is a logarithmic unit used to measure the power level of a signal relative to a power of 1 mW. Any quantity specified with the unit mW can be converted to dBm by taking its common logarithm ($\log_{10}$) and multiplying it by 10. This unit can also be converted to dBm/Hz, which stands for the power level relative to a power of 1 mW in a 1-Hz bandwidth.

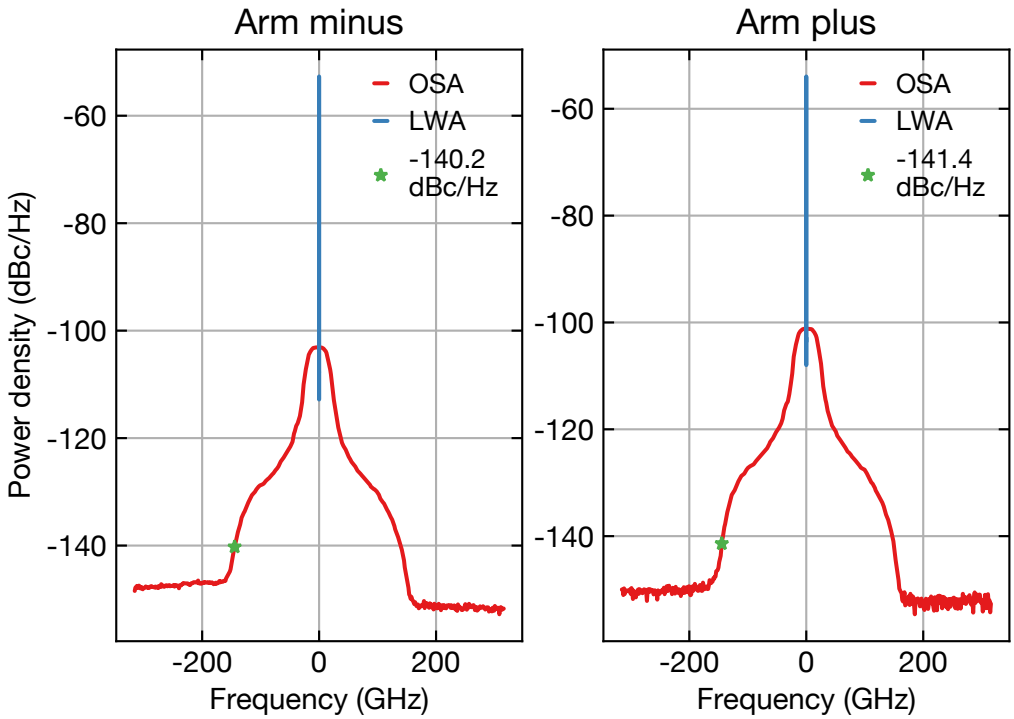


**Figure 5.2** The spectrum measurements of the injection lock lasers obtained with the OSA and the LWA combined in a single plot. From these figures, we obtain ASE levels of -140.2 dBc/Hz and -141.4 dBc/Hz at the frequency of the $^1\mathrm{S}_0 - {}^3\mathrm{P}_1$ transition.

The spectrum that we measure using the OSA has units of dBm, which we convert to dBm/Hz. The units of the LWA measurement is dBc/Hz. We now describe the procedure we go through to obtain the same units for both spectra. First, we extrapolate the data that we obtain from the LWA up to an RBW of the OSA, which is 31.5 GHz, by assuming that the tails of the LWA spectrum stay constant outside of its frequency window of $\pm$10 MHz. We calculate the total area under this extrapolated power-density spectrum. This area is proportional to the total power that is contained within one RBW of the OSA. Then, we calculate the area in the frequency window of $\pm$10 MHz and divide it by the total area. This division tells us the fraction of power contained in the frequency window of $\pm$10 MHz. We multiply the peak value of the OSA spectrum with this fraction. The result of this multiplication is the absolute power that is contained within the frequency window

of $\pm$10 MHz in units of dBm, which we define as the carrier since most of the power of the laser is concentrated in this frequency window. Then, we normalize the entire OSA spectrum to this carrier, which converts the units of the OSA spectrum to dBc/Hz. The level of the resulting spectrum at 689.449 nm now tells us how much power is present at this wavelength with respect to the carrier in a 1-Hz bandwidth. We note that the peak of the resulting spectrum will not reach zero, because we define the carrier as the power in the frequency window of $\pm$10 MHz rather than the peak value of the spectrum. After these calculations, we present both spectra (LWA & OSA) in units of dBc/Hz in Fig. 5.2. We find that the ASE levels of the lasers at a wavelength of 689.449 nm are -140.2 dBc/Hz and -141.4 dBc/Hz. These values correspond to -35.2 dBc and -36.4 dBc in a bandwidth of 31.5 GHz, which is the RBW of the OSA. These values are not lower than the previously mentioned ASE level of -50 dB with respect to the spectral peak. Furthermore, as we show later in this Chapter, these ASE levels cause significant photon scattering. Therefore, we find it necessary to suppress the ASE level of our lasers further.

## 5.3 ASE filtering

Since the ASE level of our lasers is not low enough, we use commercial ASE suppression filters (Coherent, ASE-689.22@9.8) in our experimental setup. Here, we discuss the alignment process and how we experimentally measure the total ASE suppression provided by these filters.

Our commercial ASE filters are dielectric multilayer structures that suppress the ASE level of an incoming beam by transmitting some of the light while reflecting the rest of it in a wavelength-dependent manner. Ideally, the light that originates from the ASE is transmitted and the rest of the light is reflected from the surface of the filter. We use the reflected beam in our experiment since its ASE level is suppressed. We also use a second ASE filter after the first one for more suppression.

Since a portion of the light inbound to the filter is either transmitted or absorbed by the medium of the filter, some optical power is lost. We refer to the ratio between the power of the reflected beam and the power of the incoming beam as the diffraction efficiency. We note that this quantity can be expressed in logarithmic units, or as percentage. Ideally, diffraction efficiency at a wavelength should tell us the suppression of power at that wavelength. According to the datasheets, our filters have diffraction efficiencies of 85 % at the tune-out wavelength (689.22 nm) with a reflection angle of 9.8° with respect to the normal of their surfaces. At this reflection angle, the wavelength-dependent diffraction efficiency of the filters is simulated by Coherent. Since we use two filters successively in our setup, we take the square of the simulated diffraction efficiency. We present the result in Fig. 5.3, which suggests that the ASE suppression at a wavelength of 689.449 nm is -53.2 dB.

To test the ASE suppression provided by the ASE filters, we perform an experiment.

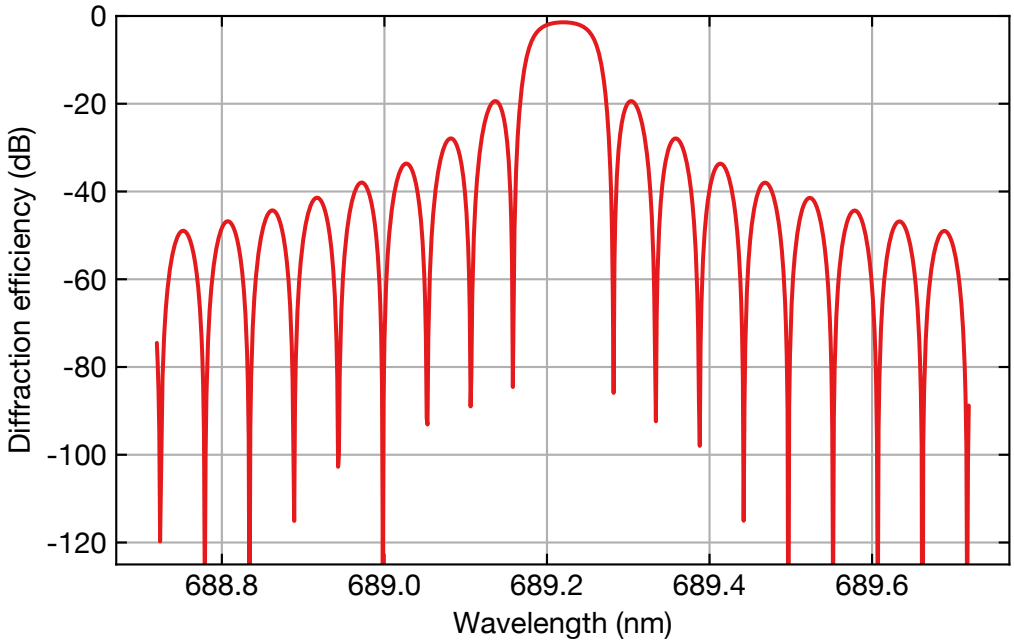


**Figure 5.3** Wavelength-dependent diffraction efficiency of two ASE filters that are placed successively in the beam path, simulated by Coherent. We observe an overall reduction in the diffraction efficiency for wavelengths that are far away from the tune-out wavelength and abrupt dips in the diffraction efficiency at certain wavelengths. This figure suggests that the ASE suppression at a wavelength of 689.449 nm is -53.2 dB.

First, we tune the wavelength of our master laser to the tune-out wavelength and lock the slave lasers to the master laser. We monitor the master laser wavelength on a wavelength meter. We mount the ASE filters on kinematic mirror mounts (Thorlabs, Polaris-K05T6). Then, we place the filters in the beam path after the injection lock lasers and the cylindrical telescopes. We maximize the power of the beam reflected from the filters by rotating the filters horizontally with the screws on the kinematic mount. We ensure that the power of the reflected light is maximized using a power meter. Then, we place the second filter on the path of the reflected beam. We go through the same angle-alignment procedure we did for the first filter. We measure the power before and after the two ASE filters and calculate a total diffraction efficiency of 76 %. Without misaligning the ASE filters, we incrementally increase the wavelength of the master laser by increasing the temperature of the laser diode. During this procedure, if the slave laser diodes get unlocked from the master laser due to the change in the wavelength, we lock them again at the new wavelength. Then, we measure the power before and after the two ASE filters again at the new wavelength. We repeat this procedure until we cannot change the temperature any more, i.e., when we reach the maximum recommended temperature of the master laser diode (35°C). Then, we reduce the temperature and rotate the reflective grating of the master

laser to tune its wavelength by a larger amount. We lock the slave lasers again after rotating the grating. We continue increasing the temperature and measuring the diffraction efficiencies. We plot the diffraction efficiency as a function of laser wavelength in Fig. 5.4. According to this figure, the diffraction efficiency at a wavelength of 689.449 nm is -33.6 dB for the minus arm laser and -32.6 dB for the plus arm laser. To calculate the overall ASE suppression from these values, we compare them to the diffraction efficiency of 76 % at the tune-out wavelength, which corresponds to -1.2 dB. Therefore, the ASE suppression at a wavelength of 689.449 nm is -32.4 dB for the minus arm and -31.4 dB for the plus arm.

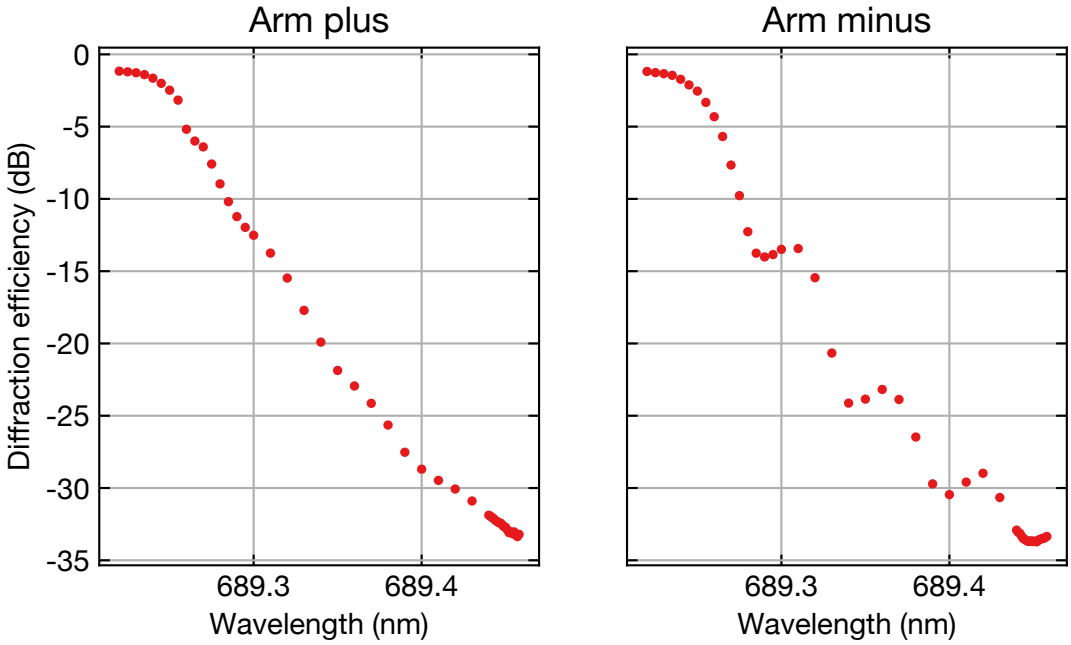


**Figure 5.4** Measured diffraction efficiencies of the ASE filters as a function of laser wavelength. The dips at certain wavelengths are less pronounced in these figures compared to the simulation results. We estimate an ASE suppression of more than 30 dB at a wavelength of 689.449 nm from these measurements.

In principle, we would expect the measured diffraction efficiencies to be the same as the simulation results in Fig. 5.3, i.e., we would expect to observe the dips that we observe in the simulation results. However, we do not see these dips in our measurement. We argue that this is due to the optical aberrations in the beam profile introduced by the cylindrical telescope. Since the filters are highly angle sensitive, aberrations in the wavefront may systematically reduce the suppression efficiency of the filters. Unfortunately, it is a challenging task to characterize how much these aberrations contribute to the suppression efficiency reduction. Therefore, we simply accept the measured suppression values of -32.4 dB and -31.4 dB and proceed our scattering rate calculations with these values.

### 5.3.1 ASE suppression of the crossed-cavity

In addition to the ASE suppression provided by the commercial ASE filters, our crossed cavity provides us with additional suppression at a wavelength of 689.449 nm. Here, we explain how the crossed cavity provides this suppression and how we estimate it.

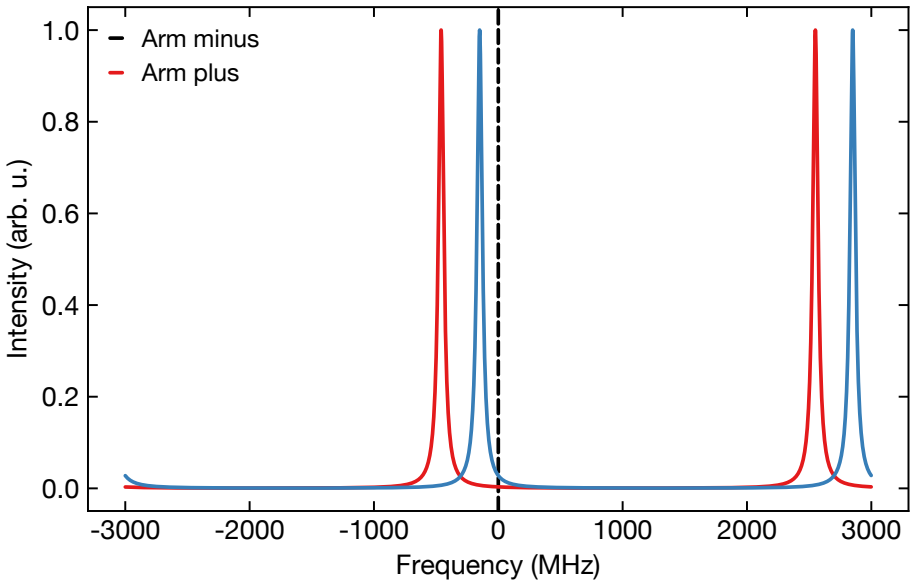


**Figure 5.5** The modes of the crossed cavity around the wavelength of the $^1S_0 - {}^3P_1$ transition, numerically represented by Lorentzian curves. The dashed line represents the transition wavelength.

As discussed in Sec. 4.3, we measure the resonance frequencies of the crossed cavity near a wavelength of 689.449 nm and present them in Tab. 4.2. Due to these cavity resonances, the intensity of the ASE light at a wavelength of 689.449 nm may get amplified. However, since we know that this wavelength does not coincide with the center of the cavity resonances, the light at this wavelength will be suppressed, instead of being amplified. To calculate the suppression, we first represent the cavity modes around the wavelength of 689.449 nm by plotting two Lorentzian functions numerically in Fig. 5.5. Then, we calculate the frequency-dependent enhancement of the cavity from these Lorentzian functions and show it in Fig. 5.6. To do this, we simply set the peak of the Lorentzian function to 147, which is the enhancement factor of the crossed cavity. We also use the known linewidth of 5.6 MHz of the crossed cavity as the FWHM of the Lorentzian function. We find that the minus arm suppresses the light at a wavelength of 689.449 nm by -12.9 dB and the plus arm suppresses it by -22.6 dB. Hence, combining the ASE suppression of the filters and the cavity, we have total suppressions of -45.3 dB and -54 dB for the minus arm and the plus arm, respectively.

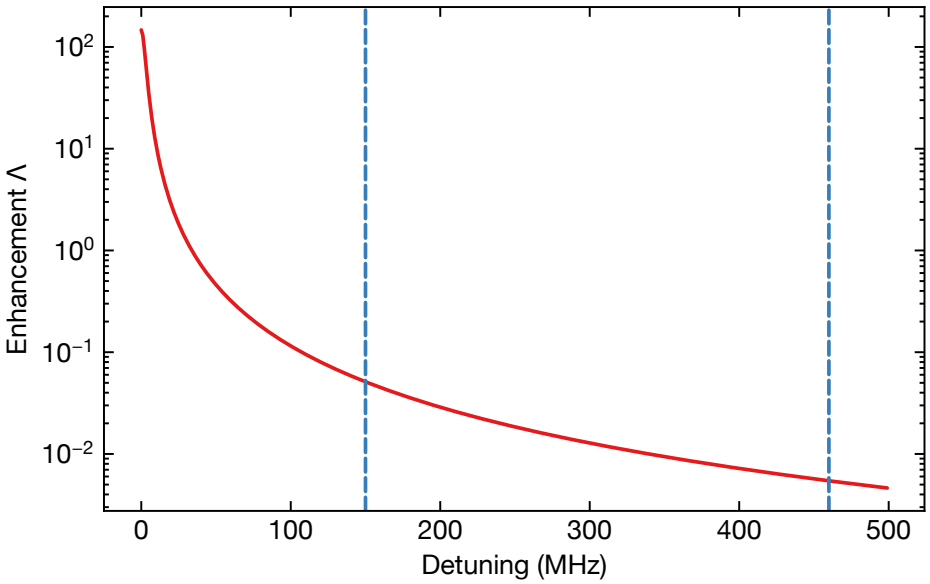


**Figure 5.6** The enhancement of the cavity as a function of detuning from the resonance frequency of the cavity. The dashed lines represent the detunings of the measured cavity modes from the $^1\mathrm{S}_0 - {}^3\mathrm{P}_1$ transition frequency.

## 5.4 Scattering rate calculations

Having obtained the ASE level of our lasers at a wavelength of 689.449 nm and the amount of suppression that we can achieve with the ASE filters and the crossed cavity at this wavelength, we proceed with calculating the rate of scattering from the $^1\mathrm{S}_0 - {}^3\mathrm{P}_1$ transition in this Section.

We use Eqn. (5.6) in our calculations. For this transition, we have $\gamma = 7.4$ kHz and $I_{\mathrm{sat}} = 3.0\ \mu\mathrm{W/cm}^2$. First, we notice that Eqn. (5.6) assumes a laser operating at a single wavelength. Such a laser has an infinitely narrow linewidth and a single peak in its spectrum. As discussed in Sec. 5.2, this is not the case for our lasers. Our lasers have a finite linewidth and a broad-band ASE spectrum. Therefore, in our calculations, we treat the lineshape of our lasers as a collection of single-frequency lasers with adjacent detunings from the $^1\mathrm{S}_0 - {}^3\mathrm{P}_1$ transition frequency. In other words, we use a detuning-dependent saturation parameter $s_0(\Delta)$ in Eqn. (5.6). With this assumption in mind, we calculate the scattering rate contribution of each single-frequency laser around the wavelength of 689.449 nm and present it in Fig. 5.7 (a). In this figure, we use a bin width of 7.4 kHz for the horizontal axis, which is the linewidth of the transition that we are interested in. To calculate this curve, we assume a total input power of 30 mW in front of each cavity arm. With this input power, we calculate the power of the ASE light around a wavelength of

689.449 nm using the ASE levels of -140.2 dBc/Hz and -141.4 dBc/Hz, which we determined in Sec. 5.2. We calculate the power of the ASE light contained in our bin width of 7.4 kHz at a wavelength of 689.449 nm. Then, we include the ASE suppression provided by the filters and the crossed cavity to calculate the suppressed power at this wavelength. By using the waist of the cavity as $w_0 = 396\ \mu\mathrm{m}$, we convert this power to an intensity. With the intensity value that we calculate, we estimate an on-resonant scattering rate of $\Gamma_{\mathrm{sc}} = 2.1 \times 10^{-4}\ \mathrm{s}^{-1}$, which is the peak value of the curve in Fig. 5.7 (a). From this figure, we observe that the scattering rate decreases rapidly for increasing detuning from the ${}^1\mathrm{S}_0 - {}^3\mathrm{P}_1$ transition frequency. To take the off-resonant scattering rate contributions into account, we sum these contributions and plot this summation as a function of detuning in Fig. 5.8. This summation converges to $\sim 3.6 \times 10^{-4}\ \mathrm{s}^{-1}$ rapidly. Therefore, we may consider this value as an upper bound for the scattering rate. Note that this argument does not hold for high intensities ($s_0 \gg 1$) since this means that the summed scattering rate saturates to a value higher than $\Gamma/2$.

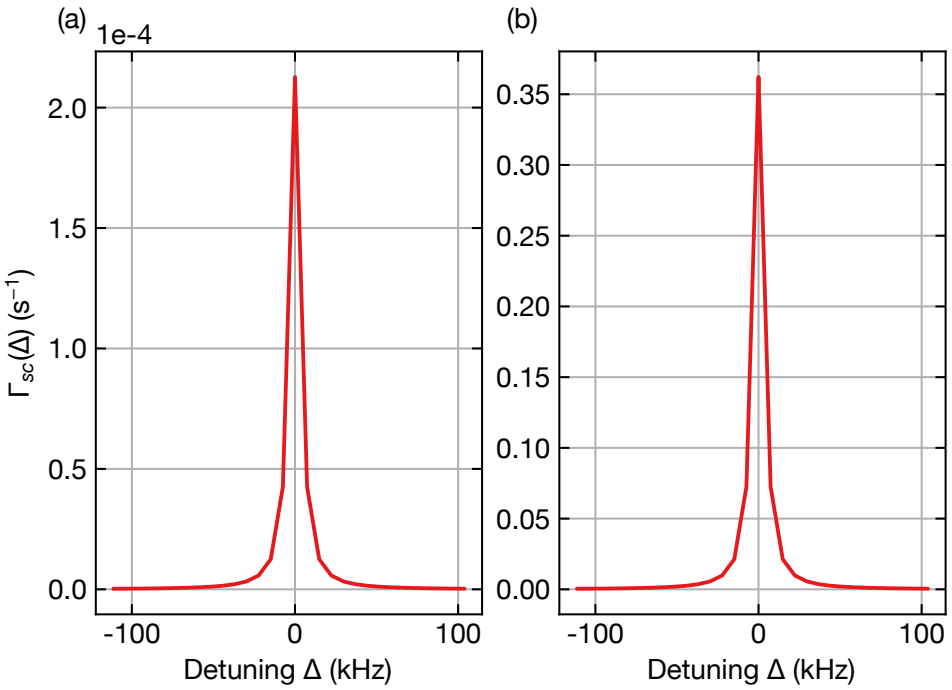


**Figure 5.7** Scattering rate contributions as a function of detuning from the transition frequency **(a)** with ASE filters **(b)** without ASE filters.

With this upper bound for the scattering rate, we estimate that approximately 0.036% of the atoms in the lattice will undergo scattering in a period of 1 s. Considering that the durations of the experimental cycles we plan to implement in the future with state-dependent lattices are shorter than 1 s, this scattering rate will not cause a significant

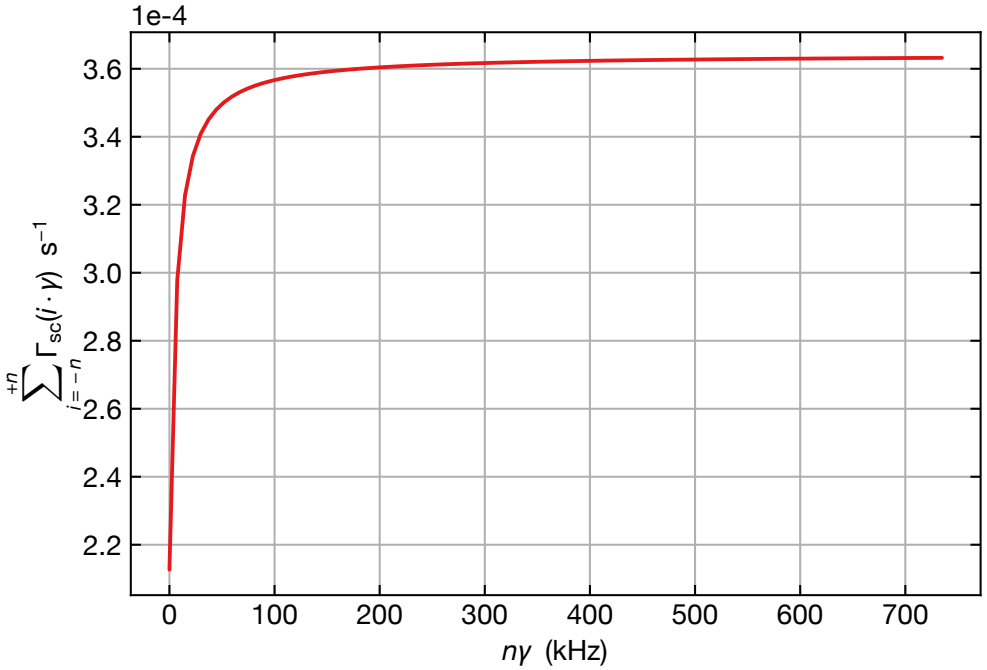


**Figure 5.8** Summation of the scattering rate contributions around the transition frequency. This summation converges to $\sim 3.6 \times 10^{-4}$ s$^{-1}$ within a detuning of a few 100 kHz.

atom loss due to heating. In Fig. 5.7 (b), we also present the scattering rate when the ASE suppression of the filters is not included. The on-resonant scattering rate in this case is $\Gamma_{\mathrm{sc}} = 0.36$ s$^{-1}$, which is significantly higher than the case where filters are used. Hence, we anticipate that by suppressing the ASE level of our diode lasers, we can reduce the loss of the atoms in the tune-out lattice drastically.

As a last remark, we calculate the scattering rate induced by the off-resonant spectral peak of the lattice field, since this may also contribute to the total scattering rate. For this calculation, we directly use the enhanced intensity of the lattice field for $s_0$, assuming a power of 30 mW in front of each arm of the crossed cavity and an enhancement factor of $\Lambda = 147$. We use a detuning of $\Delta = 143$ GHz, which is the frequency difference between the tune-out wavelength and the wavelength of the $^1\mathrm{S}_0 - {}^3\mathrm{P}_1$ transition. We calculate this scattering rate as $\Gamma_{\mathrm{sc}} = 0.0092$ s$^{-1}$. Although this contribution is higher than the contribution of the on-resonant scattering, it is still low enough since it means that only 0.9% of the atoms in the lattice will undergo scattering in a period of 1 s. Therefore, we anticipate that the scattering of lattice photons by the atoms will not cause significant heating in the tune-out lattice, provided that we suppress the ASE in our injection lock lasers.

## Conclusion

In conclusion, we have shown the successful suppression of ASE in our lasers, leading to negligible scattering rates. We first estimated the ASE level of our lasers by combining the measurements we obtained from the LWA and the OSA. Then, we measured the ASE suppression of the filters by tuning the wavelength of the lasers and measuring the diffraction efficiencies of the filters without changing the alignment. We also estimated the ASE suppression of the crossed cavity. Then, we calculated the scattering rate by considering these suppression levels and found that we can reduce the scattering in the lattice to negligible levels.

# Chapter 6

# Conclusion and Outlook

The main aim of this thesis was to construct a stable laser system to generate cavity-enhanced tune-out lattices. In Chapter 3, we introduced the diode lasers we used for this purpose, and reported on the construction of two injection lock modules for amplifying the optical power of our master laser. We also constructed a Fabry-Pérot cavity setup to monitor the injection locking status. With these injection lock modules, we were able to reach a power of $30\ \mathrm{mW}$ before each arm of the crossed cavity, giving us a lattice depth of more than $50\mathrm{E}_{\mathrm{rec}}$ for the $^3\mathrm{P}_2$ state. Then, we described how we obtained Gaussian beams using cylindrical telescopes to maximize our fiber-coupling efficiencies.

In Chapter 4, we presented the laser stabilization scheme that we devised to suppress the parametric heating in the lattice. First, we discussed the frequency-to-amplitude noise conversion in our cavity and how this situation enhances the parametric heating rate. Then, we described the working principle of the PDH technique that involves locking the frequency of a laser to a reference cavity for the aim of reducing the frequency noise of the laser. We constructed two EOMs and their respective drivers to implement the PDH technique. We reported on the laser-induced photorefractive damage that we observe on the EOM crystals at a laser intensity of $56\ \mathrm{W/cm^2}$. We argued that we can improve the damage threshold up to $8 \times 10^6\ \mathrm{W/cm^2}$ by using MgO-doped $\mathrm{LiNbO_3}$ crystals, instead of the pure ones. Then, we constructed an experimental setup that combines the PDH technique with an intensity stabilization control loop. We used AOMs to modulate the frequency and the intensity of the lasers. We additionally stabilized the frequency of our master laser by locking it to a frequency comb. We achieved this task by producing a beat note between the master laser and the frequency comb, and by stabilizing the beat note frequency with a phase-locked loop. We measured the long-term stability of the laser system and found out that the injection locking is only stable for $\sim$5 h. We claimed that this situation can be improved in the future by making the injection lock modules air tight using a wedged window at the laser beam output. Nonetheless, we found this stability period to be sufficient for conducting our experiments. After employing all of the presented stabilization schemes, we measured the RIN at different points in our setup and observed several peaks in the RIN originating from the current supplied by the laser controllers of the injection lock lasers. We demonstrated how we can successfully suppress these peaks by passing the current through a low-pass LC filter. Since this filter made the the base level of the RIN fluctuate due to external affects such as temperature fluctuations, we did not integrate it in our experiment yet. The integration of this filter

requires the development of a PCB design with appropriate electronic components. Finally, we calculated the heating rate constant using the RIN of the light transmitted from the cavity. Although we calculated a low heating rate constant with this measurement, we still need to verify this estimation by measuring the lifetime of the atoms in the lattice experimentally, similar to how it was done in Ref. [67].

In Chapter 5, we focused on suppressing the ASE in our lasers for the purpose of reducing the on-resonant photon scattering from the $^1\mathrm{S}_0 - {}^3\mathrm{P}_1$ transition of strontium. We measured the spectra of our lasers to determine their ASE levels. Since the spectrum analyzer that we used could not resolve the peak of the laser properly, we additionally used a linewidth analyzer that could measure the spectrum in a smaller window around the central wavelength of the laser. Therefore, we were able to resolve the spectral peak and the ASE level of the lasers at the same time. When combining these two separate measurements, we made certain assumptions. For instance, we conservatively assumed that the tails of the spectrum measured by the linewidth analyzer stay constant outside of its frequency window. A more accurate approach would be to use the Voigt function to extrapolate the data. This would mean a higher spectral peak compared to the ASE level of the laser, which would result in an even lower scattering rate. Since we could already estimate a negligible scattering rate, we did not investigate this subject any further. However, we may need to consider this approach if we work with powers higher than $30\ \mathrm{mW}$ in the future. To suppress the ASE level of the lasers, we used commercial ASE filters and we experimentally measured their suppression. There was a discrepancy between this measurement and the raw data of the simulation provided to us by Coherent. We argued that this discrepancy is due to optical aberrations introduced by the cylindrical telescopes in our setup. These aberrations need to be minimized by choosing cylindrical lenses with longer focal lengths. Then, the suppression can become more efficient.

In conclusion, we believe that once the laser system that we developed is embodied in the main experiment with the improvements mentioned above, it will serve as a useful tool to conduct quantum simulations of light-matter interfaces in the near future.

# References


[1] Manin, Y. I. *Computable and Non-Computable*, Sovetskoe Radio (1980).

[2] Feynman, R. P. *Simulating physics with computers*, International Journal of Theoretical Physics **21**, 467–488 (1982). DOI: 10.1007/BF02650179.

[3] Bloch, I., J. Dalibard, and S. Nascimbène. *Quantum simulations with ultracold quantum gases*, Nature Physics **8**, 267 (2012). DOI: 10.1038/nphys2259.

[4] Bloch, I., J. Dalibard, and W. Zwerger. *Many-body physics with ultracold gases*, Rev. Mod. Phys. **80**, 885 (2008). DOI: 10.1103/RevModPhys.80.885.

[5] Gross, C. and I. Bloch. *Quantum simulations with ultracold atoms in optical lattices*, Science **357**, 995 (2017). DOI: 10.1126/science.aal3837.

[6] Jessen, P. S. and I. H. Deutsch. *Optical Lattices*, Adv. Mol. Opt. Phys. **37**, 95 (1996). DOI: 10.1016/S1049-250X(08)60099-3.

[7] Esslinger, T. *Fermi-Hubbard Physics with Atoms in an Optical Lattice*, Annual Review of Condensed Matter Physics **1**, 129 (2010). DOI: 10.1146/annurev-conmatphys-070909-104059.

[8] Greiner, M., O. Mandel, T. Esslinger, T. W. Hänsch, and I. Bloch. *Quantum phase transition from a superfluid to a Mott insulator in a gas of ultracold atoms*, Nature **415**, 39 (2002). DOI: 10.1038/415039a.

[9] Pachos, J. K. and P. L. Knight. *Quantum Computation with a One-Dimensional Optical Lattice*, Phys. Rev. Lett. **91**, 107902 (Sept. 2003). DOI: 10.1103/PhysRevLett.91.107902.

[10] Brennen, G. K., D. Song, and C. J. Williams. *Quantum-computer architecture using nonlocal interactions*, Phys. Rev. A **67**, 050302 (May 2003). DOI: 10.1103/PhysRevA.67.050302.

[11] Buluta, I., S. Ashhab, and F. Nori. *Natural and artificial atoms for quantum computation*, Rep. Prog. Phys. **74**, 104401 (2011). DOI: 10.1088/0034-4885/74/10/104401.

[12] González-Tudela, A. and J. I. Cirac. *Markovian and non-Markovian dynamics of quantum emitters coupled to two-dimensional structured reservoirs*, Phys. Rev. A **96**, 043811 (2017). DOI: 10.1103/PhysRevA.96.043811.

[13] González-Tudela, A. and J. I. Cirac. *Quantum Emitters in Two-Dimensional Structured Reservoirs in the Nonperturbative Regime*, Phys. Rev. Lett. **119**, 143602 (2017). DOI: 10.1103/PhysRevLett.119.143602.

[14] González-Tudela, A., C.-L. Hung, D. E. Chang, J. I. Cirac, and H. Kimble. *Subwavelength vacuum lattices and atom–atom interactions in two-dimensional photonic crystals*, Nature Photonics **9**, 320–325 (2015). DOI: 10.1038/nphoton.2015.54.

[15] Krinner, L., M. Stewart, A. Pazmino, J. Kwon, and D. Schneble. *Spontaneous emission of matter waves from a tunable open quantum system*, Nature **559**, 589–592 (2018). DOI: 10.1038/s41586-018-0348-z.

[16] Kwon, J., Y. Kim, A. Lanuza, and D. Schneble. *Formation of matter-wave polaritons in an optical lattice*, Nature Physics **18**, 657–661 (2022). DOI: 10.1038/s41567-022-01565-4.

[17] Bakr, W. S., J. I. Gillen, A. Peng, S. Fölling, and M. Greiner. *A quantum gas microscope for detecting single atoms in a Hubbard-regime optical lattice*, Nature **462**, 74–77 (2009). DOI: 10.1038/nature08482.

[18] Sherson, J. F., C. Weitenberg, M. Endres, M. Cheneau, I. Bloch, and S. Kuhr. *Single-atom-resolved fluorescence imaging of an atomic Mott insulator*, Nature **467**, 68–72 (2010). DOI: 10.1038/nature09378.

[19] Parsons, M. F., F. Huber, A. Mazurenko, C. S. Chiu, W. Setiawan, K. Wooley-Brown, S. Blatt, and M. Greiner. *Site-Resolved Imaging of Fermionic* $^6$Li *in an Optical Lattice*, Phys. Rev. Lett. **114**, 213002 (2015). DOI: 10.1103/PhysRevLett.114.213002.

[20] Haller, E., J. Hudson, A. Kelly, D. A. Cotta, B. Peaudecerf, G. D. Bruce, and S. Kuhr. *Single-atom imaging of fermions in a quantum-gas microscope*, Nature Physics **11**, 738–742 (2015). DOI: 10.1038/nphys3403.

[21] Cheuk, L. W., M. A. Nichols, M. Okan, T. Gersdorf, V. V. Ramasesh, W. S. Bakr, T. Lompe, and M. W. Zwierlein. *Quantum-Gas Microscope for Fermionic Atoms*, Phys. Rev. Lett. **114**, 193001 (2015). DOI: 10.1103/PhysRevLett.114.193001.

[22] Omran, A., M. Boll, T. A. Hilker, K. Kleinlein, G. Salomon, I. Bloch, and C. Gross. *Microscopic Observation of Pauli Blocking in Degenerate Fermionic Lattice Gases*, Phys. Rev. Lett. **115**, 263001 (2015). DOI: 10.1103/PhysRevLett.115.263001.

[23] Yamamoto, R., J. Kobayashi, T. Kuno, K. Kato, and Y. Takahashi. *An ytterbium quantum gas microscope with narrow-line laser cooling*, New Journal of Physics **18**, 023016 (2016). DOI: 10.1088/1367-2630/18/2/023016.

[24] Yang, J., L. Liu, J. Mongkolkiattichai, and P. Schauss. *Site-Resolved Imaging of Ultracold Fermions in a Triangular-Lattice Quantum Gas Microscope*, PRX Quantum **2**, 020344 (2021). DOI: 10.1103/PRXQuantum.2.020344.

[25] Kwon, K., K. Kim, J. Hur, S. Huh, and J.-y. Choi. *Site-resolved imaging of a bosonic Mott insulator of* $^7$Li *atoms*, Phys. Rev. A **105**, 033323 (2022). DOI: 10.1103/PhysRevA.105.033323.

[26] Daley, A. J. *Quantum computing and quantum simulation with group-II atoms*, Quantum Information Processing **10**, 865–884 (2011). DOI: 10.1007/s11128-011-0293-3.

[27] Muniz, J. A., D. J. Young, J. R. K. Cline, and J. K. Thompson. *Cavity-QED measurements of the* $^{87}$Sr *millihertz optical clock transition and determination of its natural linewidth*, Phys. Rev. Research **3**, 023152 (2021). DOI: 10.1103/PhysRevResearch.3.023152.

[28] Ludlow, A. D., M. M. Boyd, E. Peik, and P. Schmidt. *Optical atomic clocks*, Rev. Mod. Phys. **87**, 637–701 (2015). DOI: 10.1103/RevModPhys.87.637.

[29] Marti, G. E., R. B. Hutson, A. Goban, S. L. Campbell, N. Poli, and J. Ye. *Imaging Optical Frequencies with* $100\ \mu$Hz *Precision and* $1.1\ \mu$m *Resolution*, Phys. Rev. Lett. **120**, 103201 (2018). DOI: 10.1103/PhysRevLett.120.103201.

[30] Campbell, S. L., R. Hutson, G. Marti, A. Goban, N. Darkwah Oppong, R. McNally, L. Sonderhouse, J. Robinson, W. Zhang, B. Bloom, *et al. A Fermi-degenerate three-dimensional optical lattice clock*, Science **358**, 90–94 (2017). DOI: 10.1126/science.aam5538.

[31] Takamoto, M., F.-L. Hong, R. Higashi, and H. Katori. *An optical lattice clock*, Nature **435**, 321–324 (2005). DOI: 10.1038/nature03541.

[32] Brusch, A., R. Le Targat, X. Baillard, M. Fouché, and P. Lemonde. *Hyperpolarizability Effects in a* Sr *Optical Lattice Clock*, Phys. Rev. Lett. **96**, 103003 (2006). DOI: 10.1103/PhysRevLett.96.103003.

[33] Ludlow, A. D., M. M. Boyd, T. Zelevinsky, S. M. Foreman, S. Blatt, M. Notcutt, T. Ido, and J. Ye. *Systematic Study of the* $^{87}$Sr *Clock Transition in an Optical Lattice*, Phys. Rev. Lett. **96**, 033003 (2006). DOI: 10.1103/PhysRevLett.96.033003.

[34] Bishof, M., M. J. Martin, M. D. Swallows, C. Benko, Y. Lin, G. Quéméner, A. M. Rey, and J. Ye. *Inelastic collisions and density-dependent excitation suppression in a* $^{87}$Sr *optical lattice clock*, Phys. Rev. A **84**, 052716 (2011). DOI: 10.1103/PhysRevA.84.052716.

[35] Oelker, E. *et al. Demonstration of* $4.8 \times 10^{-17}$ *stability at* $1$ s *for two independent optical clocks*, Nature Photonics **13**, 714–719 (Oct. 2019). ISSN: 1749-4893. DOI: 10.1038/s41566-019-0493-4.

[36] Courtillot, I., A. Quessada, R. P. Kovacich, J.-J. Zondy, A. Landragin, A. Clairon, and P. Lemonde. *Efficient cooling and trapping of strontium atoms*, Opt. Lett. **28**, 468–470 (2003). DOI: 10.1364/OL.28.000468.

[37] Katori, H., T. Ido, Y. Isoya, and M. Kuwata-Gonokami. *Magneto-Optical Trapping and Cooling of Strontium Atoms down to the Photon Recoil Temperature*, Phys. Rev. Lett. **82**, 1116 (1999). DOI: 10.1103/PhysRevLett.82.1116.

[38] Trautmann, J. "The Magnetic Quadrupole Transition in Neutral Strontium." PhD thesis. Ludwig Maximilians Universität München, 2022. URL: https://www.ultracold.sr/publications/thesis_jan_trautmann.pdf.

[39] Nicholson, T. L., S. Campbell, R. Hutson, G. E. Marti, B. Bloom, R. L. McNally, W. Zhang, M. Barrett, M. S. Safronova, G. Strouse, *et al. Systematic evaluation of an atomic clock at* $2 \times 10^{-18}$ *total uncertainty*, Nature Communications **6**, 1–8 (2015). DOI: 10.1038/ncomms7896.

[40] Cooper, A., J. P. Covey, I. S. Madjarov, S. G. Porsev, M. S. Safronova, and M. Endres. *Alkaline-Earth Atoms in Optical Tweezers*, Phys. Rev. X **8**, 041055 (2018). DOI: 10.1103/PhysRevX.8.041055.

[41] Xu, X., T. H. Loftus, J. L. Hall, A. Gallagher, and J. Ye. *Cooling and trapping of atomic strontium*, JOSA B **20**, 968–976 (2003). DOI: 10.1364/JOSAB.20.000968.

[42] Snigirev, S., A. J. Park, A. Heinz, I. Bloch, and S. Blatt. *Fast and dense magneto-optical traps for strontium*, Phys. Rev. A **99**, 063421 (2019). DOI: 10.1103/PhysRevA.99.063421.

[43] Heinz, A. "Ultracold Strontium in State-Dependent Optical Lattices." PhD thesis. Ludwig Maximilians Universität München, 2020. URL: https://www.ultracold.sr/publications/thesis_andre_heinz.pdf.

[44] Heinz, A., J. Trautmann, N. Šantić, A. J. Park, I. Bloch, and S. Blatt. *Crossed optical cavities with large mode diameters*, Opt. Lett. **46**, 250–253 (2021). DOI: 10.1364/OL.414076.

[45] Trautmann, J., D. Yankelev, V. Klüsener, A. J. Park, I. Bloch, and S. Blatt. $^1\mathrm{S}_0 - {}^3\mathrm{P}_2$ *magnetic quadrupole transition in neutral strontium*, Physical Review Research **5**, 013219 (2023). DOI: 10.1103/PhysRevResearch.5.013219.

[46] Savard, T. A., K. M. O'Hara, and J. E. Thomas. *Laser-noise-induced heating in far-off resonance optical traps*, Physical Review A **56**, R1095 (1997). DOI: 10.1103/PhysRevA.56.R1095.

[47] Steck, D. A. *Quantum and Atom Optics*. 2007. URL: http://steck.us/teaching.

[48] Grimm, R., M. Weidemüller, and Y. B. Ovchinnikov. *Optical dipole traps for neutral atoms*, Adv. At. Mol. Opt. Phys. **42**, 95 (2000). DOI: 10.1016/S1049-250X(08)60186-X.

[49] Le Kien, F., P. Schneeweiss, and A. Rauschenbeutel. *Dynamical polarizability of atoms in arbitrary light fields: general theory and application to cesium*, The European Physical Journal D **67**, 1–16 (2013). DOI: 10.1140/epjd/e2013-30729-x.

[50] Safronova, M. S., S. G. Porsev, U. I. Safronova, M. G. Kozlov, and C. W. Clark. *Blackbody-radiation shift in the* Sr *optical atomic clock*, Phys. Rev. A **87**, 012509 (2013). DOI: 10.1103/PhysRevA.87.012509.

[51] Safronova, M., Z. Zuhrianda, U. Safronova, and C. W. Clark. *Extracting transition rates from zero-polarizability spectroscopy*, Physical Review A **92**, 040501 (2015). DOI: 10.1103/PhysRevA.92.040501.

[52] Daley, A. J., J. Ye, and P. Zoller. *State-dependent lattices for quantum computing with alkaline-earth-metal atoms*, The European Physical Journal D **65**, 207–217 (2011). DOI: 10.1140/epjd/e2011-20095-2.

[53] Ricci, L., M. Weidemüller, T. Esslinger, A. Hemmerich, C. Zimmermann, V. Vuletic, W. König, and T. Hänsch. *A compact grating-stabilized diode laser system for atomic physics*, Optics Communications **117**, 541–549 (1995). DOI: 10.1016/0030-4018(95)00146-Y.

[54] Liu, Z. and R. Slavik. *Optical Injection Locking: from Principle to Applications*, Journal of Lightwave Technology **38**, 43–59 (2020). DOI: 10.1109/JLT.2019.2945718.

[55] Jansa, N. "A frequency-stable diode laser system for spectroscopy and trapping of Sr atoms." MA thesis. Ludwig Maximilians Universität München, 2016. URL: https://ultracold.sr/publications/thesis_nejc_jansa.pdf.

[56] Milonni, P. W. and J. H. Eberly. *Laser physics*. John Wiley & Sons, 2010. ISBN: 9780470387719.

[57] Huber, H. *et al. Picosecond Laser Structuring for the Monolithic Serial Intercombination of CIS Solar Cells*, EUPVSEC conference (2009). URL: https://www.researchgate.net/publication/312968534_PICOSECOND_LASER_STRUCTURING_FOR_THE_MONOLITHIC_SERIAL_INTERCONNECTION_OF_CIS_SOLAR_CELLS.

[58] Saleh, B. E. A. and M. C. Teich. *Fundamentals of Photonics*. John Wiley & Sons, 2019. ISBN: 9780471839651. DOI: 10.1002/0471213748.

[59] Black, E. D. *An introduction to Pound-Drever-Hall laser frequency stabilization*, American Journal of Physics **69**, 79–87 (2001). DOI: 10.1119/1.1286663.

[60] SiTime. *Time Machine II User Manual*. 2019. URL: https://media.digikey.com/pdf/Data%20Sheets/SiTime%20PDFs/Time-Machine_II_UM_7-24-19.pdf.

[61] Yang, Y. "A Narrow-linewidth Laser System for the $^1S_0 - {}^3P_2$ Intercombination Transition in Strontium." MA thesis. Ludwig Maximilians Universität München, 2021. URL: https://www.ultracold.sr/publications/thesis_yilong_yang.pdf.

[62] Villarroel, J., J. Carnicero, F. Luedtke, M. Carrascosa, A. García-Cabañes, J. M. Cabrera, A. Alcazar, and B. Ramiro. *Analysis of photorefractive optical damage in lithium niobate: application to planar waveguides*, Optics Express **18**, 20852–20861 (2010). DOI: 10.1364/OE.18.020852.

[63] Aillerie, M., P. Bourson, M. Mostefa, F. Abdi, and M. Fontana. *Photorefractive damage in congruent* $LiNbO_3$. *Part I. Zinc doped lithium niobate crystals*, Journal of Physics: Conference Series **416**, 012001 (2013). DOI: 10.1088/1742-6596/416/1/012001.

[64] Asobe, M., O. Tadanaga, T. Yanagawa, H. Itoh, and H. Suzuki. *Reducing photorefractive effect in periodically poled* $\mathrm{ZnO}$*-and* $\mathrm{MgO}$*-doped* $\mathrm{LiNbO_3}$ *wavelength converters*, Applied Physics Letters **78**, 3163–3165 (2001). DOI: 10.1063/1.1374228.

[65] Hänsch, T. W. *Nobel lecture: passion for precision*, Reviews of Modern Physics **78**, 1297–1309 (2006). DOI: 10.1103/RevModPhys.78.1297.

[66] Howe, D., D. Allan, and J. Barnes. *Properties of signal sources and measurement methods*, Proceedings of the 35th Annual Symposium on Frequency Control (1981). URL: https://tf.nist.gov/general/pdf/554.pdf.

[67] Heinz, A., A. J. Park, S. C., J. Trautmann, S. G. Porsev, M. S. Safronova, I. Bloch, and S. Blatt. *State-Dependent Optical Lattices for the Strontium Optical Qubit*, Phys. Rev. Lett. **124**, 203201 (2020). DOI: 10.1103/PhysRevLett.124.203201.

[68] Träger, F. *Springer handbook of lasers and optics*. Springer, 2012. ISBN: 9783642194085. DOI: 10.1007/978-3-642-19409-2.

[69] Barnes, N. P. and B. M. Walsh. *Amplified spontaneous emission-application to Nd:YAG lasers*, IEEE J. Quantum Electron **35**, 101–109 (1999). DOI: 10.1109/3.737626.

[70] Blazek, M., S. Hartmann, A. Molitor, and W. Elsaesser. *Unifying intensity noise and second-order coherence properties of amplified spontaneous emission sources*, Opt. Lett. **36**, 3455–3457 (2011). DOI: 10.1364/OL.36.003455.

[71] Keppler, S., A. Sävert, K. J., M. Hornung, H. Liebetrau, J. Hein, and M. C. Kaluza. *The generation of amplified spontaneous emission in high-power CPA laser systems*, Laser & Photonics Reviews **10**, 264–277 (2016). DOI: 10.1002/lpor.201500186.

[72] Metcalf, H. J. and P. Van der Straten. *Laser cooling and trapping*. Springer Science & Business Media, 1999. ISBN: 9780387987286. DOI: 10.1007/978-1-4612-1470-0.

[73] Di Domenico, G., S. Schilt, and P. Thomann. *Simple approach to the relation between laser frequency noise and laser line shape*, Applied Optics **49**, 4801–4807 (2010). DOI: 10.1364/AO.49.004801.

# Acknowledgements

First of all, I would like to thank **Prof. Dr. Immanuel Bloch** for granting me the opportunity of being a part of such an excellent research environment.

I am very grateful to **Dr. Sebastian Blatt** for his supervision and guidance. His exceptional insight in physics inspired me on how to approach a problem as a researcher. The practical suggestions that I received from him have never failed to make my life easier.

I would like to thank **Dr. Andreas Schindewolf**, **Dr. Sebastian Pucher** and **Dr. Dimitry Yankelev** for their time and effort in teaching a master student so many aspects of our work. I am especially grateful to Dr. Sebastian Pucher for the valuable suggestions that he gave me while writing this thesis.

I would like to thank **Valentin Klüsener** for assisting and motivating me over the course of this project. His support made this work particularly enjoyable and interesting for me. I wish him the best in the remaining part of his doctoral studies.

I would like to thank **Felix Spriestersbach**, **Andrew Whimster** and **Andreas Meyer** for all their help in the laboratory. They always listened to the issues I was having in the laboratory and gave me sound advice. I also enjoyed the times when we did activities outside the institute such as climbing and hiking.

Many thanks to **Karsten Förster** for his help with electronics. Even when he had a very busy schedule, he was willing to help me with my projects that were essential for this thesis.

Lastly, I would like to thank my family for their unending support and love.